Cover Page

Universiteit Leiden

The following handle holds various files of this Leiden University dissertation:
http://hdl.handle.net/1887/80839

Author: Haffert, S.Y.
Title: High-resolution integral-field spectroscopy of exoplanets
Issue Date: 2019-11-26

High-resolution integral-field spectroscopy of exoplanets

Proefschrift

door

Sebastiaan Yannick Haffert

geboren te
Zoetemeer, Nederland
in 1992

An electronic copy of this thesis can be found at https://openaccess.leidenuniv.nl

*To my wife for her endless
support and dedication.*

"If I have seen further it is by standing on the shoulders of Giants."
-Isaac Newton

Contents

1 | Introduction

Almost three decades ago our perception of the universe changed drastically. The first planet around a star other than our own Sun had been found (Wolszczan & Frail, 1992). This system was and still is rather unique because the two planets are orbiting a pulsar, the remnant of a star after it has created a supernova. This fact puzzled astronomers because there were no known methods at that time for planets to survive a supernova. Another possibility was that they formed from the left-over debris (Rasio et al., 1992; Tavani & Brookshaw, 1992). The second shock came when the first exoplanet orbiting a solar-like star was discovered just three years later (Mayor & Queloz, 1995). The planet, 51 Pegasi b, is in a very short-period orbit of only 4.23 days and roughly half the mass of Jupiter. It was very surprising to find a planet comparable to Jupiter orbiting their host star much closer than that Mercury is orbiting around the Sun. More Jupiter-like planets on close-in orbits followed soon (Butler et al., 1997; Marcy & Butler, 1996). This class of gas-giant planets was quickly termed 'hot Jupiters' because the close proximity to their host star leads to high equilibrium temperatures.

In the years after these first few discoveries the field of exoplanet research quickly expanded. Many observing techniques and instruments were developed, leading to an explosive growth in the number of discovered planets, which can be seen in Figure 1.1. Most exoplanets to date have been found by the Kepler mission, which added almost 2500 planets. The Kepler mission used the transit method where stars are closely monitored to search for periodic dimmings when the planet moves in front of the star (Borucki et al., 2010; Henry et al., 2000). Kepler revealed that there are many exotic planets and planetary systems. A surprising find was the detection of many super-Earths and sub-Neptunes with masses of a few times that of the Earth (Petigura et al., 2013a,b). These types of planets are the most ubiquitous in the Milky Way even though our own Solar system does not have any of them (Petigura et al., 2013a,b).

Next to super Earths there are also less common but stranger planets like Kepler 51 b and d that have densities similar to cotton candy (Masuda, 2014) or the extremely hot KELT-9b that has gaseous iron and titanium in its atmosphere (Gaudi et al., 2017; Hoeijmakers et al., 2018b). Not only is there a large diversity in the planets themselves but there is also a large diversity in the composition of planetary systems: Trappist-1 has seven Earth-mass planets with short orbital periods around an M-dwarf star (Gillon et al., 2017), but HR8799 has four giant gas planets on very wide orbits (Marois et al., 2008, 2010).
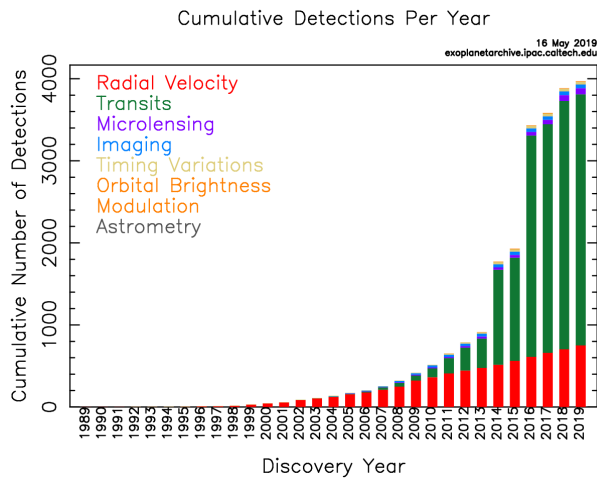
Figure 1.1: The amount of planets discovered by different observational techniques as a function of time. The number of planets found through radial velocity has been roughly linearly increasing with time. The amount of planets found by the transit method has exploded with obvious jumps in 2014 and 2017. In those years Kepler data were released, which shows the major impact Kepler had in the field of exoplanets. Other techniques are lagging behind in the number of detections. This graph was create with the NASA exoplanet archive on 16 May 2019.

This variety in exoplanets and planetary systems is challenging the theories of planet formation because the entire range of observed planetary-system architectures must be explained. The initial conditions for planet formation are set by the formation of the host star. Therefore the formation of planets cannot be understood independently from star formation. Stars are formed from clouds of molecular gas in the interstellar medium. Small overdensities in these large, cold clouds can create gravitational instabilities thath lead to the local collapse of the gas clouds into proto-stellar cores (McKee & Ostriker, 2007). If the collapsing gas has some angular momentum, it will flatten out the collapsing cloud and form a disk with the proto-star at its center. The surrounding dust and gas will gather into the circumstellar disk, which is thought to be the birth place of planets and is therefore also called a protoplanetary disk (Armitage & Belmonte, 2018). There are several proposed mechanism through which planets can form, and they broadly fall into one of the following three categories:

1. The planet forms through core accretion where small dust particles slowly coagulate into a proto-planetary core (Pollack et al., 1996). As the core grows, its gravity also grows, and it will attract more dust. When the proto-planet is massive enough it will start to rapidly accrete the gas and dust in its surrounding, thereby clearing out a path in the circumstellar disk through runaway accretion. This process stops when the proto-star becomes luminous enough to clear the disk through radiative pressure.

2. There are several mechanism through which the protoplanetary disk can become unstable and fragment into self-gravitating clumps. The most common method proposed for this are gravitational instabilities Boss (1997) that are created if the disk is very massive. But recent ALMA observations have revealed that massive disks are not very common, and this makes the gravitational instability process possibly a very rare event (Andrews et al., 2013; Pascucci et al., 2016). In the last few years it has been argued that magneto-rotational instabilities (MRI) may also cause disk fragmentation that leads to planet formation (Chiang & Youdin, 2010).

3. During the collapse of the pre-stellar core the clump of gas and dust can break up into separate clumps (Hennebelle & Chabrier, 2008). The separated clumps then can continue to contract and form planets. This scenario is very similar to the formation of binary star systems albeit with a more extreme mass ratio.

It is possible that all three processes play a part in the formation of planets. One of the challenges will be to determine which process dominates the formation process for which class of planets. It has been suggested that gas giants onwide orbits like those in the HR8799 system have been formed through gravitational instability (Nero & Bjorkman, 2009). However there is also contradicting evidence that their masses and separation do not fulfill several of the criteria for the formation through such instabilities (Bowler et al., 2015; Rameau et al., 2013; Vorobyov, 2013).

The interaction between the planet and the protoplanetary disk is thought to be quite complex (Kley, 2017). The planet can change its orbital distance, either moving in or out, due to planet-disk interaction. The more massive planets are able to sweep up a major part of the disk material in their orbit and carve a deep gap in the disk. The depletion of the dust and gas in the disk changes the pressure gradient and forces the planet to migrate; this migration scenario is called type-I migration (Kley, 2017; Nelson et al., 2000). Planets of a few Earth masses follow a different migration scenario called type II (Nelson et al., 2000) where only a small shallow gap is created that is not completely cleared of dust and gas. The main difference between the different types is the amount of matter that is accreted, and that determines whether the planet-disk interaction is linear (type II) or non-linear (type I). The case for multiple planets is more complicated since the planets will also influence each other, which is classified as type-III migration. In the past decades complex hydro-dynamical simulations have been conducted to understand the behaviour of migrating planets, leading to the development of semi-analytical relations between the migration rate, disk parameters and planet parameters (Dodson-Robinson & Salyk, 2011; Kley, 2017).

Theories of planet formation are currently tested by incorporating these semi-analytical relations, such as those for planetary migration, in a single global simulation environment (Benz et al., 2014; Mulders et al., 2018). Such codes try to replicate the observed exoplanet populations and are therefore called planet-population synthesis codes. Both the transit method and the radial velocity method mostly reveal old planetary systems because young stars produce a large quantity of astrophysical noise due to e.g. star spots or circumstellar material (Crockett et al., 2012; Lee, 2017; van Eyken et al., 2012; Yu et al., 2015). Therefore we can only compare the end state of the population synthesis codes and tweak the parameters until the simulations match the observed statistics. While this already has provided significant information about planet formation, we still have not verified

most of the physical mechanisms in these population codes (Morbidelli & Raymond, 2016).

Direct imaging plays an important role to overcome these observational limitations. By spatially resolving the disk and the embedded planets, we can witness their interaction. Another added benefit is the enhanced intrinsic contrast between the star and the planets. For old systems such as our own solar system, the best signal we could use to detect Earth or Jupiter from a distance is through reflected light. The intensity ratio between the Sun and the reflected light of Earth and Jupiter are 10^{-10} and 10^{-9}, respectively (Traub & Oppenheimer, 2010). This is a huge contrast to overcome. But during the first stages of planet formation, the planets are still very hot. This increases the intrinsic contrast in the Near-Infrared to $10^{-5} - 10^{-6}$ (Burrows et al., 2004) making the detection of such exoplanets orders of magnitude easier. This shows that direct imaging is the prime technique to observe young planetary systems and their planet-disk interactions.

1.1   The direct imaging challenge

1.1.1   The Earth atmosphere

Direct imaging of exoplanets is a challenging task because a high contrast needs to be reached at very close angular separations. If we place our solar system at 100 parsec, the resolving power necessary to separate Earth from the Sun would need to be better than 10 milliarcseconds (mas), but even if we could resolve Earth, the contrast between the Earth and the Sun of about 10^{-10} will make Earth close to impossible to observe. For Jupiter it becomes slightly easier with a separation of 55 mas and a contrast of $10^{-8} - 10^{-9}$. To resolve Earth and Jupiter at this distance we would need to use large telescopes of at least 30 meters in diameter, under the assumption that we will be able to solve the contrast-ratio problem. This angular resolving power will become available in the next decade with the construction of the upcoming extremely large telescopes; the Extremely Large Telescope (ELT) spearheaded by ESO, the Thirty Meter Telescope (TMT) and the Giant Magellan Telescope (GMT). But until those are build, we will have to use the current 8 and 10-meter class telescopes that are limited to about 26 mas angular resolution at 1 μm by diffraction,

$$\Delta\theta = 1.22\lambda/D. \tag{1.1}$$

Here $\Delta\theta$ is the angular resolving power, λ the wavelength that is used for imaging and D the telescope diameter. While the current generation of telescopes like the Very Large Telescope (VLT) of ESO, with an 8.2-meter diameter, would be able to resolve Jupiter at 100 pc, we have not been able to do this. For ground-based telescopes there are two challenges to overcome. The first being turbulence in the Earth's atmosphere, and the second is the intrinsic contrast between the planet and its host star. When light propagates from a star towards the Earth, it becomes a smooth plane wave due to the large distance between us and the star. It travels over several years to tens or hundreds of year,s and when it finally reaches Earth the light has to travel through the atmosphere to enter our telescopes. During the last tenth of a milliseconds of its journey the light wave loses its flatness because of turbulence in the atmosphere (Fried, 1966). This turbulence will create wavefront aberrations that degrade the resolving power of the telescope. The amount of wavefront aberration depends on the turbulence strength that is parametrised by the Fried parameter r_0 (Fried, 1966). The Fried parameter is the characteristic spatial scale of the perturbed wavefront where the wavefront changes by less than one radian. The resolution limit of the telescope is set by this characteristic scale instead of the telescope diameter. In median weather conditions the Fried parameter is roughly 20 to 30 cm at 1 μm for good observing sites such as Paranal, La Palma or Mauna Kea. The resolution that the VLT achieves during these condition is about 1 arcsecond, almost 40 times larger than the diffraction limit! This can be seen in Figure 1.2.

1.1.2 Adaptive optics

Almost 70 years ago Horace Babcock proposed the idea of adaptive optics to remove the effects of atmospheric turbulence (Babcock, 1953). A simple sketch of an adaptive optics (AO) system is shown in Figure 1.3. Every AO system contains an adaptive element that can change its shape in such a way that it compensates for the wavefront distortions caused by the atmosphere. Usually a deformable mirror (DM) is used because of its achromatic response. After reflecting of the DM surface, the wavefront has become flat again, and the telescope can reach its diffraction limit. The operation of such an AO system is complex, and several sub-systems are necessary. The most important sub-system is the wavefront sensor (WFS). Detectors in the visible and near-infrared can only measure the intensity of the light and not its phase. Therefore a specialized piece of optic, the wavefront sensor, is necessary to change the wavefront errors into intensity
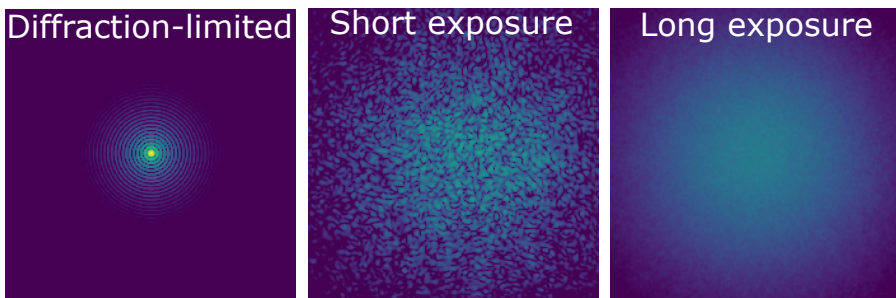
Figure 1.2: The effects of turbulence are shown here for an 8-meter class telescope with a seeing of 1 arcsecond. The left image shows the theoretical diffraction pattern for a circular telescope. In the centre an image is shown of a very short integration time effectively freezing the atmosphere during that time frame. The effects of turbulence are very apparent in this image, the Point-Spread-Function(PSF) is broken up into many individual speckles. A long integration where the PSF is averaged over many realizations of turbulence can be seen on the right. This seeing-limited PSF is smeared out over a large area reducing the resolving power.
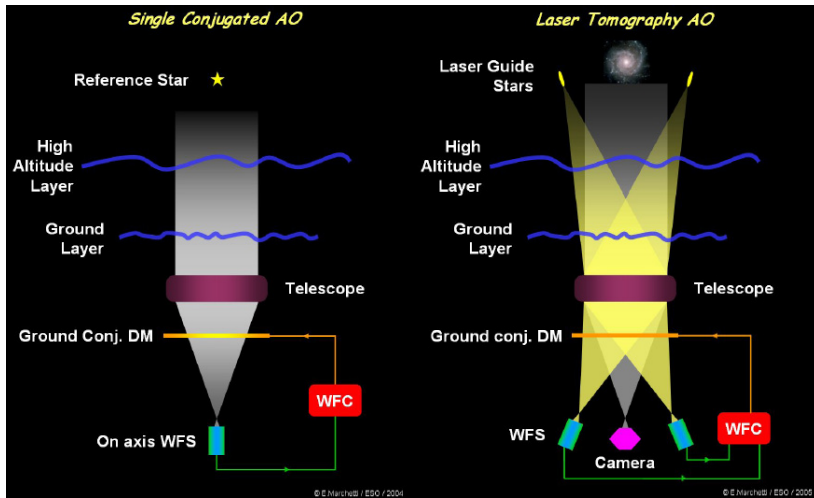
Figure 1.3:   These two figures show different types of adaptive optics.
The left uses the light from the astrophysical target itself to do wavefront
sensing, while the right scheme uses an artificial light source created by a
powerful laser that is reflected by the upper atmosphere. Both methods
drive a single deformable mirror to correct for the wavefront aberrations.
Image credit: ESO.

modulations on the detector. The standard AO system as drawn in Figure
1.3 uses a WFS to measure wavefront deviations and feeds those back to
the DM to create a closed-loop feedback system. The AO system needs to
operate at several hunderd Hz to several thousand Hz because of the time
scale over which the atmosphere changes (Greenwood, 1977). The coher-
ence time of the atmosphere τ_0 is roughly r_0, the Fried parameter, divided
by the wind speed v (Greenwood, 1977). This leads to a coherence time
on the order of 1 ms to 10 ms, which is why AO systems need to do the
corrections in real time.

The AO system that has been described here is a so called Single-
Conjugate Adaptive Optics (SCAO) system. In a SCAO system there is
one DM that is used for on-axis correction of the turbulence, and the light
of the target itself is used for wavefront sensing. The first generation of AO
instruments, NACO at the VLT (Lenzen et al., 2003; Rousset et al., 2003)
and NIRC2 at KECK (Wizinowich et al., 2000), began their operations
in the early 2000's. They all used the SCAO configuration because it is

relatively easy to implement and has the potential to provide the highest possible on-axis correction. Many astronomers used these early AO instruments for direct imaging while they had not been specifically developed for exoplanet science (Chauvin et al., 2005). The potential of AO instruments for direct imaging was proven by the detection of multiple planets around HR8799 (Marois et al., 2008, 2010). This system came as a surprise because most planets found until then were much closer to their host star, making HR8799 a still unique planetary system.

SCAO has worked very well for the purpose of improving the image quality but it is limited to bright targets because the light from the star itself is used to measure the wavefront errors created by the atmosphere. In the past two decades a large amount of work has been done to make AO-corrected images accessible for fainter targets. Instead of using the light from the astrophysical object an artificial light source is generated with a powerful laser high up in the atmosphere (Foy & Labeyrie, 1985; Fugate et al., 1991). For large telescopes a sodium laser is used to excite atoms in the sodium layer of Earth's atmosphere (Bonaccini Calia et al., 2010). The excited atoms will become an articial light beacon that can be used to measure the atmospheric turbulence. Due to the brightness of the laser it is not possible to bring the laser close to the astrophysical source, it needs to be pointed slightly away from the target. The atmospheric volume that is probed by this laser is slightly different than the volume that the star passes through. This led to the development of Laser Tomography Adaptive Optics (LTAO) where multiple laser guide-stars are placed around the target of interest (Hubin et al., 2005; Tallon & Foy, 1990). The measurements from the different lasers are then combined to create the best estimate of the on-axis wavefront errors. ESO applied this in the Adaptive Optics Facility (AOF) for the VLT that saw first light in 2015 (Madec et al., 2018). It has since then produced spectacular images, see for example Fig 1.4.

1.1.3   High-contrast imaging

The first generation of dedicated planet-hunting instruments SPHERE (Beuzit et al., 2019), GPI (Macintosh et al., 2014) and SCEXAO (Jovanovic et al., 2015) saw first light in 2013 and 2014. These instruments incorporated major instrumental advances to improve the performance for the detection and characterization of exoplanets. The AO systems contain DMs that have many more degrees of freedom operating above 1 kHz as opposed to the few hundred Hz of instruments such as NACO. These improvements allow for almost perfect correction and are therefore termed as Extreme Adaptive
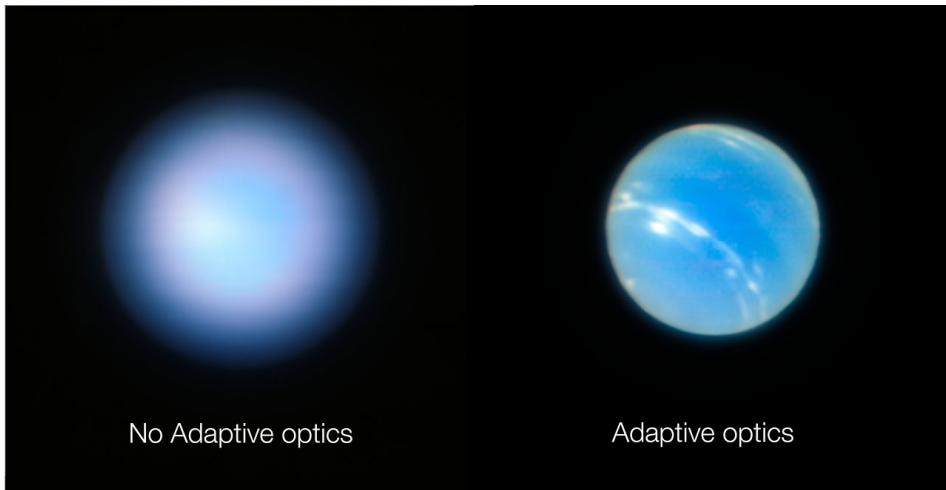
Figure 1.4:   Observations of Neptune with the new Narrow Field Mode
of MUSE with AO correction provided by the LTAO system. The LTAO
shows almost diffraction-limited performance. Image credits to ESO/P.
Weilbacher (AIP).

Optics (XAO). With the current generation of high-contrast imagers (HCI)
we can reach diffraction-limited performance in the near-infrared. But this
is not enough to find faint planets as the planet is still much fainter than
the Airy rings of the stellar diffraction pattern. With the high quality of
the PSFs of SPHERE and GPI they can also use advanced coronagraphs
to remove the diffraction effects of the star.

   A coronagraph is a specialized optical device that is designed as an
extreme angular filter; the on-axis starlight needs to be suppressed as much
as possible while leaving the off-axis planet light unaltered. One of the
first coronagraphs to be used for exoplanet imaging was the classical Lyot
coronagraph, originally developed to observe the solar corona outside of
a total solar eclipse (Lyot, 1939): an opaque disk with a size of a few
λ/D is added in the focal plane. This mask blocks part of the light, but
due to the hard edges of the mask, some of the on-axis light still diffracts
around it. Because the edge of the mask is much smaller than λ/D, this
diffracted light will scatter outside of the geometric pupil, which can then
be blocked by placing an additional aperture mask, the Lyot stop, in a
pupil after the focal-plane mas. The classical Lyot coronagraph reduces
the starlight by several orders of magnitude. More advanced focal-plane

masks have been developed that theoretically can remove all starlight if the input wavefront has no aberrations (Foo et al., 2005; Guyon, 2003; Rouan et al., 2000; Soummer, 2005). Another class of coronagraphs called pupil plane coronagraphs place masks in the pupil of the telescope to modify the shape of the PSF. By manipulating the amplitude or phase in the pupil, the electric field in the focal plane can be made to destructively interfere. With this technique dark holes can be created where we can search for planets, and because the optics are in the pupil, they are insensitive to vibrations. There are currently two flavours of pupil-plane coronagraphs, the Shaped Pupil (SP) coronagraph that uses amplitude masks (Kasdin et al., 2003; Soummer et al., 2003) and the Apodizing Phase Plate (APP) coronagraph that uses phase plates (Codona et al., 2006; Otten et al., 2017; Snik et al., 2012).

For Lyot-style coronagraphs the PSF needs to be perfectly aligned with the focal plane mask to cancel the starlight, but due to vibrations and small drifts the star will not be perfectly aligned with the mask. This deteriorates the performance of the coronagraph (Ruane et al., 2017). Pupil-plane coronagraphs are less sensitive to theses issues because the optical elements are in the pupil. Next to vibrations all other wavefront errors will also degrade the performance of the coronagraph (Aime & Soummer, 2004). There are still residual wavefront errors even though an AO system is used. The residual wavefront errors have two sources, the first being residual wavefront errors from the atmosphere that are not correctable or not completely removed. The second is due to a difference in the optical path between the coronagraphic optics and the wavefront-sensor optics. Because these instruments have different optics, they will see a slightly different wavefront error causing differential wavefront errors between the two systems. These wavefront errors are called Non-Common Path Aberrations (NCPAs). A lot of current research is focused on mitigating these NCPAs (Jovanovic et al., 2018). Both the NCPAs and the residual turbulence causes speckles that can look like planets. Image-processing algorithms are used to further remove these speckles.

1.1.4   Post-processing

To further enhance the contrast, advanced post-processing algorithms are used to minimize the starlight while leaving the planet light unaltered as much as possible. These techniques aim to model the PSF and speckle field of the star, which can then be subtracted from the image to reveal the planet. The most straightforward technique is to observe a reference

object and then subtract its PSF from the science target. Because this reference object is used to measure the PSF, it should not include any circumstellar material or companions. This technique is called Reference Differential Imaging (RDI) and was one of the first HCI techniques and was able to reveal the circumstellar disk around Beta Pictoris (Smith & Terrile, 1984). RDI has also been very successfully applied to Hubble Space Telescope (HST) data because HST has a very stable PSF (Schneider & Silverstone, 2003). If it is not possible to use a reference target, either due to unavailability or because the speckle pattern is not repeatable for different targets, a PSF model has to be built from the data itself. To create the reference PSF in this case, one needs to make use of a difference between the star and the planet.

The most successful method is based on angular rotation. The contributions from the star and planet can be separated when the field rotates but the pupil is stable because the star is on-axis and the planet is off-axis. During the rotation the PSF of the star will stay fixed in the image while the planet will rotate. The planet signal will therefore have a different temporal behaviour from the static speckles. The different observations are median combined, and because the planet is at different positions for every observation, it will not affect the median. The median-combined data are then a good model for the PSF. After subtracting the PSF model the data is derotated and combined to create the final image that can reveal faint point sources. This technique is called Angular Differential Imaging(ADI) and has been the most successful differential imaging technique for the detection of giant planets (Marois et al., 2006). ADI is quite a natural way of observing with an alt-azimuth telescope where the field will rotate due to the rotation of the Earth. Space-based telescopes usually employ different roll angles to rotate the image (Schneider & Silverstone, 2003). RDI and ADI require stable PSFs and speckle patterns, and depending on the speckle statistics either ADI or RDI reaches deeper constrast levels (Ruane et al., 2019). If the the speckle patterns change between observations, they will not be removed, and the achievable contrast limit is set by the speckle-noise limit (Aime & Soummer, 2004; Martinez et al., 2013). This is not an issue far away from the star as the speckles average out quite well, and the speckle noise limit is usually below the photon noise limits. But close to the star the speckles change slowly, and the photon-noise limit is many times higher due to the brightness of the Airy rings (Racine et al., 1999). Both RDI and ADI are therefore limited in power close to the diffraction limit. The effects of slowly evolving speckles can be seen in Figure 1.5
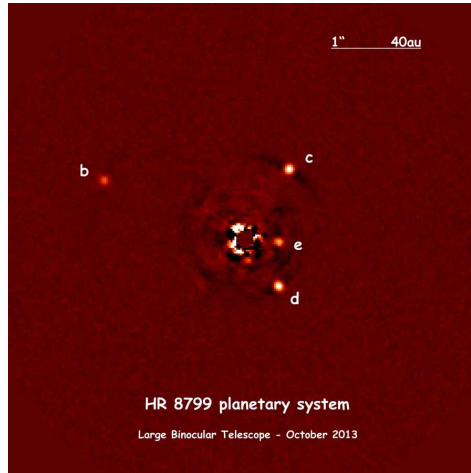
Figure 1.5: An observation of the HR8799 system taken with the LBT (Maire et al., 2015) and post-processed with Angular Differential Imaging. The four planets orbiting the star are clearly resolved. Searching for planets closer in is difficult due to slowly changing speckles that limit how close in we can search. The speckle noise can be seen at the edge of the coronagraphic mask were the intensity quickly changes from white to black.

where limited improvement is achieved close to the star. Diversities that are based on the intrinsic properties of the observed system that are time invariant would be more robust against these varying speckles.

1.1.5 The powers of ten in exoplanet spectroscopy

Evolutionary models of exoplanets predicted a strong methane signal similar to field brown dwarfs (Baraffe et al., 2003). Simultaneous Differential Imaging takes advantage of this difference by observing in two narrowband filters (Marois et al., 2005; Racine et al., 1999). One narrowband filter targeting the methane absorption band at 1.62 μm and one just outside of the band to measure the continuum. The difference between the two observations should reveal the planet. Although SDI in the methane feature looked like a promising technique, it has not been fruitful (Biller et al., 2007). Recent work shows that planets typically do not contain strong methane absorption features (Konopacky et al., 2013; Petit dit de la Roche et al., 2018; Skemer et al., 2014). A feature that is promising and has shown success is the emission of hydrogen. Hα emission is one of the strongest

signposts of a planet in formation (Aoyama et al., 2018; Marleau et al., 2017; Zhu, 2015), which occurs when gas is deposited onto the planet at high velocity. As the gas collides with the planet, it creates a strong shock front, which heats up the local gas to high temperatures (T>10000 K). This process generates a large amount of Hα emission, which decreases the contrast between the star and planet by several orders of magnitude, thereby making it easier to detect. The difference between two narrowband filters with one covering Hα and the other in the nearby continuum can be used to subtract out the star (Close et al., 2014).

A higher-resolution version of this is Spectral Differential Imaging, (having the same abbreviation as Simultaneous Differential Imaging). With SDI the PSF is measured at many wavelengths, usually with a low-resolution integral-field spectrograph at a resolving power of $R = 50 - 100$ over a large bandwidth. Due to the properties of diffraction the PSF and its speckles scale radially with wavelength while the planet stays at a fixed position (Sparks & Ford, 2002; Thatte et al., 2007). Rescaling the data to a reference wavelength will overlay the speckles while smearing out the planet. Taking a median as is done with ADI will create a PSF model that can be used for subtraction. Some planet signal is also subtracted by this procedure; the amount of planet subtraction depends on the observed bandwidth and the angular distance of the planet. SDI has the advantage that it can remove the starlight and at the same time characterize the planet at low resolving power. This is very powerful because it provides a spectrum of the planet. Usually both SDI techniques are combined with ADI into sADI to make use of both diversities at the same time. The combined technique of sADI has allowed us to reach the deepest contrasts ever observed (Vigan et al., 2015).

Spectral resolving powers of the order of a few thousand can distinguish between the molecular bands and spectral lines of the star and planet due to the intrinsic difference of their sources (Barman et al., 2015; Hoeijmakers et al., 2018a; Konopacky et al., 2013). An example of the spectral differences at various spectral resolutions of a solar-like star and a giant planet are shown in Figure 1.6. Spectral filters tuned to the host star can be used to remove the starlight while leaving the exoplanet's spectrum largely undisturbed. After removing the starlight a matched-filter is used to combine the various spectral lines of the planet across the spectral range to increase the signal-to-noise. This technique has been used in the Near-Infrared to search for the signatures of different molecules and therefore was coined as Molecule Mapping (Hoeijmakers et al., 2018a). A distinct
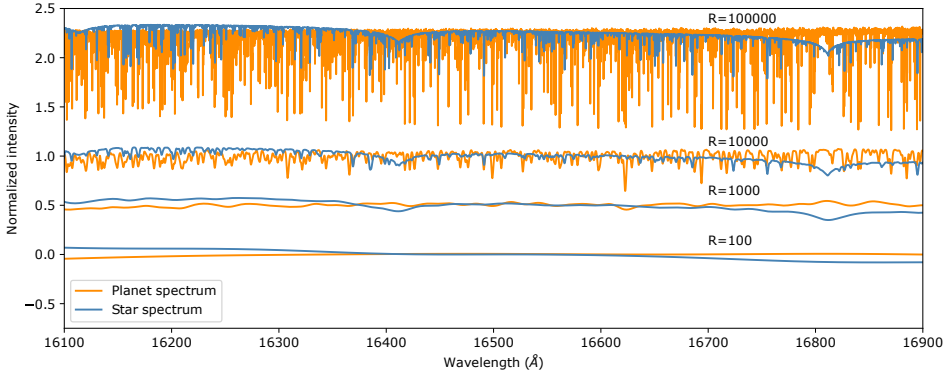
Figure 1.6: The spectrum of a solar-like star modelled with a 6000 K PHOENIX model and a spectrum of a giant planet modelled by a 1200 K BTSettl model. The resolving power changes by one order of magnitude between the different spectra, going from R=100000 to R=100. The spectra are shifted for ease of viewing. As the spectral resolving power decreases, it becomes more difficult to discriminate the planetary spectrum from the stellar spectrum.

advantage of this technique is that it is not limited by speckle noise, which hampers the other post-processing techniques.

An even higher spectral resolving power that is of the order of tens of thousands to a hundred thousand resolves individual spectral lines. This increases the capability to discriminate between the planet and stellar features. Due to the high resolving power small Doppler shifts on the order of a few km/s will also become visible. The dynamics of the orbital motion can then be used as an additional difference to disentangle the planet from the star (Charbonneau et al., 1999; Snellen et al., 2010). The orbital difference, without spatially resolving the companion, has been successfully applied to study several hot giant gas planets, in which many atomic and molecular species like water, CO (Birkby et al., 2013; Brogi et al., 2014, 2013) and even gaseous iron have been found (Hoeijmakers et al., 2018b). Even the spin rate and atmospheric dynamics of planetary atmospheres can be measured by carefully analysing the line profiles (Snellen et al., 2010). Because the signal-to-noise ratio grows as $\sqrt{R}$ for unresolved lines, it helps to increase the spectral resolution (Sparks & Ford, 2002). The downside is that for a fixed detector size the spectral range or the field of view will be severly limited.

1.2   Thesis outline

The goal of this thesis is to explore the potential of high-resolution integral-field spectroscopy behind a high-contrast imaging instrument for the detection and characterization of exoplanets. The work presented in this thesis can be divided into three parts, the first one focused on coupling a high-contrast imager with a high-resolution spectrograph (R≈100000). The second part shows the scientific gain of integral-field spectroscopy in the visible for high-contrast imaging. And the last part is about a novel way to do spectroscopy with applications for astronomy and Earth observations.

Chapter 2 and 3: The Leiden EXoplanet Instrument(LEXI)
These two chapters present the design, development and on-sky results of the Leiden EXoplanet Instrument (LEXI) a bench-mounted visitor instrument for the 4.2m William Herschel Telescope at La Palma. LEXI was built as a test bed for high-contrast imaging and integral-field spectroscopy. Several different approaches to AO-fed spectroscopy have been tested with LEXI. Our results show that XAO systems are well suited for single-mode fiber spectroscopy. LEXI has also been used to test several wavefront sensing concepts such as the generalised Optical Differentiation Wavefront Sensor (g-ODWFS) (Haffert (2016), Haffert et. al. in prep.), the Coronagraphic Modal Wavefront Sensor (Wilby et al., 2016, 2017) and more recently the Three Wave Shearing Interferometer (TWSI) (Por et al. in prep.).

Chapter 4 and 5: SCAR
These two chapters present the Single-mode Complex Amplitude Refiner (SCAR) coronagraph. SCAR is a promising new coronagraph that makes use of the mode-filtering capabilities of single-mode fibers. This allows us to design and create coronagraphs with higher planet throughput that can search closer to the star. In chapter 5 we present the concept, designs and performance estimates where we show that SCAR enables coronagraphs with inner-working angles close to the diffraction limit. In chapter 6 we experimentally demonstrate the nulling capabilities of SCAR for two differently designs in the lab where we reached a 10^{-4} contrast at 1 λ/D.

Chapter 6: Imaging a forming multi-planet system
This chapter presents the results of High-Resolution Spectral Differential Imaging applied to the system PDS 70 that was observed by MUSE during the commissioning of its new narrow-field mode. MUSE is a medium-

resolution integral-field unit that spans the wavelength range from 0.465μm to 0.93μm at an average resolving power of $R = \lambda/\Delta\lambda = 3000$. The instrument is fed by the LTAO system on UT4 of the VLTs and can reach a spatial resolution of roughly 60 milliarcseconds in good seeing conditions. The combination of the spectral resolving power and the AO performance made it possible to detect two accreting proto-planets in the transition disk around PDS 70. Our observations show that adaptive-optics-assisted, medium-resolution, integral-field spectroscopy with MUSE targeting accretion signatures is a powerful way to trace ongoing planet formation in transitional disks at different stages of their evolution. This was also the first time that a planet has been discovered with an LTAO system, which is very interesting as LTAO can reach a better performance on fainter targets than comparable SCAO systems.

Chapter 7: Novel spectroscopic instrumentation

This chapter presents a novel spectrograph concept based on Volume Bragg Gratings (VBG) that is able to achieve high spectral resolution over a large wavelength range for a large field of view without the need for very large detectors. This is achieved by creating specialized spectral filters with highly multiplexed VBGs (HMBG) that are sensitive to a molecular species of choice. The HMBG condenses the full spectrum into a small, multiplexed spectrum with the size of a single spectral line thereby enabling a large reduction of the required detector real estate per spatial pixel. The chapter presents the concept and a few case studies.

1.3   Outlook

Medium to high-resolution spectroscopy will be a powerful addition to the current and future generation of high-contrast imaging instruments as is demonstrated by the discovery of the second planet in the PDS 70 system (Chapter 6). Our solution to add this capability is to couple high-contrast imaging instruments to spectrographs with single-mode fibers, because they can reduce the complexity of the spectrograph (Chapters 2 and 3) while also enabling improved coronagraph designs with smaller inner-working angles and higher throughput as we have demonstrated with SCAR (Chapters 4 and 5). The success of high-resolution spectroscopy lies in its capability to separate the continuum effects, such as speckle noise, from spectral line features. This does not have to be done in post-processing but can also be done

optically (Chapter 7), and therefore we can reduce the number of required detector pixels per spatial point. With the multiplexed Bragg gratings we can apply the same technique to much larger fields of view and bypass the field-of-view limitation of high-resolution integral-field spectroscopy.

Medium to high-resolution integral-field spectroscopy is likely to be the ideal observing technique to search for accretion signatures from proto-planets. The current standard is to search for Hα emission with Simultaneous Differential Imaging, effectively resulting in resolving powers on the order of $10 - 100$. Signatures such as Hα are intrinsically narrowband, therefore increasing the spectral resolving power of our observations increases the signal-to-noise ratio as long as the line is not resolved. Adding the capability to observe these signatures at much higher resolving power $R = 5000 - 10000$ will increase the signal-to-noise ratio by a factor 10-100 almost for free. MUSE at the VLT does have the capability of integral-field spectroscopy but it was not designed for high-contrast imaging, and therefore lacks the capability for starlight suppression. Development of high-resolution integral-field units for extreme adaptive optics systems will allow us to take the next step in the search and characterization of proto-planets, where we will be able to not only find such planets more efficiently but also can study the process of accretion in detail.

Currently MUSE provides an exciting opportunity to study the time variability of accretion signals from short to long timescales. Such observations will set strong constraints on planet growth and evolution during the earlier stages. In addition due to the unique broad spectral coverage of MUSE, we can observe other accretion tracers such as Hβ at 4861Å, OI at 8446Å, and the CaII triplet at 8498Å, 8542Å, and 8662Å. Together with Hα, the detection of any these tracers will put constraints on the temperature, density and shock velocity at the interface between the planet and the accretion flow.

This work at medium resolution lays down the foundation for visible-light high-resolution integral-field units and high-contrast imaging for the detection of reflected light from cold and old exoplanets, like Earth, and biosignatures such as the O$_2$ band with the Extremely Large Telescopes (ELT). High-resolution spectroscopy for exoplanets is a photon-starved observing technique. The detection limits are therefore set by the amount of light that we can collect from the star and the planet. Proxima Centauri b could be characterized with the current telescopes but almost a hundred nights spread over three years are necessary to guarantee a detection (Lovis et al., 2017). The effective observing time can be drastically lowered

by using one of the ELTs. ELTs come with two advantages, the first being the larger collecting area, and the second is the increased spatial resolution. With an ELT the detection of Proxima Centauri b can obtained in a single night instead of the hundred nights of VLT time (Snellen et al., 2015). With the addition of high-resolution integral-field units to extreme adaptive optics systems at ELTs, we will start to study older, potentially habitable planets, and thus address humanity's ultimate question: Are we alone?

Bibliography

Aime, C., & Soummer, R. 2004, ApJ, 612, L85

Andrews, S. M., Rosenfeld, K. A., Kraus, A. L., & Wilner, D. J. 2013, ApJ, 771, 129

Aoyama, Y., Ikoma, M., & Tanigawa, T. 2018, ApJ, 866, 84

Armitage, P. J., & Belmonte, J. A. 2018, A Brief Overview of Planet Formation (Cham: Springer International Publishing), 2185–2203. `https://doi.org/10.1007/978-3-319-55333-7_135`

Babcock, H. W. 1953, PASP, 65, 229

Baraffe, I., Chabrier, G., Barman, T. S., Allard, F., & Hauschildt, P. H. 2003, A&A, 402, 701

Barman, T. S., Konopacky, Q. M., Macintosh, B., & Marois, C. 2015, ApJ, 804, 61

Benz, W., Ida, S., Alibert, Y., Lin, D., & Mordasini, C. 2014, in Protostars and Planets VI, ed. H. Beuther, R. S. Klessen, C. P. Dullemond, & T. Henning, 691

Beuzit, J. L., Vigan, A., Mouillet, D., et al. 2019, arXiv e-prints, arXiv:1902.04080

Biller, B. A., Close, L. M., Masciadri, E., et al. 2007, ApJS, 173, 143

Birkby, J. L., de Kok, R. J., Brogi, M., et al. 2013, MNRAS, 436, L35

Bonaccini Calia, D., Feng, Y., Hackenberg, W., et al. 2010, The Messenger, 139, 12

Borucki, W. J., Koch, D., Basri, G., et al. 2010, Science, 327, 977

Boss, A. P. 1997, Science, 276, 1836

Bowler, B. P., Liu, M. C., Shkolnik, E. L., & Tamura, M. 2015, ApJS, 216, 7

Brogi, M., de Kok, R. J., Birkby, J. L., Schwarz, H., & Snellen, I. A. G. 2014, A&A, 565, A124

Brogi, M., Snellen, I. A. G., de Kok, R. J., et al. 2013, ApJ, 767, 27

Burrows, A., Sudarsky, D., & Hubeny, I. 2004, ApJ, 609, 407

Butler, R. P., Marcy, G. W., Williams, E., Hauser, H., & Shirts, P. 1997, ApJ, 474, L115

Charbonneau, D., Noyes, R. W., Korzennik, S. G., et al. 1999, ApJ, 522, L145

Chauvin, G., Lagrange, A. M., Dumas, C., et al. 2005, A&A, 438, L25

Chiang, E., & Youdin, A. N. 2010, Annual Review of Earth and Planetary Sciences, 38, 493

Close, L. M., Follette, K. B., Males, J. R., et al. 2014, ApJ, 781, L30

Codona, J. L., Kenworthy, M. A., Hinz, P. M., Angel, J. R. P., & Woolf, N. J. 2006, in Society of Photo-Optical Instrumentation Engineers (SPIE) Conference Series, Vol. 6269, 62691N

Crockett, C. J., Mahmud, N. I., Prato, L., et al. 2012, ApJ, 761, 164

Dodson-Robinson, S. E., & Salyk, C. 2011, ApJ, 738, 131

Foo, G., Palacios, D. M., & Swartzland er, Grover A., J. 2005, Optics Letters, 30, 3308

Foy, R., & Labeyrie, A. 1985, A&A, 152, L29

Fried, D. L. 1966, Journal of the Optical Society of America (1917-1983), 56, 1372

Fugate, R. Q., Fried, D. L., Ameer, G. A., et al. 1991, Nature, 353, 144

Gaudi, B. S., Stassun, K. G., Collins, K. A., et al. 2017, Nature, 546, 514

Gillon, M., Triaud, A. H. M. J., Demory, B.-O., et al. 2017, Nature, 542, 456

Greenwood, D. P. 1977, Journal of the Optical Society of America (1917-1983), 67, 390

Guyon, O. 2003, A&A, 404, 379

Haffert, S. Y. 2016, Optics Express, 24, 18986

Hennebelle, P., & Chabrier, G. 2008, ApJ, 684, 395, doi: 10.1086/589916

Henry, G. W., Marcy, G. W., Butler, R. P., & Vogt, S. S. 2000, ApJ, 529, L41

Hoeijmakers, H. J., Schwarz, H., Snellen, I. A. G., et al. 2018a, A&A, 617, A144

Hoeijmakers, H. J., Ehrenreich, D., Heng, K., et al. 2018b, Nature, 560, 453

Hubin, N., Arsenault, R., Conzelmann, R., et al. 2005, Comptes Rendus Physique, 6, 1099

Jovanovic, N., Martinache, F., Guyon, O., et al. 2015, PASP, 127, 890

Jovanovic, N., Absil, O., Baudoz, P., et al. 2018, in Society of Photo-Optical Instrumentation Engineers (SPIE) Conference Series, Vol. 10703, Adaptive Optics Systems VI, 107031U

Kasdin, N. J., Vanderbei, R. J., Spergel, D. N., & Littman, M. G. 2003, ApJ, 582, 1147

Kley, W. 2017, arXiv e-prints, arXiv:1707.07148

Konopacky, Q. M., Barman, T. S., Macintosh, B. A., & Marois, C. 2013, Science, 339, 1398

Lee, C.-H. 2017, Research Notes of the AAS, 1, 41

Lenzen, R., Hartung, M., Brandner, W., et al. 2003, in Proc. SPIE, Vol. 4841, Instrument Design and Performance for Optical/Infrared Ground-based Telescopes, ed. M. Iye & A. F. M. Moorwood, 944–952

Lovis, C., Snellen, I., Mouillet, D., et al. 2017, A&A, 599, A16

Lyot, B. 1939, MNRAS, 99, 580

Macintosh, B., Graham, J. R., Ingraham, P., et al. 2014, Proceedings of the National Academy of Science, 111, 12661

Madec, P. Y., Arsenault, R., Kuntschner, H., et al. 2018, in Society of Photo-Optical Instrumentation Engineers (SPIE) Conference Series, Vol. 10703, Adaptive Optics Systems VI, 1070302

Maire, A. L., Skemer, A. J., Hinz, P. M., et al. 2015, A&A, 576, A133

Marcy, G. W., & Butler, R. P. 1996, ApJ, 464, L147

Marleau, G.-D., Klahr, H., Kuiper, R., & Mordasini, C. 2017, ApJ, 836, 221

Marois, C., Doyon, R., Nadeau, D., et al. 2005, PASP, 117, 745

Marois, C., Lafrenière, D., Doyon, R., Macintosh, B., & Nadeau, D. 2006, ApJ, 641, 556

Marois, C., Macintosh, B., Barman, T., et al. 2008, Science, 322, 1348

Marois, C., Zuckerman, B., Konopacky, Q. M., Macintosh, B., & Barman, T. 2010, Nature, 468, 1080

Martinez, P., Kasper, M., Costille, A., et al. 2013, A&A, 554, A41

Masuda, K. 2014, ApJ, 783, 53

Mayor, M., & Queloz, D. 1995, Nature, 378, 355

McKee, C. F., & Ostriker, E. C. 2007, ARA&A, 45, 565

Morbidelli, A., & Raymond, S. N. 2016, Journal of Geophysical Research (Planets), 121, 1962

Mulders, G. D., Pascucci, I., Apai, D., & Ciesla, F. J. 2018, AJ, 156, 24

Nelson, R. P., Papaloizou, J. C. B., Masset, F., & Kley, W. 2000, Monthly Notices of the Royal Astronomical Society, 318, 18

Nero, D., & Bjorkman, J. E. 2009, ApJ, 702, L163

Otten, G. P. P. L., Snik, F., Kenworthy, M. A., et al. 2017, ApJ, 834, 175

Pascucci, I., Testi, L., Herczeg, G. J., et al. 2016, ApJ, 831, 125

Petigura, E. A., Howard, A. W., & Marcy, G. W. 2013a, Proceedings of the National Academy of Science, 110, 19273

Petigura, E. A., Marcy, G. W., & Howard, A. W. 2013b, ApJ, 770, 69

Petit dit de la Roche, D. J. M., Hoeijmakers, H. J., & Snellen, I. A. G. 2018, A&A, 616, A146

Pollack, J. B., Hubickyj, O., Bodenheimer, P., et al. 1996, Icarus, 124, 62

Racine, R., Walker, G. A. H., Nadeau, D., Doyon, R., & Marois, C. 1999, PASP, 111, 587

Rameau, J., Chauvin, G., Lagrange, A. M., et al. 2013, A&A, 553, A60

Rasio, F. A., Shapiro, S. L., & Teukolsky, S. A. 1992, Astronomy and Astrophysics, 256, L35

Rouan, D., Riaud, P., Boccaletti, A., Clénet, Y., & Labeyrie, A. 2000, PASP, 112, 1479

Rousset, G., Lacombe, F., Puget, P., et al. 2003, in Proc. SPIE, Vol. 4839, Adaptive Optical System Technologies II, ed. P. L. Wizinowich & D. Bonaccini, 140–149

Ruane, G., Mawet, D., Jewell, J., & Shaklan, S. 2017, in Society of Photo-Optical Instrumentation Engineers (SPIE) Conference Series, Vol. 10400, Society of Photo-Optical Instrumentation Engineers (SPIE) Conference Series, 104000J

Ruane, G., Ngo, H., Mawet, D., et al. 2019, AJ, 157, 118

Schneider, G., & Silverstone, M. D. 2003, in Proc. SPIE, Vol. 4860, High-Contrast Imaging for Exo-Planet Detection., ed. A. B. Schultz, 1–9

Skemer, A. J., Marley, M. S., Hinz, P. M., et al. 2014, ApJ, 792, 17

Smith, B. A., & Terrile, R. J. 1984, Science, 226, 1421

Snellen, I., de Kok, R., Birkby, J. L., et al. 2015, A&A, 576, A59

Snellen, I. A. G., de Kok, R. J., de Mooij, E. J. W., & Albrecht, S. 2010, Nature, 465, 1049

Snik, F., Otten, G., Kenworthy, M., et al. 2012, in Society of Photo-Optical Instrumentation Engineers (SPIE) Conference Series, Vol. 8450, Modern Technologies in Space- and Ground-based Telescopes and Instrumentation II, 84500M

Soummer, R. 2005, ApJ, 618, L161

Soummer, R., Aime, C., & Falloon, P. E. 2003, A&A, 397, 1161

Sparks, W. B., & Ford, H. C. 2002, ApJ, 578, 543

Tallon, M., & Foy, R. 1990, A&A, 235, 549

Tavani, M., & Brookshaw, L. 1992, Nature, 356, 320

Thatte, N., Abuter, R., Tecza, M., et al. 2007, MNRAS, 378, 1229

Traub, W. A., & Oppenheimer, B. R. 2010, Direct Imaging of Exoplanets (University of Arizona Press), 111–156

van Eyken, J. C., Ciardi, D. R., von Braun, K., et al. 2012, ApJ, 755, 42

Vigan, A., Gry, C., Salter, G., et al. 2015, MNRAS, 454, 129

Vorobyov, E. I. 2013, A&A, 552, A129

Wilby, M. J., Keller, C. U., Haffert, S., et al. 2016, in Society of Photo-Optical Instrumentation Engineers (SPIE) Conference Series, Vol. 9909, Adaptive Optics Systems V, 990921

Wilby, M. J., Keller, C. U., Snik, F., Korkiakoski, V., & Pietrow, A. G. M. 2017, A&A, 597, A112

Wizinowich, P., Acton, D. S., Shelton, C., et al. 2000, PASP, 112, 315

Wolszczan, A., & Frail, D. A. 1992, Nature, 355, 145

Yu, L., Winn, J. N., Gillon, M., et al. 2015, ApJ, 812, 48

Zhu, Z. 2015, ApJ, 799, 16

2 | The Leiden Exoplanet Instrument (LEXI): a high-contrast high-dispersion spectrograph

The Leiden EXoplanet Instrument (LEXI) will be the first instrument designed for high-contrast, high-dispersion integral field spectroscopy at optical wavelengths. High-contrast imaging (HCI) and high-dispersion spectroscopy (HDS) techniques are used to reach contrasts of 10^{-7}. LEXI will be a bench-mounted, high dispersion integral field spectrograph that will record spectra in a small area around the star with high spatial resolution and high dynamic range. A prototype is being setup to test the combination of HCI+HDS and its first light is expected in 2016.

2.1   Introduction

One of the major drivers for current astronomical instrumentation development is the direct detection and characterization of Earth-like exoplanets. These developments are largely focused on improving high-contrast imaging techniques. But with the recent improvements of Extreme Adaptive Optics (AO) and coronagraphy (Jovanovic et al., 2015; Macintosh et al., 2014; Vigan et al., 2016), it is now possible to directly detect hot, self-luminous exoplanets. The current generation of high-contrast imaging instruments deliver a contrast between 10^4 and 10^6 after careful data reduction. The fundamental limit of raw contrast on ground-based telescopes is set by the AO system (Guyon, 2005). For 8-meter class telescopes this is roughly 10^6. Earth-like exoplanets have a contrast on the order of 10^{10}, which makes it necessary to have techniques that can bridge the gap between the AO contrast limits and the contrast of Earth-like planets.

Another technique to characterize exoplanets was developed at the same time as the HCI techniques. This technique makes use of the fact that the light of the planet is Doppler-shifted with respect to the star light. With a high-resolution spectrograph the stellar light can then be removed to extract the planet light. This method has already been successfully used to characterize several exoplanets (Brogi et al., 2012; Snellen et al., 2010). This high-dispersion spectroscopy technique has reached contrast limits of 10^5.

Recently Snellen et al. (Snellen et al., 2015) proposed to combine high-contrast imaging with high-resolution spectroscopy. High-contrast imaging reduces the contrast between a star and its circumstellar environment; and high-resolution spectroscopy can then be used to remove the residual starlight. If we could reach 10^5 with HCI and 10^5 with HDS, then the combined contrast could reach 10^{10}. The assumption here is that the two methods directly add their powers. The Leiden EXoplanet Instrument(LEXI) is the first instrument that will combine high-resolution spectroscopy with high-contrast imaging techniques in the visible. The main purpose will be to test the combination of HCI+HDS and see if we can directly add the achieved contrast limits of the individual techniques. LEXI is a visiting instrument for the 4.2m William Herschel Telescope (WHT) on La Palma.

The current version of LEXI is a prototype. This LEXI prototype will be operated in two observing modes simultaneously. The first observing mode is a high-resolution imaging camera for measuring non-common path errors and for high-contrast imaging. The second observing mode is a high-resolution long-slit spectrograph. Both are fed by an AO-corrected beam.

Because our main targets are binary stars and standard stars, we need a derotator to keep the field fixed. At the William Herschel Telescope, we use the facility UV/optical derorator. In the next subsections each module of the prototype is discussed, and several design choices for the prototype instrument are described.

2.2   Prototype optical design

2.2.1   LEXI Adaptive optics system

The adaptive optics module of LEXI was originally designed for ExPo (Rodenhuis et al., 2012). Because ExPo is a polarimetric imager, the AO module was designed to minimize the instrumental polarization. It sits on a customized breadboard at the focal plane of the WHT Nasmyth focus. There a 140 mm lens collimates the beam to a 12.7 mm pupil onto the deformable mirror, an Alpao DM 97-15. The deformable mirror is a high-speed, high-stroke DM with an operating frequency of up to 900 Hz. The stroke of the deformable mirror is 60 μm, which enables it to remove large aberrations in the system including tipt and tilt introduced by telescope tracking errors and the atmosphere. The beam is redirected by a second fold mirror. The angle that the DM and the fold mirror make with the optical axis were minimized to decrease the instrumental polarization. The beam is then focused by a lens that is identical to the collimation lens. This creates a 1:1 reimaing system between the AO input and output.

A 50:50 polarizing beam splitter with a VIS anti-reflection coating was put in the focus of the AO output beam. This divides the light between the wavefront sensor and the science arm. A polarizing beam splitter was chosen over a non-polarizing beam splitter because the optics in the science arm required a polarized input, and a polarizing beam splitter then provides the highest possible efficiency for the instrument. Due to the geometry of the beam splitter vertically polarized light is sent to the wavefront sensor and horizontally polarized light to the science arm.

A Shack-Hartmann wavefront sensor provides data to the control system. The light from the beam splitter is collimated by a 60-mm achromatic doublet. The collimated pupil of the telescope is then sampled by microlens array. The pitch of the microlenses is 500 μm, leading to 11 microlenses across the pupil. The images created by the microlenses are then reimaged by a pair of lenses onto an Andor Ixon 870 EMCCD camera with sub-electron read noise and the ability to cool to -80 degree Celsius, which
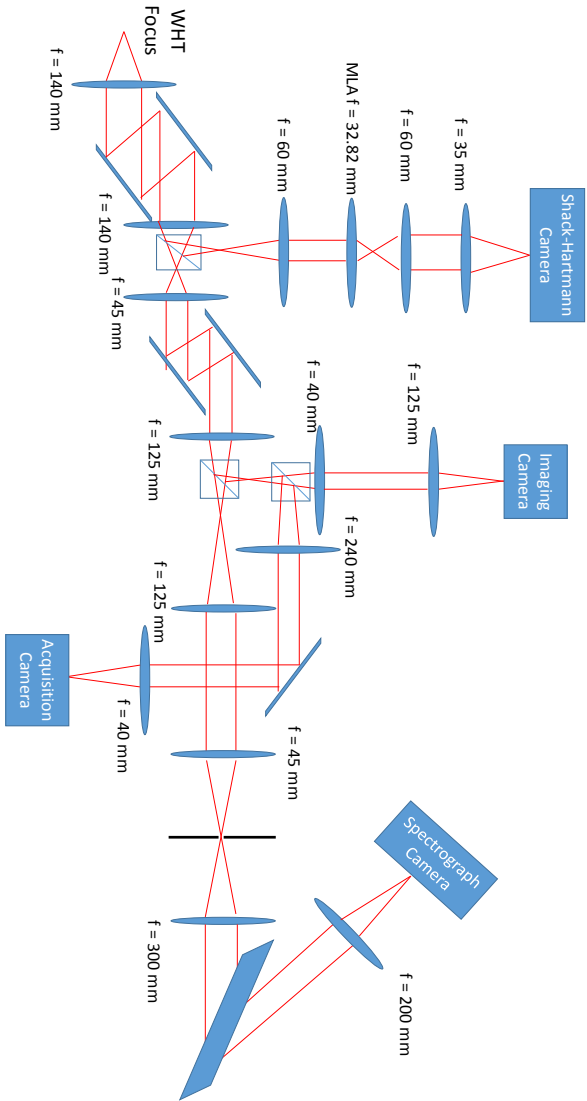
Figure 2.1: A sketch of the LEXI prototype as used at the William Herschel Telescope. The focal lengths of the lenses are shown next to the lens. The instrument can globally divided into three parts. The AO module, the high contrast imaging module and the spectrograph module.
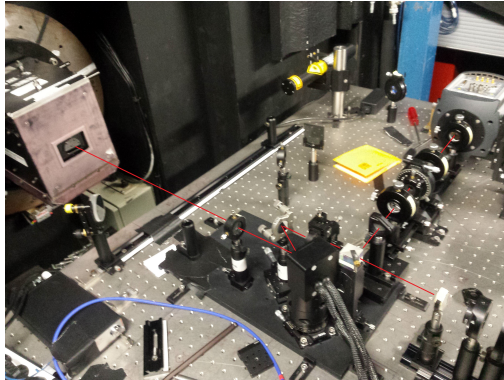
Figure 2.2: AO system as it was set up in GHRILL at the William Herschel Telescope. The red line shows the path of the light.

eliminates dark noise. The camera has 128 by 128 pixels with a 16 μm pixel size. Each subaperture image is thus sampled by 8 pixels. Due to the size of the secondary mirror of the WHT and partially illuminated subapertures, we could determine 80 useful sub-apertures for on-sky wavefront sensing. The setup of the AO system can be seen in Figure 2.2.

The AO system has two focal planes where spatial filters can be inserted. These spatial filters are used together with an internal light source for calibrations. The wavefront sensor arm is calibrated by using a 10 μm pinhole in the second focal plane. This creates a point source input for the wavefront sensor. The point source is then chosen as a reference flat wavefront. The reference is necessary for a SHWFS because it measures spot displacements with respect to a certain zero point.

The second part of the calibrations consists in determining the inter-action matrix between the deformable mirror and the wavefront sensor. For this calibration we place a pinhole in the first focus as this creates a point source input for the whole AO system. A single column of the in-teraction matrix is the response to the wavefront mode that is applied to the deformable mirror. The mode response is calibrated by applying the mode with a positive amplitude and a negative amplitude. The difference between these two creates an estimate for the response slope of the mode. Currently the DM can be controlled in an actuator basis, where each ac-tuator is controlled independently, in a Karhunen-Loeve basis or a Zernike basis. The Karhunen-Loeve basis is the standard in which the AO system is operated. Because the alignment of the optical system is not perfect, this

calibration procedure needs to be iterated a few times. Each time a new calibration is done, the AO is operated in closed loop to remove the aberrations before a new calibration iteration is done. With this iterative scheme any large aberration that is present due to misalignments of the optics or due to initial non-flatness of the deformable mirror can be removed.

2.2.2   Non-common path correction and coronagraph

The second part of the instrument is used for the creation of phase patterns with a Spatial Light Modulator (SLM). The SLM can create phase patterns by applying different voltages to it's pixels. The SLM is a Boulder Nonlinear Systems 512 by 512 SLM XY series with a pixel pitch of 15 μm and a 83.4% fill factor. Because the SLM is polarization sensitive, it needs to have a vertically polarized input for phase modulation. If the light is not perfectly vertically polarized, the SLM will also create amplitude modulations.

The polarizing beam splitter creates a horizontally polarized input for the SLM. A re-imaging arm was placed between the AO output and the SLM input. This re-imaging arm consists of two identical achromatic doublets with a focal length of 50 mm. A zero-order half-wave plate was placed in the intermediate pupil plane to rotate the polarization from horizontal to vertical. Because the half wave plate is chromatic, there is also a linear polarizer directly after the half-wave plate to filter out any horizontal polarization that could still be present. The orientation of the two components was determined by first inserting the polarizer and minimizing the intensity of the light that came out. That ensured that the polarizer was orthogonal to the polarizing beam splitter. The half-wave plate was then added and rotated until the intensity was maximized. The re-imaged focus was then collimated by a 45-mm focal length achromat onto the SLM. The pupil is then sampled by 274 SLM pixels across its diameter.

The spatial light modulator can be used to create phase patterns for APP coronagraphs (Codona et al., 2006). The APP coronagraphs use phase only pupil functions to apodize the PSF. The apodization creates a dark hole close to the center of the PSF to suppress the diffracted starlight.

One of the largest influences on the performance of coronagraphs are non-common path (NCP) errors. These residual aberrations are not sensed by the wavefront sensor and can therefore not be corrected by the DM. To measure the NCP errors a holographic focal plane wavefront sensor is added to the coronagraphic phase pattern. This coronagraphic modal wavefront sensor(CMWFS) (Wilby & Keller, 2016) creates holographic copies of the PSF that are sensitive to pupil-plane aberrations. For each phase mode
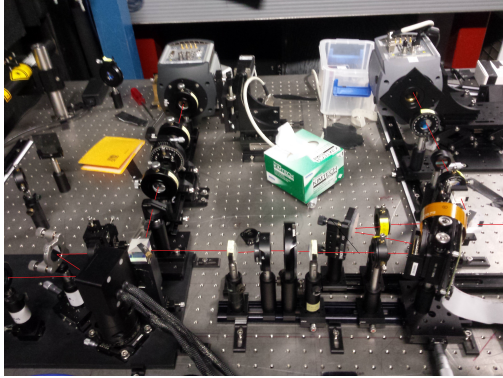
Figure 2.3: In this figure the spatial light modulator configuration together with the high resolution imaging camera are shown. The optical path is indicated with a red line.

two PSF copies are made. The mode coefficient can then be retrieved by measuring the normalized difference between the Strehl ratio of the copies. Because the CMWFS works in the science focal plane, it can correct for any NCP error.

After the SLM the beam was redirected by a fold mirror and then focused by a 125-mm focal length lens. The focused beam goes through a second beam splitter. This 90:10 beam splitter sends 10% to the imaging arm and 90% to the spectrograph. The imaging camera is used to measure the NCP errors with the CMWFS.

To measure the Strehl ratio of each holographic PSF copy correctly, the PSF has to be super Nyquist sampled. A double achromatic lens system magnifies the PSF with a factor of 3.125. With this magnification the sampling is roughly 4 pixels per λ/D. The camera that is used for the CMWFS is an Andor EMCCD with 512 by 512 16 μm pixels. The corresponding field of view is about 4 by 4 arcsec on the sky.

Because of the small field of view, it is difficult to acquire targets. Therefore another imaging camera was added. After the second beam splitter a third beam splitter was placed with a 50:50 splitting ratio. The transmitted part is sent to the high resolution imaging camera. The reflected part is sent to an acquisition camera. Before the acquisition camera is a double lens system consisting of two achromatic lenses with focal lengths of 250 mm and 40 mm, respectively. The acquisition camera has a pixel size of 5.6 μ m and a total array size of 640 by 480 pixels. The field of view of

the acquisition camera is about 36 by 27 arcsec. But due to the limited size of the third beam splitter, the field of view heavily vignetted after 30 arcseconds. This effectively creates a field of view of 30 by 27 arcseconds.

2.2.3   High-resolution spectrograph

The initial design had a separated path for the SLM and imaging arm and for the spectrograph arm. Because of this the high resolution spectrograph was designed to be fed by a beam with an F-number of 11. This is matched to the output of the AO system. But the module with the SLM setup changed the F number of the beam. So a re-imaging optics was inserted between the spectrograph and the SLM output to create a correct input beam. This re-imaging setup was created with two achromats.

The spectrograph is built around a volume phase (VPH) grating from Kaiser Optical Systems with a line density of 3000 lines/mm. The clear aperture of the grating is 130 mm by 100 mm. This VPH was originally designed for the S5T (Snik et al., 2009) and coated with an UV-VIS anti-reflection coating optimized for 450 nm. With the LEXI prototype we are aiming at the R band. Despite the mismatch between the wavelength range of the grating and LEXI, the VPH grating is usable in the R band. And because the VPH can easily achieve a high resolution because of its high line density we operate it in first order.

There are three parameters that determined the design of the spectrograph. The spectral resolving power, the spectral bandwidth and the entrance slit width. The trade off between resolution and spectral bandwidth was driven by trying to have a bandwidth as broad as possible while still being able to resolve spectral lines. The resolution was set to be 75000 after considering the bandwidth. Together with the spectrograph camera size this results in a bandwidth of 10 nm. The camera for the spectrograph is an Andor Zyla 5.5 sCMOS with 2560 times 2100 6.7 μm pixels.

The slit width is a dominant component in the throughput of the instrument. The slit width was chosen to be as large as possible while still reaching the spectral resolution of 75000. This led to a slit width of 36 μm. Since this was not a readily available slit, we used a 30 μm slit. The effective size of the slit on the sky is 0.13 arcsec. This small slit width was enabled by the adaptive optics system in front of the spectrograph.

Because of the required high resolving power and the high line density, the angle of incidence needed to be quite extreme. The angle of incidence for the central wavelength 632.8 nm is 72.3 degrees. These requirements fixed the focal length of the achromatic collimator and camera lenses, which
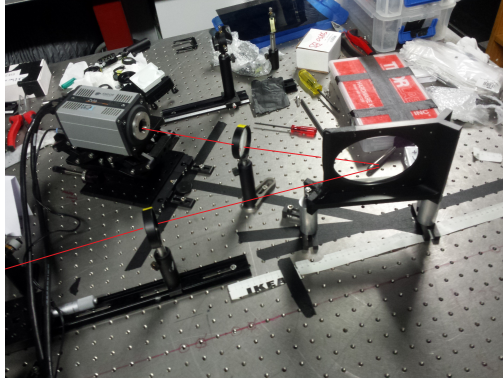
Figure 2.4: The spectrograph as used at the William Herschel Telescope. The red line indicates the optical path. Here the extreme angle of the VPH can be seen.

have focal lengths of 300 mm and 200 mm, respectively.

2.3 First light

During June 2016 the instrument saw first light at the William Herschel Telescope. The figures below show the first results from the observing run. The raw spectra have been flat fielded and bias subtracted. No further data reduction has been done yet. In Figure 2.5 the spectrum of Vega is shown. The spectrum of Vega was taken both with AO and without AO. The difference between these two is clearly visible in the figure. The throughput is higher and the extent of the spectrum in the slit direction is also narrower.

A second target was the binary system Zeta Herculis. The visual magnitude of the components are 2.8 for the primary and 5.4 for the secondary. The spectra of the binary are shown in Figure 2.6. Because of the AO the binary is very well resolved, which can be seen in the spectrum in Figure 2.7. Both spectra show spectral lines at the same position, which should be the case since the spectral types of these two stars are close to each other.
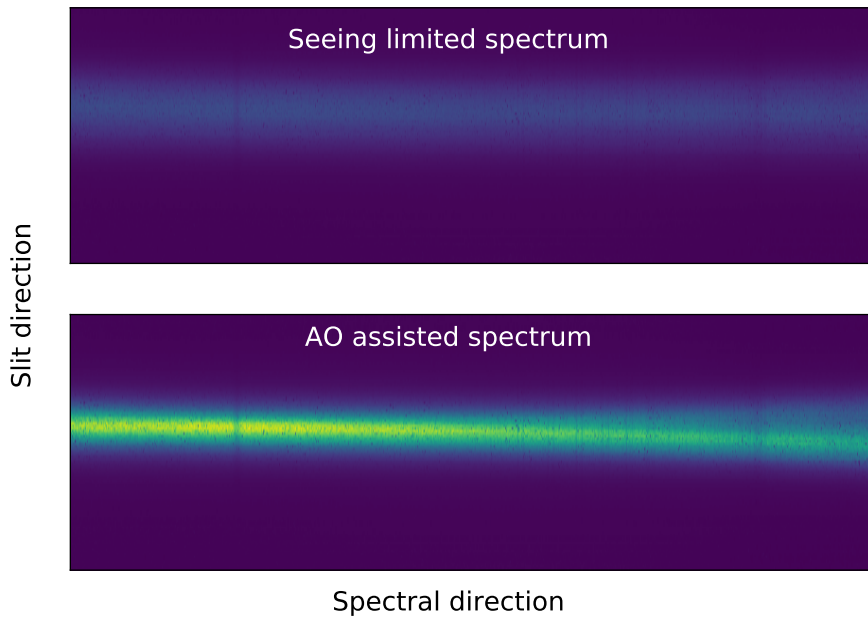
Figure 2.5: Both figures show the spectrum of Vega. The upper spectrum was taken without the AO system, and the bottom spectrum was taken with the AO system. Both spectra were taken with the same integration time. The AO clearly helps with increasing the throughput. Another visible effect is the spread in the spectrum. The spectrum with AO is more concentrated along the slit direction.
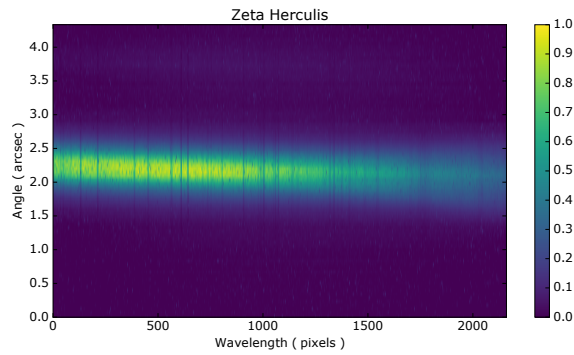
Figure 2.6:   Spectra of Zeta Herculis A and B, a resolved binary with primary magnitude of 2.8 and a secondary magnitude of 5.4. The spectrum of the primary is clearly visible and the spectrum of the secondary is quite faint.
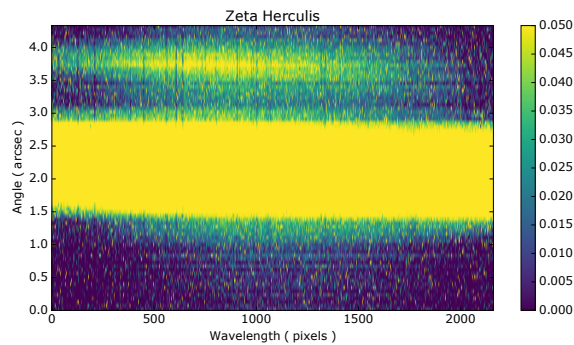
Figure 2.7:   Spectra of Zeta Herculis A and B, a resolved binary with primary magnitude of 2.8 and a secondary magnitude of 5.4. This figure is the same as figure 2.6, but the cut of the image is different to emphasize the spectrum of the secondary.

2.4 Conclusion and outlook

A LEXI prototype has been built and saw first light at the William Herschel telescope in June 2016. The preliminary data reduction indicates that the prototype is reaching its specifications. A more detailed analysis needs to be done to analyse the on-sky performance.

The current version of LEXI is essentially a narrowband instrument. The imaging arm is working with a narrowband filter in the R band, and the spectrograph has a bandwidth of only 10 nm. Several upgrades are planned to improve the instrument.

The first upgrade is to switch to a broadband system. The most important part to replace is the SLM, because it is highly chromatic. The SLM will be replaced by a liquid crystal phase plate that can be used to create broadband phase patterns (Otten et al., 2014; Snik et al., 2012). The second upgrade will increase the spectral bandwidth of the spectrograph by making a cross dispersed Echelle spectrograph. These two upgrades will enable us to cover the whole visible and very near-infrared part of the spectrum. The third upgrade will add an integral field unit.

Bibliography

Brogi, M., Snellen, I. A. G., de Kok, R. J., et al. 2012, Nature, 486, 502

Codona, J. L., Kenworthy, M. A., Hinz, P. M., Angel, J. R. P., & Woolf, N. J. 2006, in Proc. SPIE, Vol. 6269, Society of Photo-Optical Instrumentation Engineers (SPIE) Conference Series, 62691N

Guyon, O. 2005, ApJ, 629, 592

Jovanovic, N., Martinache, F., Guyon, O., et al. 2015, PASP, 127, 890

Macintosh, B., Graham, J. R., Ingraham, P., et al. 2014, Proceedings of the National Academy of Science, 111, 12661

Otten, G. P. P. L., Snik, F., Kenworthy, M. A., Miskiewicz, M. N., & Escuti, M. J. 2014, Optics Express, 22, 30287

Rodenhuis, M., Canovas, H., Jeffers, S. V., et al. 2012, in Proc. SPIE, Vol. 8446, Ground-based and Airborne Instrumentation for Astronomy IV, 84469I

Snellen, I., de Kok, R., Birkby, J. L., et al. 2015, A&A, 576, A59

Snellen, I. A. G., de Kok, R. J., de Mooij, E. J. W., & Albrecht, S. 2010, Nature, 465, 1049

Snik, F., Melich, R., & Keller, C. U. 2009, in Astronomical Society of the Pacific Conference Series, Vol. 405, Solar Polarization 5: In Honor of Jan Stenflo, ed. S. V. Berdyugina, K. N. Nagendra, & R. Ramelli, 383

Snik, F., Otten, G., Kenworthy, M., et al. 2012, in Proc. SPIE, Vol. 8450, Modern Technologies in Space- and Ground-based Telescopes and Instrumentation II, 84500M

Vigan, A., Bonnefoy, M., Ginski, C., et al. 2016, A&A, 587, A55

Wilby, M. J., & Keller, C. U. 2016, in Proc. SPIE, Vol. 9909, Adaptive Optics
    Systems V

3 | On-sky results of the Leiden EXoplanet Instrument(LEXI)

The Leiden EXoplanet Instrument (LEXI) is a bench-mounted high-contrast spectrograph (HCS) and high-contrast imager(HCI). Both science instruments are mounted behind a common adaptive optics (AO) system. The AO can be controlled by several new wavefront sensors for which we will show the first on-sky results. There is a new pupil-plane wavefront sensors; the Generalized Optical Differentiation Wavefront sensor(g-ODWFS). LEXI can switch between two observing modes, the HCI mode or the HD-IFS mode.

The spectrograph is very compact because it is fed by single-mode fiber. The HD-IFS is an IFS that covers the spectral range of 600 – 800 nm with a constant spectral resolving power of 96000. The 2kx3k detector makes it possible to deliver diffraction limited spectra of up to 20 input fibers. The high-dispersion spectra of the HD-IFS allow for robust post-processing technique to remove residual stellar speckles and allows for direct characterization of the faint stellar environment. We will show the first sucesful on-sky results of the injection into a single-mode fiber with LEXI.

In HCI mode an Apodizing Phase Plate (APP) is used to create a dark region around the star with an average design contrast of 1E-4. The APP is multiplexed with holographic modes to create the Coronagraphic Modal Wavefront sensor (cMWS) for non-common path error (NCPE) correction. The cMWS creates holographic copies in the focal plane that react linearly to aberrations. The holographic copies are measured simultaneously with the science target. There is no downtime for NCPE correction. We will show the first on-sky closed-loop correction of (NCPEs) with the cMWS.

3.1   Introduction

The discovery of Proxima Centauri b (Anglada-Escudé et al., 2016) shows that the solar neighbourhood has many planets waiting to be discovered. Current surveys show that most habitable zone planets have a separation near the diffraction limit of current and future large telescopes. Many exoplanets are found through indirect methods such as radial velocity or transit measurements. Both are very successful at finding exoplanets. But the only way to unambiguously characterize the atmospheres of exoplanets is through direct imaging where the photons of the planet are separated from the photons of the star. This is achieved through high-contrast imaging(HCI) where advanced optical techniques are applied to suppress the stellar light at the position of the planet.

For ground-based telescopes the major limitation for exoplanet characterization is the Earth's atmosphere. The atmosphere causes wavefront errors due to turbulence and temperature fluctuations. These wavefront errors limit the spatial-resolution of the telescope. High-speed adaptive optics(AO) is necessary to correct for the wavefront errors. With AO the telescope can reach its diffraction limit again. However not all wavefront errors are corrected. There are residual wavefront errors, which are due to errors in the measurements of the wavefront or due to certain modes that the AO cannot correct. To control the AO system the wavefront errors need to be sensed which is done by a wavefront sensor.

Another limitation is set by the difference in optical path of the science instrument and the AO wavefront sensor. Because there are optics which are not in the common path of both systems there will be wavefront errors that are not sensed by the AO system. These are called NCPAs and are usually of a low-order. These low-order NCPAs are the main limitation for deep starlight suppression by the coronagraph close to the star. Currently there is a lot of research focused on the active control of the NCPAs by using focal-plane wavefront sensing (FPWFS) (Jovanovic et al., 2018).

After AO and NCPA correction it is still possible to have residual speckles in the focal plane. Smart post-processing methods are necessary to discern whether the speckle is a planet or light from the star. Most conventional post-processing methods use spatial diversity to remove the residual speckles of the star. But this leads to problems at small inner working angles where the speckles change by large amounts due to slowly changing NCPAs. A very promising approach that has recently been explored is the combination of high-resolution spectroscopy together with high-contrast

imaging (Snellen et al., 2015). High-contrast imaging spatially separates the planet from the star and overcomes part of the large contrast between the objects. High-resolution spectroscopy(HRS) can be used to gain additional orders of magnitude and suppress the star enough to characterize the exoplanets atmosphere. At high-resolution the spectral lines from the planet and star can be separated. The difference in spectral lines is due to a difference in radial velocity and/or a difference in molecular composition. Using matched spectral filters it becomes possible to remove the residual starlight and discover and characterize exoplanets at the same time.

The Leiden Exoplanet Instrument(LEXI) is a HCI pathfinder instrument that is being developed at Leiden. LEXI is a bench-mounted visiting instrument for the William Herschel Telescope(WHT) at La Palma. LEXI consists of an AO system that feeds two different instruments, a high-contrast imager and a high-contrast spectrograph(HCS). The main purpose of LEXI is to explore the power of HCS for exoplanet detection and characterization. It is the first instrument that is specifically designed for HCS in the visible band. As LEXI is a pathfinder instrument it uses several newly developed techniques for HCI. An overview of the modules of LEXI will be given in section 2. Section 3 will show the improvement of the AO system and the first on-sky results of the newly developed generalised-Optical Differentiation wavefront sensor (Haffert, 2016). In section 4 we will discuss the sensing, calibration and control of NCPAs with the coronagraphic Modal Wavefront Sensor(cMWS) (Wilby & Keller, 2016; Wilby et al., 2017). And section 5 will show the results of the HCS.

3.2   LEXI overview

We observed with LEXI in December 2017 during the observing run LEXI consisted of three modules. A sketch of the system is shown in Figure 3.1. This was the second observing run of LEXI at the WHT (Haffert et al., 2016). During that run we experienced that our AO system was not of high enough order to correct for the full aperture. There were two options for this run either the DM was replaced with a higher order DM or we stop down the aperture. We decided to stop down the aperture as this was an option that was cheaper and was quicker to implement compared to the lead time of a new DM. The geometry of the stopped-down aperture is show in Figure 3.2. The diameter of the off-axis segment was based on the actuator count of our Alpao 97-15 DM. The Alpao 97-15 DM has 11 actuators across the pupil. Because the Alpao DM has actuators on the

Figure 3.1: This is a sketch of the LEXI modules. The light from the WHT is fed into an AO system which feeds two different backends. The science instruments are an high-contrast imager and a high-contrast spectrograph.

edges of the mirror the effective degree of freedom is $N - 1$. To correct for most turbulence we have to match 1 degree of freedom to 1 patch of turbulence. At the WHT there is a median seeing of 1 arcsecond, which corresponds to a r_0 of 10 cm at 550 nm. LEXI has a specctral range from 0.6 um to 0.9 um. To match the median seeing over the whole wavelength range we decied on an off-axis segment of 1.2 meter.

We do not have a derotator in our system and this causes the spiders to come in and out during observations. With a few small simulations we estimated that the effects of the spiders were negligible compared to the residual wavefront errors of the atmosphere. Therefore we decided against implementing a derotator.

LEXI is bench-mounted on an optical table at the Nasmyth focus of the WHT. The light from the Nasmyth focus of the WHT passes through a small optical relay which consisted of two achromatic doublets with a focal length of 100 mm and 25 mm respectively. In the intermediate pupil plane we placed an aperture stop. This relay was designed with the idea to accommodate a potential atmospheric dispersion compensator for a future version of LEXI. After the relay the light is collimated by a 140 mm achromatic doublet. The projected pupil size of the off-axis segment is 13.5 mm which fully illuminates the DM. The DM can run at frequencies up to 900 Hz and has a stroke of 60 um. This allows for corrections of large aberrations. The beam is redirected by a second fold mirror after the DM. The beam is then focused by an identical lens as was used for the collimation. This creates a 1-to-1 system between the AO input and output.

The focused beam passes through a 50-50 cube beam splitter. Half of the light is sent towards the wavefront sensor arm and the other half is sent

William Herschel Telescope
4.2m diameter
LEXI run June 2016

William Herschel Telescope
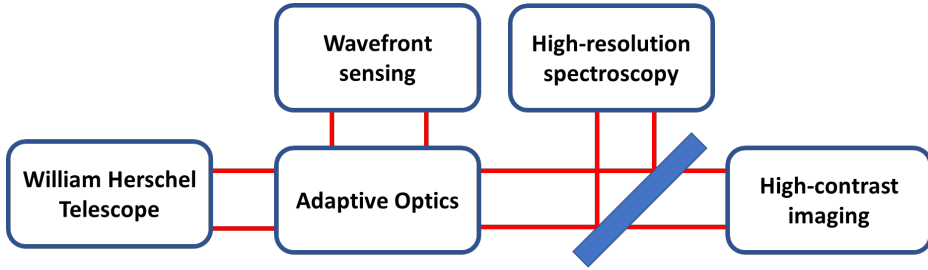1.2m off-axis segment
LEXI run December 2017
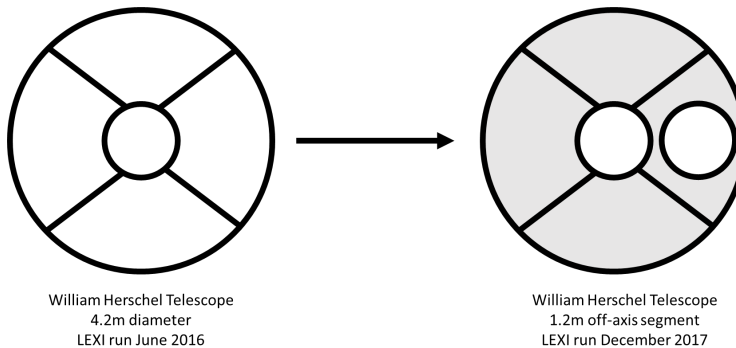
Figure 3.2: This is a sketch of the LEXI modules. The light from the WHT is fed into an AO system which feeds two different backends. The science instruments are an high-contrast imager and a high-contrast spectrograph.

towards the science instruments. Both the wavefront sensor and the science instruments use the same wavelength range and share the photons. For the science beam the light collimated by a 50 mm achromatic doublet. This creates a 4.7mm pupil of which a 4.55mm pupil is cut-out by a liquid-crystal plate. The liquid-crystal plate contains our pupil plane coronagraphs and acts as a pupil stop at the same time. The pupil stop is created by using a very high frequency grating creating a grating mask (Doelman et al., 2017). The imaging is done with a last 2 inch 300 mm lens. This creates a PSF that is sampled with about 3 pixels per λ/D at 700nm.

3.3   The adaptive optics module of LEXI

The wavefront sensor of LEXI has been changed from a Shack-Hartmann wavefront sensor to a generalized Optical Differentiation Wavefront Sensor(g-ODWFS). This is a new wavefront sensor which was recently developed in Leiden (Haffert, 2016). The g-ODWFS uses focal plane amplitude masks to filter the incoming light to sense the wavefront in the pupil plane. A sketch of the g-ODWFS principle is shown in Figure 3.3. The g-ODWFS has several advantages over the SHWFS. The foremost advantages is it's sensitivity which is close to a modulated pyramid wavefront sensor. A second advantage is that the wavefront sensor manipulates the light in the focal plane allowing for arbitrary sampling in the pupil. Because the sampling only depends on the camera we can be adjust the sampling on the fly
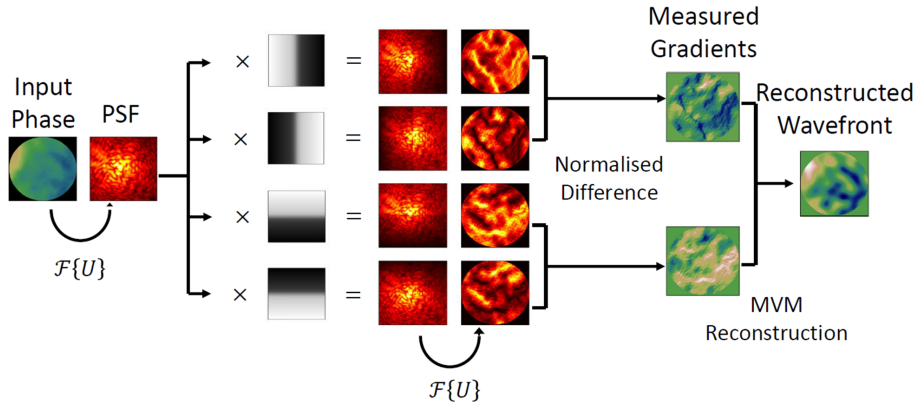
Figure 3.3: This figure is adapted from Haffert 2016 (Haffert, 2016). The input pupil is focused by a lens and filtered by 4 focal plane masks. Each filtered PSF is collimated which results in 4 pupils. The normalized difference of the pupils encodes the wavefront slope. The wavefront is reconstructed with a matrix-vector multiplication.

by binning the camera. We made use of this by oversizing the pupils on purpose and then used the highest binning setting with which we could still operate all DM modes. The camera of the wavefront sensor is an Andor iXon EMCCD with 128x128 pixels which can run at 512 Hz while reading out the full frame. Because we binned the camera we could increase our AO loop speed to 800 Hz, which was limited before by the frame rate of the camera. The pupils were sampled with 16 pixels across which is still oversampled with respect to the actuators.

Normal amplitude filters are not photon efficient, they will always throw away light. Therefore the amplitude filters of LEXI were implemented with patterned liquid-crystals(LC). The LC act as a spatially varying half-wave plate. This plate will rotate linear polarized light by an amount which is determined by the position on the focal plane mask. After the focal plane mask the light is split into two pupils with a Wollaston prism. The angle of the polarization after the LC plate determines the relative transmission between the two outgoing pupils. So we can implement amplitude filters by acting on the angle of polarization. Because the LC plate needs linear polarized light we place a polarization beam-splitter cube up-stream of the LC plate. This has a nice advantage as we can use the two output
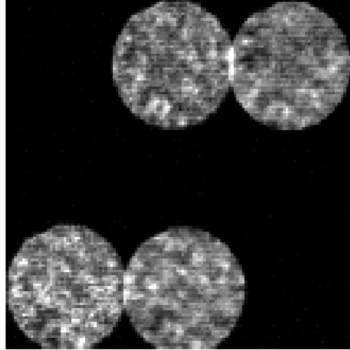
Figure 3.4: The output of the g-ODWFS during on-sky operation. The left and right pair of pupils are modulated with an opposite intensity pattern. This asymmetry is caused by wavefront aberrations. There is still a detector artifact left in the pupil images which is due to a non-perfect estimated bias.

polarizations of the beam-splitter cube for sensing the wavefront gradient in two directions. The final output pupil configuration is shown in Figure 3.4.

The combination of an off-axis segment and the new wavefront sensor led to a great improvement in quality of PSF. The first on-sky results of the g-ODWFS can be seen in Figure 3.5. The wavefront sensor closed the loop on-sky for the first time without any issues. The Full-Width at Half-Maximum(FWHM) changed from 4.3 λ/D in natural seeing to a diffraction-limited FWHM of 1 λ/D. The seeing during the observation is estimated at 0.64" from the FWHM of the seeing-limited PSF. The quality of the AO correction allowed us to use a coronagraph to increase the raw contrast. This can be seen in Figure 3.5 where the AO-corrected PSF is a one-sided vector Apodizing Phase Plate(vAPP) (Otten et al., 2014; Snik et al., 2012) coronagraphic PSF. With the vAPP and the improved AO we were able to reach 5σ contrast of 1E-3 at from $2\lambda/D$ and further. This can be seen in Figure 3.6. The contrast gain is factor of 10 to 200 depending on the distance from the star. This curve was measured from an imaging cube consisted of 250 frames with an individual exposure time of 0.07s. The cube was checked for temporal correlations between individual frames, but no correlation was found. Therefore we determined the 5σ contrast limits by taking the standard deviation of imaging cube in time and divided by the square root of the number of frames. Afterwards the normalization was
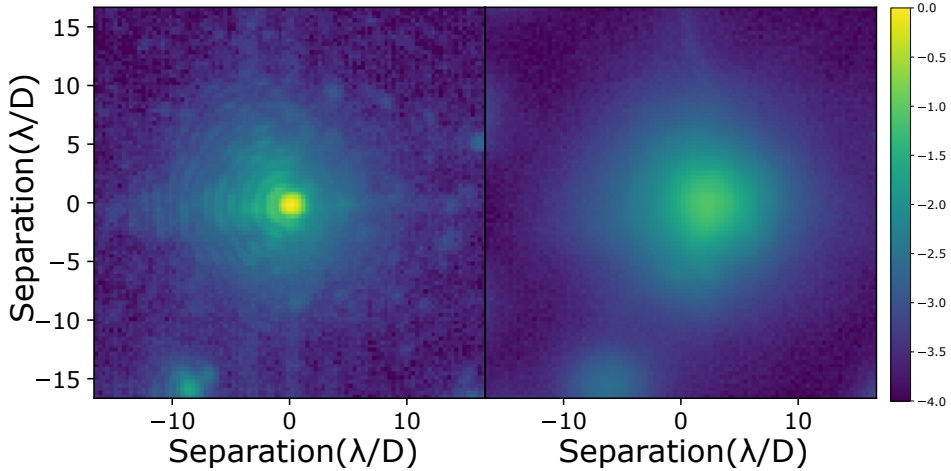
Figure 3.5: The figure on the left shows the closed-loop AO PSF and figure on the right shows the seeing-limited PSF. The AO improves the quality of the PSF substantially. The AO PSF is close to diffraction limit with a FWHM of 1 λ/D.

done by the maximum of the mean-combined image. The results of this observation is encouraging as this contrast is reached with a total exposure time of only 17.5 seconds.

3.4 Focal-plane wavefront sensing with the cMWS

The contrast at small inner-working angles is mainly limited by low-order non-common path errors. The HCI arm of LEXI uses focal plane wavefront sensing to sense and actively correct for NCPAs. The focal-plane wavefront sensor is a coronagraphic Modal Wavefront sensor. The cMWS is a holographic wavefront sensor that can be multiplexed together with a vAPP. The hologram generates spatially separated secondary PSF copies in the science focal plane. For each wavefront aberration two oppositely biased satellite spots are generated. The difference between the Strehl ratio of the two copies reacts linearly to the amplitude of the selected wavefront aberrations. This makes the cMWS a fast and real-time wavefront sensor for focal-plane wavefront sensing.

The design for LEXI is shown in Figure 3.7. The cMWS is multiplexed with a 360 degree dark hole vAPP. The dark hole contrast is 1E-4 from 3 to
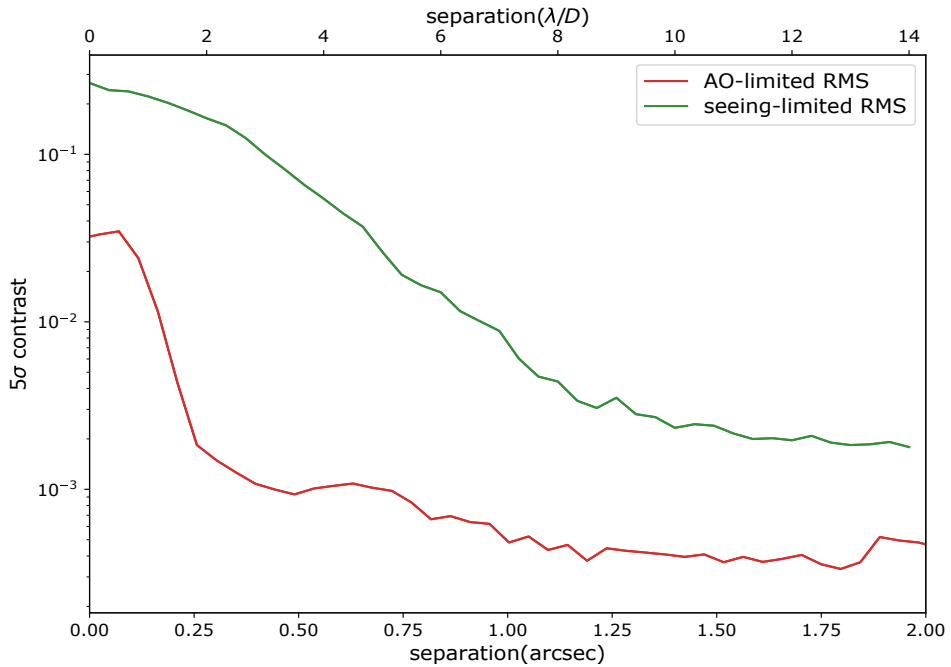
Figure 3.6:   The post-processed 5σ contrast curves of LEXI. These curves were generated from a 17.5 second data cube. The contrast is 1E-3 from 2 λ/D and further. The gain in contrast compared to the seeing-limited PSF is significant. This gain varies from a factor of 10 to 200 depending on the angular separation.
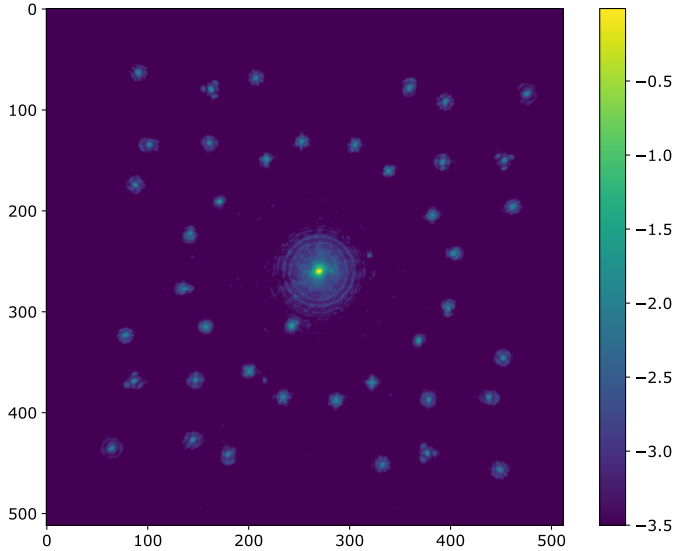
Figure 3.7: The multiplexed focal plane of the cMWS. The cMWS is multiplexed with a 360 degree dark hole vAPP. The vAPP creates a 1E-4 dark hole from 3 to 6 λ/D. The cMWS is multiplexed with 20 Disk Harmonic modes.

6 λ/D. The vAPP is multiplexed together with 20 Disk Harmonic modes. The Disk Harmonics(DH) were chosen over the Zernike modes as the edge behaviour of the DHs is more regular. The there is also a ghost visible on the bottom left of the stellar PSF. The cMWS was calibrated by applying the DH modes iteratively on the DM. From the response of the cMWS to the DM modes we build up an interaction matrix. This takes care of any linear cross-talk between the sensed modes and calculates the gain between the sensor and the DM. The calibration was done with the internal light source during the day. Any NCPA sensed by the cMWS was send to the high-speed g-ODWFS as a reference offset for the slopes.

The closed-loop feedback was successfully tested on Regulus. This can be seen in Figure 3.8. The quality of the PSF increases after the loop on the cMWS has been closed. The first Airy ring became more circular. The outer edges of the diffraction structure was also closed to the designed

structure. The improvement in contrast can be seen in 3.9. The contrast improves by a factor of 1.5-2. This is more evident by looking at the sensed wavefront rms in Figure 3.10. After the loop closes the wavefront rms decreases by a factor of 1.5-2.

3.5   Single-mode fiber-fed spectroscopy

High-contrast spectroscopy is a robust technique for removing speckle noise. It has been used to characterize the atmosphere of giant exoplanets and determine the spin rate of these planets. LEXI will have an fiber-fed IFU spectrograph in the future. The current baseline design is to use a single-mode multi-core fiber for the IFU. But is it notoriously difficult to couple efficiently into a single-mode fiber (Bechter et al., 2016; Jovanovic et al., 2014; Jovanovic et al., 2017). An important experiment is to see whether LEXI is able to inject light into a single-mode fiber-fed spectrograph. The spectrograph of LEXI has been designed to reach a spectral resolving power of 100000 from 600 to 900 nm for 19 fibers. The spectrograph itself is a cross-dispersed echelle spectrograph. Because the input is diffraction-limited due to the single-mode fiber the spectrograph itself is very small in size. A photo of the assembled spectrograph can be seen in Figure 3.11.

To keep the design relatively simple we opted to go for a special kind of single-mode fiber, a photonic crystal fiber(PCF). The PCF we used was a Large Mode Area fiber (LMA). LMA fibers are fibers with a large Mode Field Diameter which can be up many tens of microns. We used the LMA-15 of NKT-photonics which had a MFD of 12.5um. This is ideally suited to the SBIG STF-8300 CCD camera which has a pixel size of 5.4 um. Due to the matching of the sizes no reimaging optics are necessary to change the F-ratio of the beam. To reach the large MFD the NA of the fiber has to be low, and is around 0.05 for our wavelength range. This makes it relatively easy to collimate the beam. For the collimator we decided to use a off the shelf Thorlabs tube lens, the TTL200MP. This infinity-corrected tube lens is an apochromatic design with a diffraction-limited field of view of ±11 mm designed to operate from 400 nm to 2000 nm. After the collimation the beam will be pre-dispersed by a 18 degree BK7 wedge prism of Thorlabs and then dispersed by an Thorlabs R2 echelle grating with 31.6 lines/mm. After the reflection of the echelle grating the beam will through the wedge prism a second time. The collimating tube lens is also used as a camera lens. Because of it's wide field of view and broad wavelength performance, the lens is able to deliver a diffraction-limited cross-dispersed spectrum on
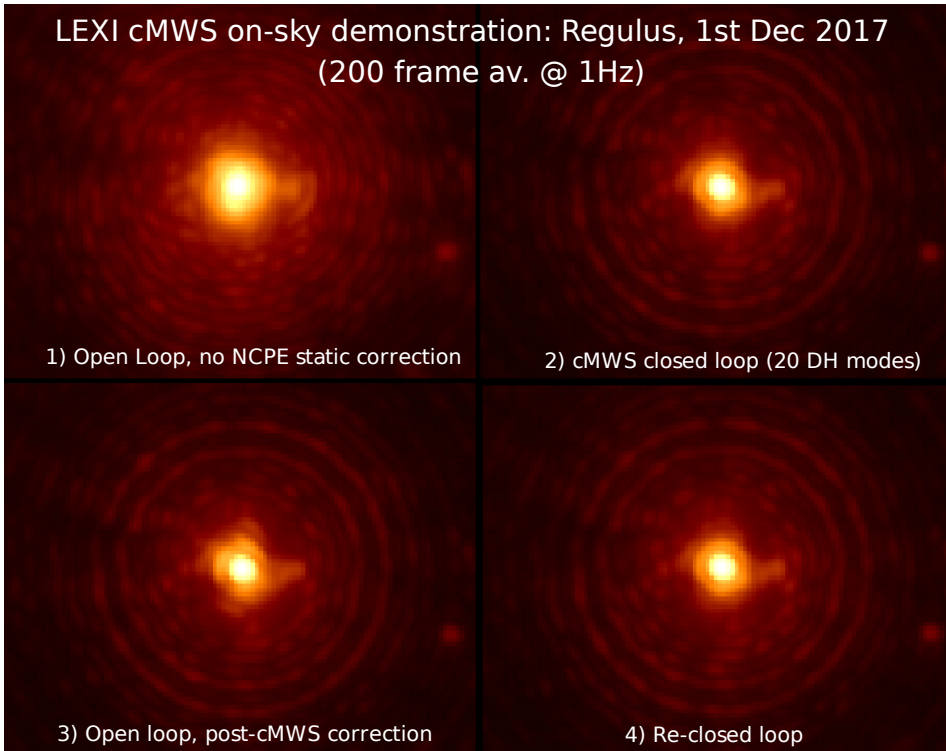
Figure 3.8:   A sequence of stacked images of the PSF during operation of the cMWS. During closed-loop feedback of the cMWS the PSF clearly improves in quality. The asymmetric feature in the first panel has been fixed and the first Airy ring looks nice and round. After the first round of feed-back the loop is opened again and the NCPA's are allowed to evolve again. The last panel shows the closed loop PSF after that.
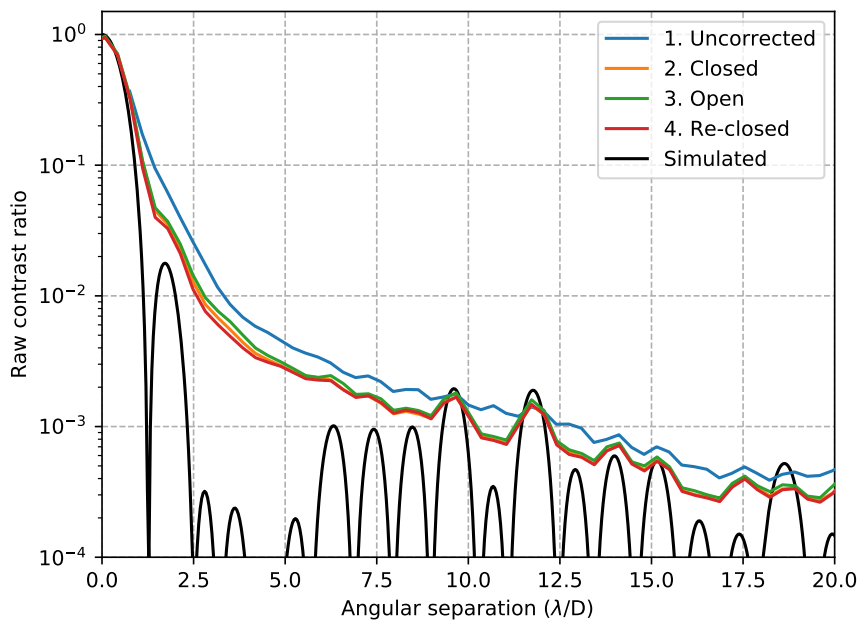
Figure 3.9: The contrast curve of Regulus with the 360 vAPP dark hole. The cMWS does improve the raw contrast by a factor of 1.5-2. We do not however reach the design contrast.
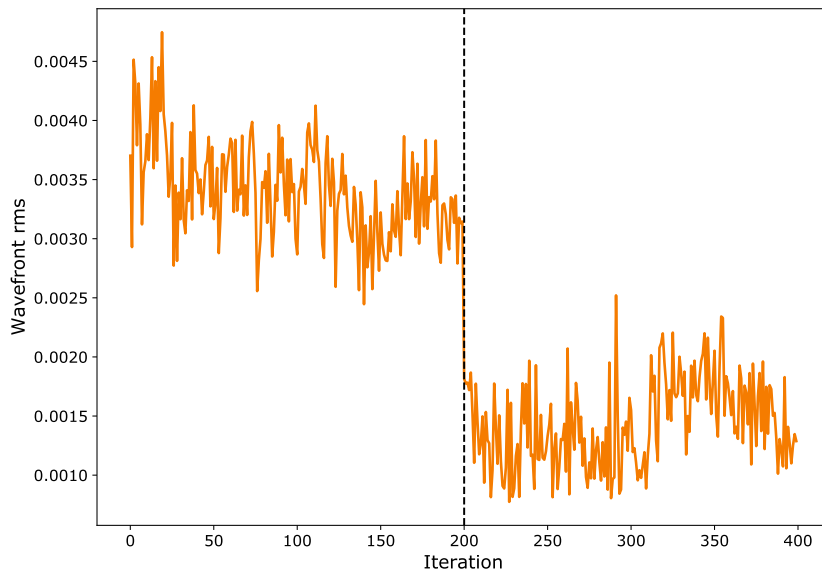
Figure 3.10: The wavefront rms as measured by the cMWS. The wavefront rms gain is not calibrated therefore only the relative change is important. The black dashed line indicates the moment that the cMWS starts to give feedback. The wavefront rms as measured by the cMWS decreases by a factor of 1.5-2 which is exactly the gain in contrast that was achieved.
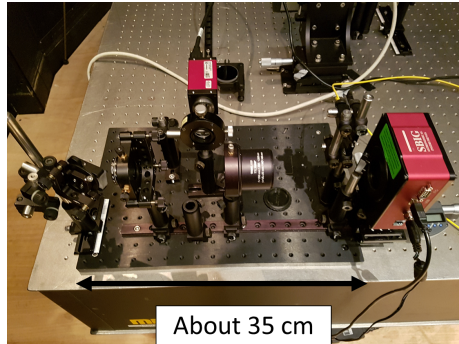
Figure 3.11: A picture of the single-mode fiber-fed spectrograph of LEXI. The spectrograph footprint is about 35 cm by 25 cm. It is a minimal design with 1 fold mirror, 1 collimator/camera lens 1 prism and 1 grating. The spectrograph is fed by a LMA-15 fiber from NKT photonics which is dispersed on a SBIG STF-8300 camera. A fold mirror can be entered to look at the broadband output of the fiber without dispersion.

the detector.

An advantage of the LMA fibers is their constant MFD as function of wavelength. To keep this property the F number changes as the wavelength changes. This exactly cancels out the wavelength dependence of the spectral resolving power of a grating. Therefore the spectral resolving power is almost constant across the whole wavelength range. An example of the spectra that were obtained with the LEXI spectrograph can be seen in Figure 3.12. The oxygen absorption lines from the Earth's atmosphere are very clear in the spectrum. These oxygen lines have also been used to estimate the spectral resolving power of the spectrograph, which was calculated to be 92000 which was very close to the designed resolving power of 96000.

3.6   Conclusion and outlook

The strategy to change the wavefront sensor and stop down the aperture was very successful. The first on-sky results of the g-ODWFS are very encouraging and showed that it worked under natural seeing conditions and with broadband light. The improved Strehl and PSF quality allowed us to apply high-contrast imaging techniques. This lead to the successful closed-loop demonstration of the cMWS. The cMWS has shown to increase
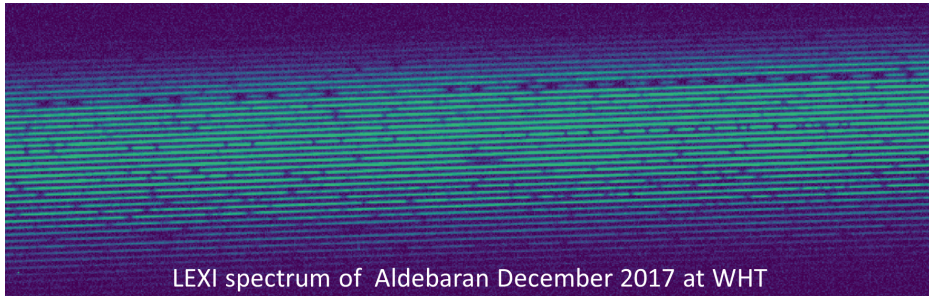
Figure 3.12: This is a cross-dispersed spectrum of Aldebaran. The integration time of this spectrum if 40 minutes with a SNR of 30-40 on the continuum. The spectrum shows very clear and deep spectral lines, which indicate the high-quality and high-resolution of the spectrum.

the contrast by a factor 1.5-2 which is also indicated by the sensor itself as the wavefront rms has also decreased by a factor of 1.5-2. LEXI was also able to inject light efficiently into a single-mode fiber-fed spectrograph. With Aldebaran we measured the design parameters of the spectrograph and confirmed that it reached the requirements.

LEXI is currently being upgraded with a major component being the upgrade of the spectrograph. It will change from a single single-mode fiber-fed spectrograph to a multi-core fiber-fed spectrograph. It will allow up to 20 fibers at a spectral resolving power of 100000 between 600-900nm. An important aspect during this upgrade is the addition of an ADC. The ADC becomes necessary as we want to couple the high-resolution spectrograph with more advanced coronagraphic techniques which need well corrected tip/tilt otherwise there will be stellar light leaking through.

Bibliography

Anglada-Escudé, G., Amado, P. J., Barnes, J., et al. 2016, Nature, 536, 437

Bechter, A., Crass, J., Ketterer, R., et al. 2016, in Proc. SPIE, Vol. 9909, Adaptive Optics Systems V, 99092X

Doelman, D. S., Snik, F., Warriner, N. Z., & Escuti, M. J. 2017, in Proc. SPIE, Vol. 10400, Techniques and Instrumentation for Detection of Exoplanets VIII, $10400 - 10400 - 12$

Haffert, S., Wilby, M., Keller, C., & Snellen, I. 2016, in Ground-based and Airborne

Instrumentation for Astronomy VI, Vol. 9908, International Society for Optics and Photonics, 990867

Haffert, S. Y. 2016, Optics Express, 24, 18986

Jovanovic, N., Guyon, O., Martinache, F., Schwab, C., & Cvetojevic, N. 2014, in Proc. SPIE, 91477P–91477P

Jovanovic, N., Schwab, C., Guyon, O., et al. 2017, A&A, 604, A122

Jovanovic, N., et al. 2018, in Proc. SPIE, Vol. 10703, Adaptive Optics Systems VI

Otten, G. P. P. L., Snik, F., Kenworthy, M. A., Miskiewicz, M. N., & Escuti, M. J. 2014, Optics Express, 22, 30287

Snellen, I., de Kok, R., Birkby, J. L., et al. 2015, A&A, 576, A59

Snik, F., Otten, G., Kenworthy, M., et al. 2012, in

Wilby, M. J., & Keller, C. U. 2016, in Proc. SPIE, Vol. 9909, Adaptive Optics Systems V

Wilby, M. J., Keller, C. U., Snik, F., Korkiakoski, V., & Pietrow, A. G. M. 2017, A&A, 597, A112

4 | The Single-mode Complex Amplitude Refinement (SCAR) coronagraph

I. Concept, theory, and design

Adapted from
E. H. Por and S. Y. Haffert
Astronomy and Astrophysics in press (2019)

Context The recent discovery of an Earth-mass exoplanet around the nearby star Proxima Centauri provides a prime target for the search for life on planets outside our solar system. Atmospheric characterization of these planets has been proposed by blocking the starlight with a stellar coronagraph and using a high-resolution spectrograph to search for reflected starlight off the planet.

Aims Due to the large flux ratio and small angular separation between Proxima b and its host star ($\leq 10^{-7}$ and $\leq 12.2\lambda/D$ respectively; at 750nm for an 8m-class telescope) the coronagraph requires high starlight suppression at extremely-low inner working angles. Additionally, it must operate over a broad spectral bandwidth and under residual telescope vibrations. This allows for efficient use of spectroscopic post-processing techniques. We aim to find the global optimum of an integrated coronagraphic integral-field spectrograph.

Method We present the Single-mode Complex Amplitude Refinement (SCAR) coronagraph that uses a microlens-fed single-mode fiber array in the focal plane downstream from a pupil-plane phase plate. The mode-filtering property of the single-mode fibers allows for the nulling of starlight on the fibers. The phase pattern in the pupil plane is specifically designed to take advantage of this mode-filtering capability. Second-order nulling on the fibers expands the spectral bandwidth and decreases the tip-tilt sensitivity of the coronagraph.

Results The SCAR coronagraph has a low inner working angle ($\sim 1\lambda/D$) at a contrast of $< 3 \times 10^{-5}$ for the six fibers surrounding the star using a sufficiently-good adaptive optics system. It can operate over broad spectral bandwidths ($\sim 20\%$) and delivers high throughput ($> 50\%$ including fiber injection losses). Additionally, it is robust against tip-tilt errors ($\sim 0.1\lambda/D$ rms). We present SCAR designs for both an unobstructed and a VLT-like pupil.

Conclusions The SCAR coronagraph is a promising candidate for exoplanet detection and characterization around nearby stars using current

high-resolution imaging instruments.

4.1   Introduction

The discovery of many rocky exoplanets around stars (Borucki et al., 2011) has prompted the radial velocity search of the closest and brightest ones. This led to the discovery of a terrestrial exoplanet in the habitable zone around Proxima Centauri (Anglada-Escudé et al., 2016). This planet does not transit its host star (Kipping et al., 2017), making transit spectroscopy impossible. Proxima b however has an angular separation in quadrature of $\sim 2.2\lambda/D$ at 750nm for an 8m-class telescope, making a spatially resolved imaging approach feasible. Lovis et al. (2017) explores the possibility of coupling the high-contrast imager SPHERE (Beuzit et al., 2008) with the high-resolution spectrograph ESPRESSO (Pepe et al., 2010). The implementation of the coronagraph was left as an open question. Here we show a new type of coronagraph that will enable a combination of SPHERE and a high-resolution spectrograph to successfully observe Proxima b.

  With the advent of extreme adaptive optics systems (xAO), such as SPHERE (Beuzit et al., 2008), GPI (Macintosh et al., 2014) and SCExAO (Jovanovic et al., 2015), direct detection has taken some major steps forward. These systems create a diffraction-limited point spread function (PSF), which allows for the use of coronagraphy to enhance the contrast of observations. Coronagraphs need to suppress stellar light at the location of the planet, while having high throughput for the planet itself. Additionally, they need to operate over a broad wavelength range and in the presence of residual telescope aberrations, both static and dynamic. Telescope vibrations in particular turned out to be a major concern for these high contrast imaging instruments (Fusco et al., 2016). The performance of pupil-plane-only coronagraphs is independent of telescope pointing, making telescope vibrations less of a concern. An inherent disadvantage of pupil-plane coronagraphs is that the coronagraphic throughput loss is the same for the star and the planet. Therefore designs of pupil-plane coronagraphs that reach high contrasts or extremely-low inner working angles have an intrinsically low throughput. As a result, coronagraphs combining focal-plane and pupil-plane optics often outperform pupil-plane-only coronagraphs at extremely-low inner working angles (Mawet et al., 2012). For example, an apodizing phase plate (APP) with an annular dark zone optimized from $1.2\lambda/D$ to $2.3\lambda/D$ for a contrast of 10^{-4} has a Strehl ratio (ie. planetary throughput) of 0.13%. The APP optimization was performed following Por

(2017).

Even with the best adaptive optics systems, residual aberrations will always limit the raw contrast of ground-based observations to $\sim 10^{-6}$ to 10^{-7} (Guyon, 2005). Currently however, observations are limited by the non-common-path errors between the wavefront sensor and science camera, creating quasi-static speckles in the focal-plane. These speckles amplify atmospheric residuals (Aime & Soummer, 2004) and are notoriously hard to predict. The raw contrast in the intensity image provided by the coronagraphic system is often enhanced by post-processing techniques to form the final contrast curve of the observation. Diversity of some kind is often used to calibrate the instrument itself. Angular diversity (Marois et al., 2006) uses the rotation of the sky with respect to the instrument and has provided excellent results. A recent development in this field uses the diversity in radial velocities of the star and the planet: stellar-light speckles still retain the radial velocity of the star, while the planet appears at a different velocity altogether. Cross-correlation techniques on high-resolution spectroscopy (Konopacky et al., 2013; Riaud & Schneider, 2007; Sparks & Ford, 2002) combined with coronagraphy (Kawahara et al., 2014; Snellen et al., 2015; Wang et al., 2017) show great promise. They provide dayside spectroscopy of τ Boötis b (Brogi et al., 2012) and even the first measurement of planetary spin (Snellen et al., 2014).

Integration of both coronagraphy and high-resolution spectroscopy into a single concept has only recently been attempted. Mawet et al. (2017) use a fiber injection unit in the focal-plane downstream from a conventional vortex coronagraph. A single-mode fiber was centered around the planet and the stellar light speckles were removed using active speckle control algorithms. While this setup does allow for transportation of the light to a dedicated high-resolution spectrograph, it does not optimally combine both methods. A system for which all components are optimized simultaneously is always better than, or at least as good as, a system for which each component is optimized separately. In this paper we allow the coronagraph design to depend on the single-mode fibers in the focal plane. This allows for more freedom in the design process and provides better planetary coronagraphic throughput as those modes filtered out by the fiber injection unit do not need to be suppressed by the upstream coronagraph. The increase in throughput can be quite significant. For example, optimizing a SCAR coronagraph with an operating angular separations from $1\lambda/D$ to $2.5\lambda/D$ yields a throughput of $\sim 54\%$, compared to the $\sim 0.13\%$ of the corresponding APP mentioned above.
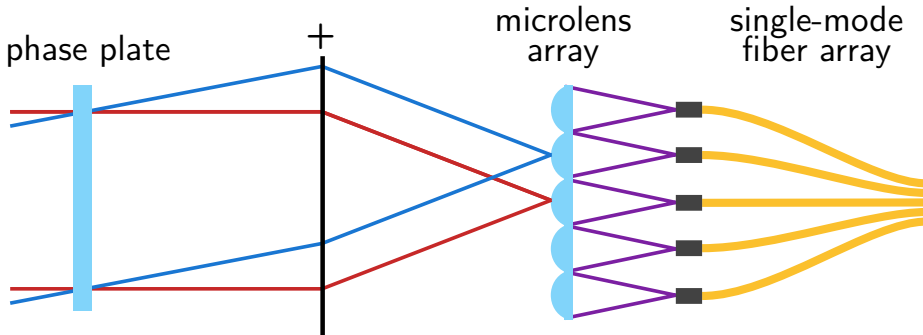
Figure 4.1: Schematic layout of the proposed system. The phase plate located in the pupil-plane alters the PSF that is imaged on the microlens array. Each microlens focus is imaged on a single-mode fiber. An off-axis source will be spatially separated in the focal-plane and its Airy core will fall on a different microlens.

The schematic layout of the proposed coronagraph is shown in Figure 4.1. The SCAR coronagraph uses a phase plate in the pupil plane to alter the PSF. The light is then focused on the microlens array which focuses the light into the single-mode fiber array. This provides additional filtering of the incoming starlight. The starlight is nulled on off-axis fibers, while light is let through in the center fiber. This means that the light from an off-axis companion, of which the PSF is the same as that of the star, will be let through by the off-axis fiber on which it is centered. In this paper, we aim to provide an overview of the principle and optimization behind the SCAR coronagraph.

Interestingly, the use of single-mode fibers for coronagraphy is not new. Haguenauer & Serabyn (2006) already propose using a single-mode fiber to null the star by using a π phase shift on part of the pupil. Martin et al. (2008) develop this further and Hanot et al. (2011) finally put this system on sky. These applications of single-mode fibers for coronagraphy were based on interferometry. Mawet et al. (2017) is the first to put single-mode fibers behind a conventional coronagraph.

In Sect. 4.2 we describe nulling on single-mode fibers, extend the fiber injection unit to use multiple single-mode fibers and show the coronagraphic capabilities and throughput of such a system. In Sect. 4.3 we use an apodizing phase plate coronagraph to expand the spectral bandwidth and decrease the tip-tilt sensitivity. In Sect. 4.4 we describe the throughput, inner work-

ing angle, chromaticity and sensitivity to aberrations of this new system. We conclude with Sect. 4.6.

4.2   Modal filtering using single-mode fibers

4.2.1   Nulling in single-mode fibers

The coupling efficiency η_{sm} of light into a single-mode fiber can be calculated by the projection of the input electric field E_{in} onto the mode of the fiber E_{sm} as

$$\eta_{\mathrm{sm}} = \frac{\left| \int E_{\mathrm{in}}^{*} E_{\mathrm{sm}} \mathrm{d}A \right|^2}{\int |E_{\mathrm{in}}|^2 \mathrm{d}A \ \int |E_{\mathrm{sm}}|^2 \mathrm{d}A}, \tag{4.1}$$

where the integration is done over all space. The fiber mode E_{m} can be calculated using waveguide theory and the geometry of the fiber in question, but in this paper we use the Gaussian approximation (Marcuse, 1978)

$$E_{\mathrm{sm}}(r) = \exp\left[-\frac{r^2}{w^2} \right] \tag{4.2}$$

where r is the distance from the center, and $2w$ is the mode field diameter of the fiber. We see that the coupling efficiency $\eta_{\mathrm{sm}} \leq 1$ for all input fields and that maximum coupling is only attained when E_{in} matches the fiber mode.

Suppose now that we put a single-mode fiber in the focal plane of a telescope, with its mode field diameter matched to that of the Airy core of the PSF. Using Equation 4.1 we can calculate the coupling efficiency $\eta_s(\mathbf{x})$ of the star as a function of focal-plane position x. We can do the same thing for the planet, yielding $\eta_p(\mathbf{x}, \mathbf{x}_0)$ where $\mathbf{x}_0$ is the location of the planet. The raw contrast at the fiber output can be written as

$$C_{\mathrm{raw}}(\mathbf{x}, \mathbf{x}_0) = \frac{\eta_{\mathrm{s}}(\mathbf{x})}{\eta_{\mathrm{p}}(\mathbf{x}, \mathbf{x}_0)}. \tag{4.3}$$

When the fiber is centered around the planet, ie. $\mathbf{x} = \mathbf{x}_0$, the electric field of the planet will couple efficiently into the fiber, as the Airy core is closely matched to the Gaussian fiber mode. The electric field of the star at this position will however consist of Airy rings. These will be smaller, not only in intensity but also spatially so that around two Airy rings will be visible on the fiber face. This is possible as the Airy core itself has a size of $\sim 1\lambda/D$ full-width half-maximum (FWHM), while the Airy rings are sized

$\sim 0.5\lambda/D$ FWHM. As neighboring Airy rings have opposite phase, the light from the two Airy rings will (partially) cancel each other in the projection integral of Eq. 4.1, resulting in a lower stellar throughput. This nulling provides an additional contrast enhancement not possible with multimode fibers. Fig. 4.2 illustrates this graphically in columns one and two.

Column three in Fig. 4.2 shows an alternative null structure. This second-order null balances the contribution of the core with its two side-bands. This has the effect of broadening the null for decenter as the loss in overlap with one of the sidebands is compensated by the increase in overlap with the other. In this case we have essentially split the second-order null into two first-order null by subtracting a tiny fraction of the matched mode. This gives a characteristic double dip in the coupling curve and broadens the null even more by raising the coupling between the two first-order nulls. This coupling at the center must be kept below the design coupling.

This second-order null is the basis for the SCAR coronagraph. For comparison with existing coronagraph implementations, we define the "relative integration time" as the ratio between the integration time for unresolved imaging and coronagraphic imaging to reach a predefined signal-to-noise ratio. This can be expressed in the star and planet throughput as

$$\frac{\Delta T_{\text{coronagraphic}}}{\Delta T_{\text{unresolved}}} = \frac{\eta_s(\mathbf{x})}{\eta_p^2(\mathbf{x}, \mathbf{x}_0)}. \tag{4.4}$$

This metric takes into account both the raw contrast and planet throughput of the coronagraph. Noise sources other than photon noise were ignored in this respect. As these only become important for small planet throughputs, we will show both the relative integration time η_s/η_p^2 and the planet throughput η_p.

4.2.2 Single-mode fiber arrays using microlenses

To cover the field of view around a star, we need to fill the focal plane with single-mode fibers. This means that the fibers are impractically close together. A more reasonable solution is to use a microlens array with a single-mode fiber in each focus, as shown by Corbett (2009). Each fiber face now contains a strongly spatially-filtered telescope pupil. The corresponding focal-plane mode for each fiber can be recovered by back-propagating the fiber mode to the focal plane. An example of such a mode is shown in Fig. 4.3. The amplitude of this back-propagated mode is still Gaussian in amplitude. In phase however, it is flat within the central lenslet, but picks up a phase gradient on off-axis lenslets: light hitting off-axis lenslets
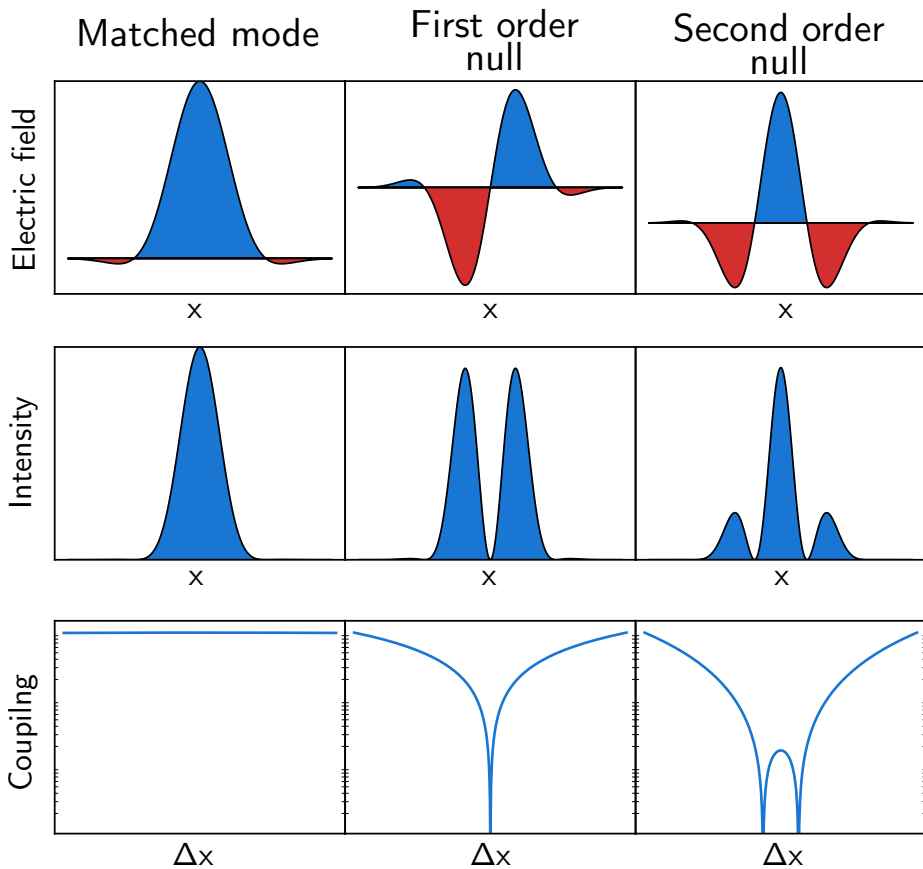
Figure 4.2: Coupling into a single-mode fiber with a (a) matched electric field, (b) first order null and (c) second order null. The first row shows the electric field projected onto the fiber. The second row shows the intensity on the fiber face. The third row shows the coupling efficiency for off-center fibers. The matched mode couples well into the fiber, even for small off-center positions. The first-order null has no throughput: its odd electric field ensures a zero overlap integral in Eq. 4.1. Off-center positions however still transmit because the odd structure is lost. The second-order employs an even electric field where the contribution of the central peak is canceled by the two sidebands. This creates a much broader null when decentering the fiber.
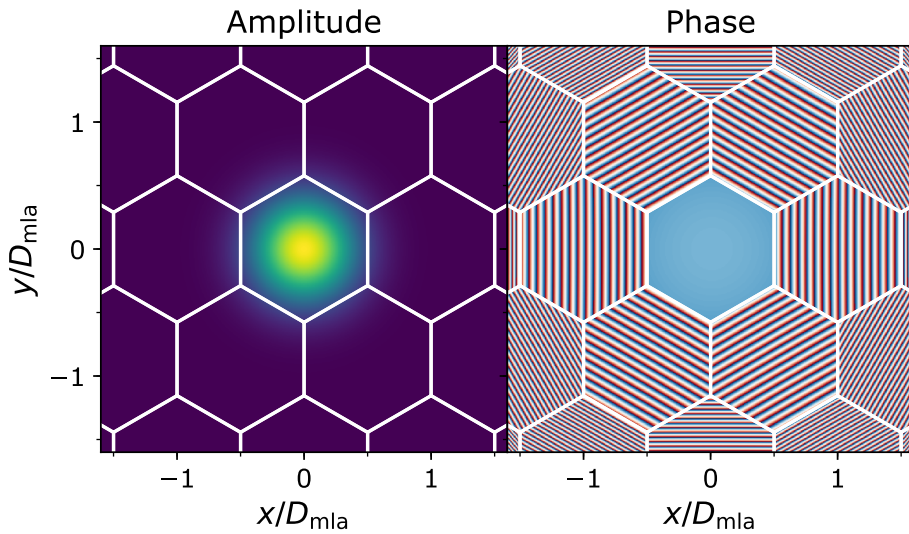
Figure 4.3: Backpropagated mode of a single-mode fiber to the microlens array surface. Conceptually our microlens array and single-mode fiber can still be thought of as focal-plane electric field filtering using this modified mode. The mode is still Gaussian on the central microlens, but picks up an additional tilt on off-axis microlenses: on those microlenses the light needs to have a huge tilt to be propagated into the central fiber.
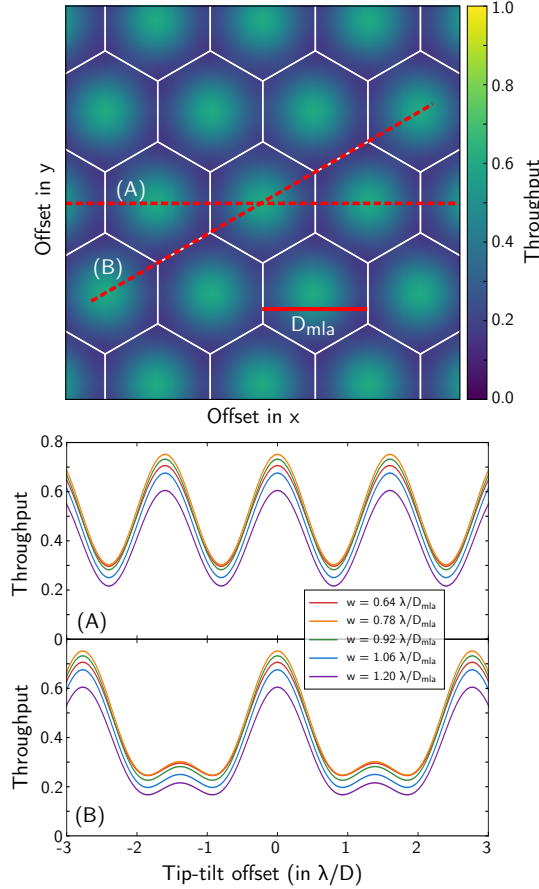
Figure 4.4: Throughput of the single-mode fibers as a function of tip-tilt offset of the source. On the top a two-dimensional throughput map is shown. On the bottom two slices through this map are plotted for several values for the mode field diameter of the single-mode fibers. Maximum throughput of $\sim 72\%$ is reached at the center of a lenslet. On the edge of two microlens the throughput of two fibers have to be added to reach $\sim 30\%$ throughput. The worst case is the triple-point at which the maximum throughput drops to $\sim 25\%$. A fiber mode field radius of $w = 0.78\lambda/D$ achieves the highest throughput for all tip-tilt offsets.

need to have a huge tilt to still couple into the central fiber. We denote this off-axis contribution as lenslet crosstalk, and it is taken into account in every optimization and calculation done in this paper.

The throughput of the single-mode fiber array depends on the position of the object and the mode field diameter of the fibers. Figure 4.4 shows the throughput for a clear aperture with slices through the best and worst-case position angles. The throughput is dominated by the lenslet closest to the center of the PSF and is only weakly dependent on the mode field diameter around the optimal value. Additionally, at each position in the focal plane, the optimal value of the mode field diameter is the same, simplifying implementation.

Figure 4.5 shows the throughput of an off-axis lenslet as a function of microlens diameter, while keeping the PSF centered around the on-axis lenslet. We can clearly see that at a diameter of $\sim 1.28\lambda/D$ no stellar light is transmitted by the fiber. This contrast is solely the result of the mode-filtering property of the single-mode fiber: if we were to use multimode fibers instead, the contrast would still be $\sim 3 \times 10^{-2}$ at this point. The nulling can be classified as first order: only where the electric field of the Airy core and the first Airy ring exactly cancel do we see the contrast reduction. Moving the PSF only slightly already destroys this nulling.

Since the PSF changes in size with wavelength, the throughput of an off-axis fiber is inherently chromatic. We can read off the spectral bandwidth from Fig. 4.5 directly. A contrast of 10^{-4} is reached for $1.26\lambda/D < D_{\mathrm{mla}} < 1.30\lambda/D$, corresponding to a spectral bandwidth of just 3%. Nevertheless this demonstrates that significant gains can be obtained by using single-mode fibers instead of multimode fibers or even conventional intensity detectors.

4.3   Coronagraphy with a single-mode fiber array

4.3.1   Conventional coronagraphy

We can use conventional coronagraphy techniques to reduce the spot intensity and ignore the mode-filtering property in the design process. As an example we use the apodizing phase plate (APP) coronagraph (Codona et al., 2006; Otten et al., 2017; Snik et al., 2012). This coronagraph consists of a single phase-only optic in the pupil plane, making it impervious to tip-tilt vibrations of the telescope or adaptive optics system. The phase pattern is designed to yield a dark zone in a certain region of interest in
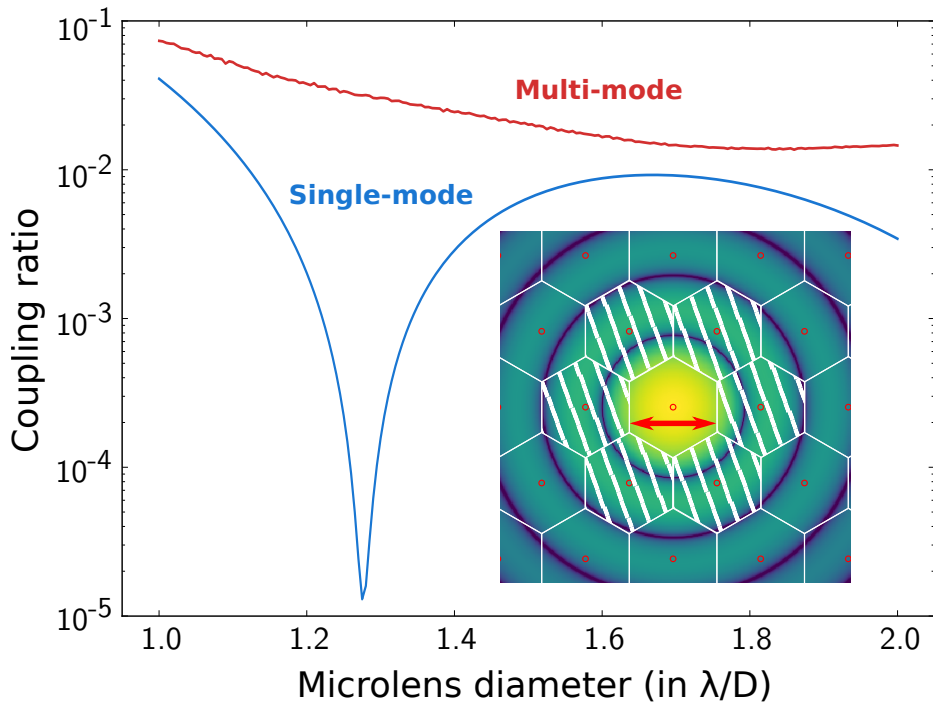
Figure 4.5: Coupling ratio between an on-axis and off-axis source through an off-axis microlens as a function of microlens diameter for a multimode and single-mode fiber. The gain in contrast by using a single-mode fiber can readily be seen in the ratio of these two functions. For most microlens diameters this gain amounts to several orders of magnitude and reaches infinity at $\sim 1.28\lambda/D$ where the light is perfectly nulled on the fiber face by the single-mode fiber. This nulling is first order and is therefore very sensitive to wavelength and centering of the star around the central lenslet.
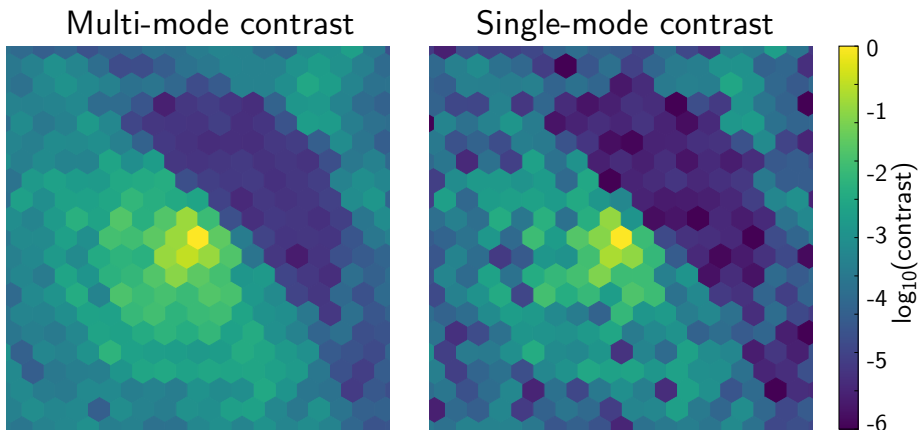
Figure 4.6: Coupling through a microlens array using a conventional APP coronagraph with multimode fibers (left) and single-mode fibers (right). Using a conventional coronagraph such as an APP contrast is still enhanced by the single-mode fibers. The contrast in the dark zone is still enhanced by $\sim 3\times$ on average when using single-mode fibers compared to multimode fibers.

the focal plane. This region of interest can be both one- and two-sided, and can have arbitrary shapes. Most often the one-sided regions of interest are D-shaped and the two-sided are annular. See Por (2017) for a recent description of APP design. As both the PSF of the star and the planet are altered, the Strehl ratio is maximized to retain planet transmission.

Figure 4.6 shows the contrast through a fiber-fed single-mode fiber array using an APP designed for a contrast of 10^{-5} in a D-shaped region with an inner working angle of $2\lambda/D$ and outer working angle of $10\lambda/D$. While the use of single-mode fibers does enhance the contrast by $\sim 3\times$ on average, this enhancement is not consistent: in some fibers the contrast is enhanced by $> 10\times$ while in others we barely see any improvement at all. This shows that the factor of 3 enhancement that Mawet et al. (2017) finds for a dynamic random speckle field holds true for a single-mode fiber in a static structured speckle field, such as a residual coronagraphic electric field, even when the mode shape is modified from a Gaussian to a constricted Gaussian profile.

4.3.2   Direct pupil-plane phase mask optimization

This improvement brings up the question: can we make use of this mode-filtering in the coronagraph design? As the single-mode fiber array already filters out some electric field modes, the coronagraph does not have to suppress those modes; only modes that are transmitted by the single-mode fiber array need to be suppressed by the coronagraph. The coronagraph needs to minimize the coupling through the single-mode fibers, not the intensity at those positions in the focal plane. Designing a coronagraph specifically for the fiber array therefore allows for more design freedom compared to conventional coronagraph design. In principle, any coronagraph can be designed to take the fiber coupling into account. As a case study, we use a pupil-plane phase plate to alter the PSF in the focal plane. A schematic layout of the proposed system is shown in Fig. 4.1.

To find the phase pattern, we use the novel optimizer from Por (2017), based on the work by Carlotti et al. (2013), that maximizes the throughput (ie. Strehl ratio) for a complex pupil mask, while constraining the stellar intensity in the dark zone to be below the desired contrast. Since the transformation between the pupil and focal plane is linear in electric field, this optimization problem is linear, and its global optimum can be easily found using large-scale numerical optimizers such as Gurobi (Gurobi Optimization, 2016). In practice the optimization produces phase-only solutions, which is surprising as non-phase-only solutions are still feasible solutions. As the phase-only optimization problem is simply a more constrained version of the linear one, the phase-only solution must therefore be a global optimum of both problems.

The fiber coupling integral in Eq.4.1, or rather the amplitude of the coupled electric field

$$E_{\text{coupled}} = \frac{\int E_{\text{in}}^* E_{\text{sm}} \mathrm{d}A}{\left| \int E_{\text{sm}} \mathrm{d}A \right|} \tag{4.5}$$

is still linear in the input electric field E_{in}, so we can apply the same method here. We maximize the throughput of the central fiber, while constraining the coupling through the specified off-axis fibers. To counter the chromaticity mentioned in Sect. 4.2.2, we constrain the off-axis stellar intensity at several wavelengths simultaneously, which ensures that the contrast is attained over a broad spectral bandwidth. Jitter resistance is kept in check in a similar manner: the desired raw contrast must be attained for several tip-tilt positions simultaneously.

In Fig. 4.7 we show a few examples of optimizations for one, three and six fibers for a contrast of 1×10^{-4}, 3×10^{-5} and 1×10^{-5} using a
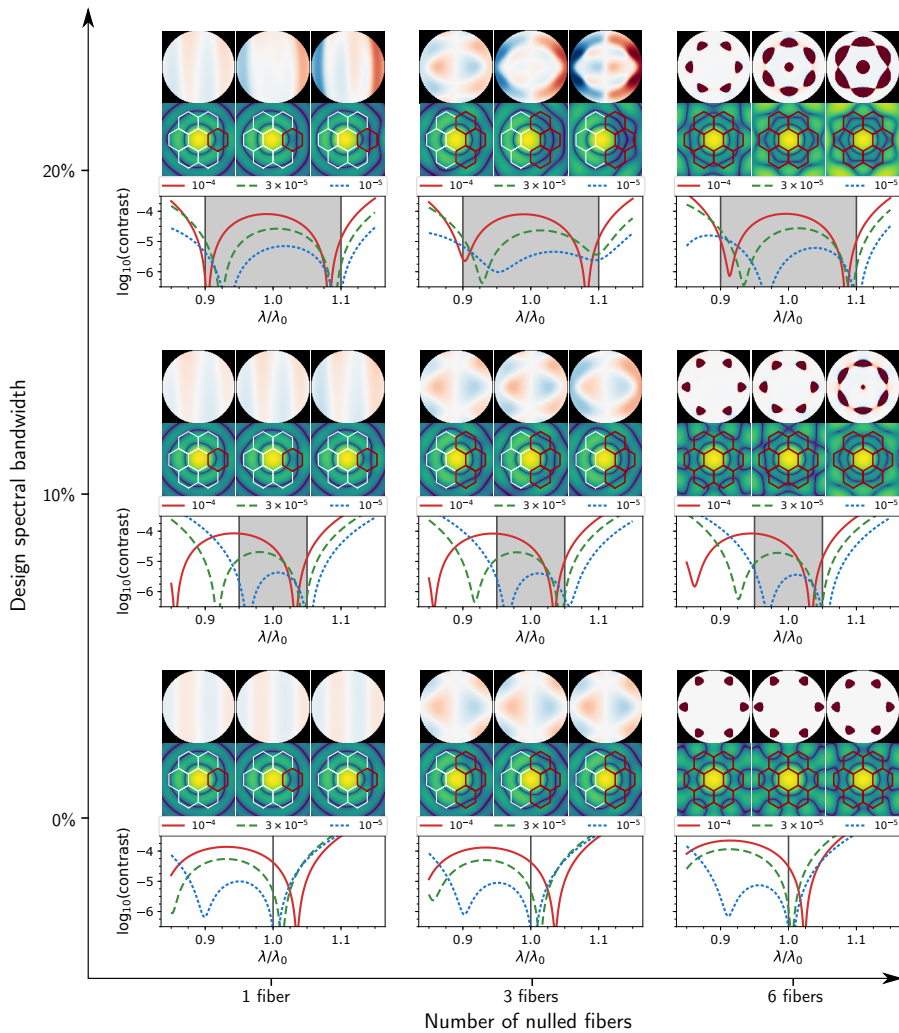
Figure 4.7: A series of optimizations for one, three and six fibers on the first ring of microlenses for a clear aperture. The design spectral bandwidth were 0%, 10% and 20% and the contrasts 1×10^{-4}, 3×10^{-5} and 1×10^{-5}. A $0.06\lambda/D$ peak-to-peak telescope tip-tilt jitter was also taken into account. Each microlens has a circum-diameter of $1.8\lambda/D$. For each SCAR design we show the pupil-plane phase pattern, its corresponding point spread function and its raw contrast η_s/η_p as a function of wavelength averaged over the marked fibers. The chromatic response shows the raw contrast after the single-mode fiber. The second-order nulling on the fiber face is clearly visible in every design. In Table 4.1 we list the fixed and varied parameter in this figure. The throughput of all SCAR designs shown in this figure can be found in Figure 4.9.

Figure 4.8: The same as Fig. 4.7 for a VLT aperture. The aperture was subject to a 1% binary erosion, ie. undersizing the pupil and oversizing central obscuration, spiders and other pupil features by 1% of the aperture size, to accommodate a pupil misalignment. The general structure of the solutions is similar to the case of a clear aperture. The central obscuration increases the strength of the first Airy ring, thereby decreasing the throughput of these SCAR designs slightly. The relatively thin spiders have no influence on the throughput at these angular separations. In Table 4.1 we list the fixed and varied parameter in this figure. A summary of the throughput of all SCAR designs shown in this figure can be found in Fig. 4.9.
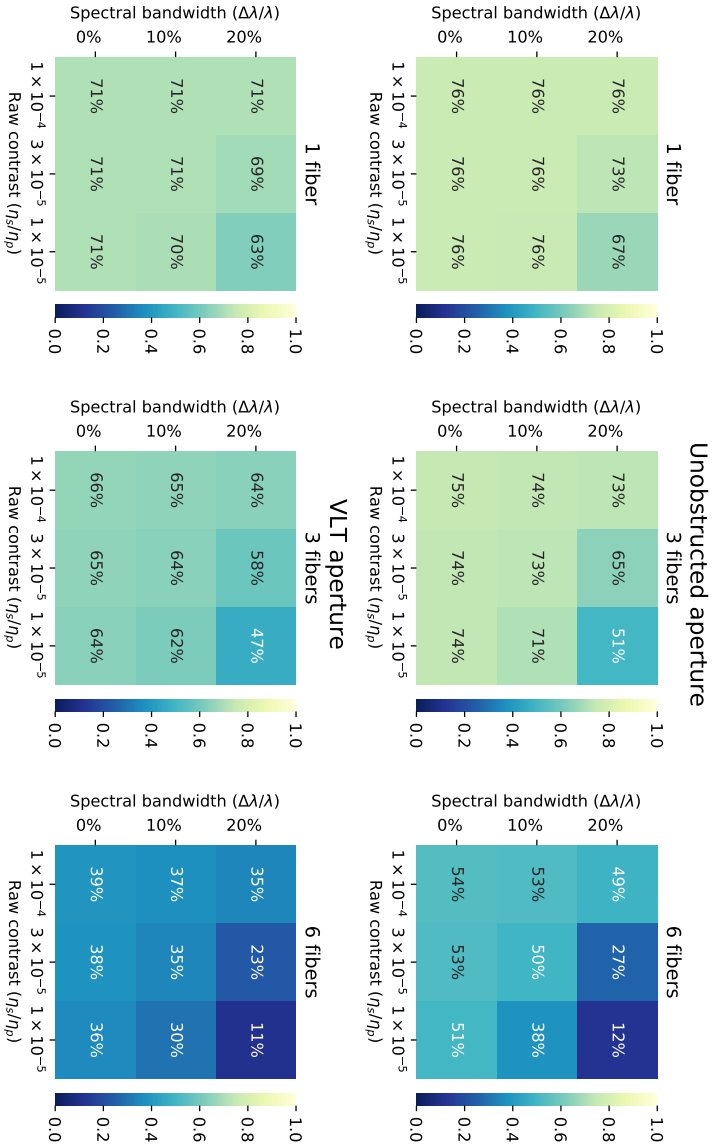
Figure 4.9: The throughput (η_p) for the SCAR designs shown Figs. 4.7 and 4.8. The shown throughput is the total throughput of the coronagraphic system. It includes the Strehl reduction of the phase plate, the spatial filtering of the microlenses and the mode filtering of the single-mode fibers. This throughput is achieved through a single single-mode fiber when the planet is located directly on top of an off-axis lenslet. The throughput at other positions varies generally according to Figure 4.4, but varies slightly depending on the specific SCAR design.

Table 4.1: The design parameters used for all SCAR designs throughout this work. All SCAR designs generated with these parameters can be found in Figures 4.7 and 4.8.

Parameter name	Value
Raw contrast limit	$\{1 \times 10^{-4}, 3 \times 10^{-5}, 1 \times 10^{-5}\}$
Spectral bandwidths	$\{0\%, 10\%, 20\%\}$
Tip-tilt errors	$0.06\lambda/D$ peak-to-peak
Microlens circum-diameter	$1.8\lambda/D$
Microlens shape	Hexagonal
Fiber mode shape	Gaussian
Fiber mode field diameter	$1.7\lambda/D_{\mathrm{mla}}$
Pupil mask	$\{\mathrm{unobstructed}, \mathrm{VLT}\}$

$0\%, 10\%$ and 20% spectral bandwidth, along with their corresponding PSF and chromatic response. The design parameters are shown in Table 4.1. These design parameters were chosen to show a variety of SCAR designs for realistic implementations. At the shown contrast limits, the residual atmospheric speckles will limited the on-sky contrast, even after an extreme AO system. The spectral bandwidths were chosen as wide as possible, without compromising on planet throughput. The resulting spectral bandwidths are large enough to apply spectral cross-correlation techniques.

In each case the optimizer prefers a second order null. This second order null is much more stable against bandwidth and tip-tilt jitter. The reason for this is explained graphically in Fig. 4.2. Furthermore, this second order null is even present in monochromatic optimizations and in optimizations without accommodation for tip-tilt errors. This means that the second-order null requires less phase stroke to achieve and therefore provides higher Strehl ratios.

As the optimizer can handle arbitrary apertures, optimizations for other aperture shapes are also possible. Figure 4.8 shows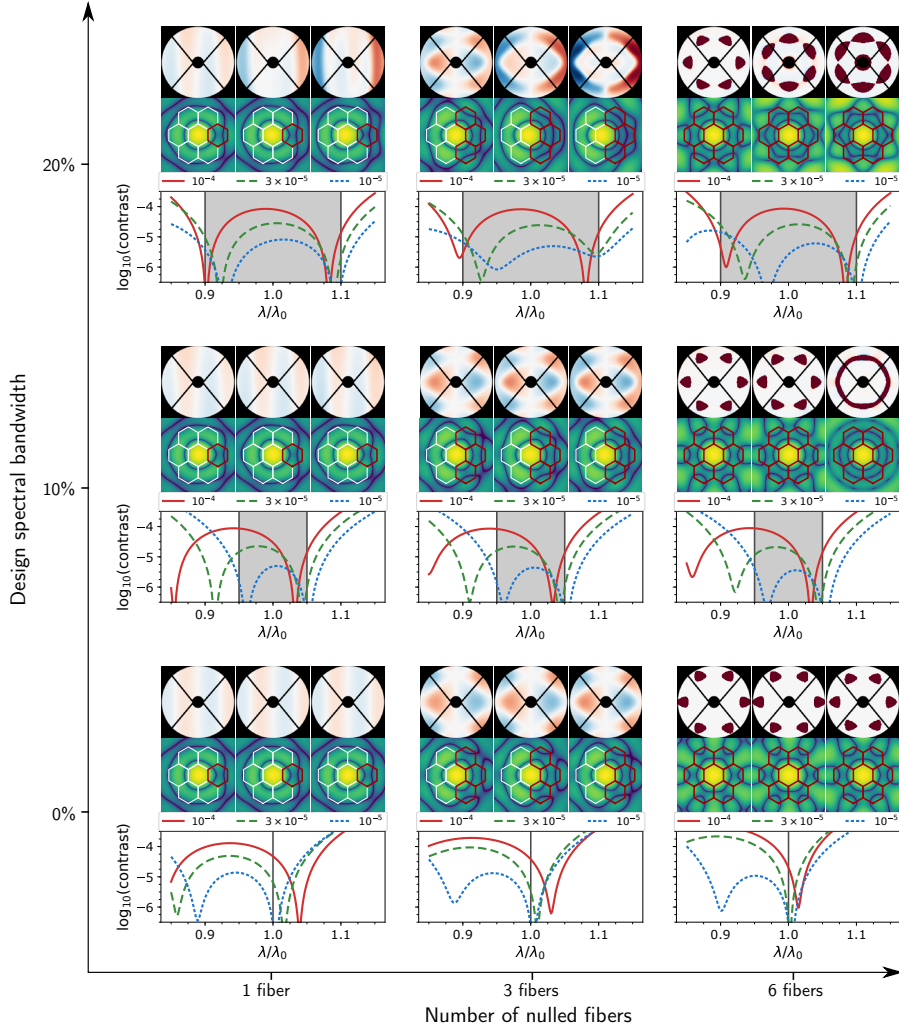 optimizations for a VLT aperture for the same parameters as for the clear apertures. The aperture was subject to a 1% binary erosion, ie. undersizing the pupil and oversizing central obscuration, spiders and other pupil features by 1% of the aperture size, to accommodate for a misalignment in the pupil mask. Although the overall structure is quite similar, there is one key difference compared to a clear aperture: the relative transmission T is lower for all phase plate designs. This means that the relative transmission depends strongly on the size of the central obscuration. This is obvious as larger central obscu-

Table 4.2: The different throughput terms that are important for the SCAR coronagraph. A distinction is made between theoretical and experimental terms. Experimental throughput terms will be non-existent with perfect manufacturing, while theoretical throughput terms are unavoidable. Typical values in the visible are shown for each term. The values for the experimental throughput terms are indicative of current technology performance and may increase as technology matures.

Throughput term	Typical values
Theoretical	
Geometric lenslet throughput	$\sim 80\%$
Fiber injection losses	$90\% - 95\%$
Planet location	$50\% - 100\%$
Phase plate Strehl reduction	$60\% - 80\%$
Total	$\sim 41\%$
Experimental	
Phase plate transmission	$> 85\%$
Fresnel losses on the fiber	$\sim 90\%$
Microlens transmission	$> 95\%$
Strehl ratio of the AO system	$\sim 50\%$
Total	36%
Total	14%

rations strengthen the first Airy ring and brighter features typically cost more stroke, and therefore relative transmission, to change, similar to conventional APP design. Effectively, this means that each feature in the phase pattern becomes larger to compensate for larger central obscurations.

We summarize the multitude of SCAR phase pattern designs in Figure 4.9. This figure shows the total planet throughput η_p, provided that the planet is located in the center of the off-axis microlens. This throughput includes all theoretically unavoidable terms, but excludes all experimental terms. A summary of important throughput terms are listed in Table 4.2.

In the rest of this paper, we consider the outlined SCAR design in Fig. 4.7 and 4.8 using a 10% spectral bandwidth for a contrast of 3×10^{-5}. Although optimized for only 10%, this specific design performs exceptionally well and a contrast of $< 10^{-4}$ is obtained for a spectral bandwidth of 18% centered around the design wavelength.

4.4   Single-mode fiber coronagraph properties

In this section we show the properties of this new coronagraph and perform parameter studies on the fixed parameters in Table 4.1. We discuss the mode field diameter of the single-mode fiber in Sect. 4.4.1, throughput and inner working angle in Sect. 4.4.2, the chromatic response in Sect. 4.4.3, the tip-tilt sensitivity of the SCAR designs in Sect. 4.4.4 and the sensitivity of other modes in Sect. 4.4.5.

4.4.1   Fiber mode field diameter

The phase plate reduces the throughput of planet light. This reduction will also affect the optimal value of the mode field diameter. Smaller mode field diameters result in larger back-propagated fiber modes in the focal plane, which makes it easier to squeeze the three rings necessary for the second-order nulling into this mode. Therefore, we expect higher Strehl ratios (the throughput relative to the unaltered PSF throughput) as the mode field diameter becomes smaller. This is superimposed on the actual throughput of the unaltered PSF. Both curves are shown in Fig. 4.10 for both a clear and the VLT aperture.

4.4.2   Throughput and inner working angle

The throughput shown here is the fractional transmission of light from the entire pupil into the central single-mode fiber: it includes all theoretical terms as listed in Table 4.1. It however excludes all experimental terms. It is clear that larger microlenses generally give a better throughput, as is expected. Additionally, we can see that the optimal mode field diameter as a function of microlens diameter for the unaltered PSF moves to larger mode field diameters, as it is essentially matching the Airy-core width rather than the size of the microlens itself. The optimal mode field diameter for the SCAR however stay the same as smaller mode field diameter have an advantage in their Strehl ratio.

Figure 4.11 shows the throughput (η_p) of the coronagraph for different values for the microlens diameter. The mode field radius of the fiber was fixed at $w = 0.85\lambda/D_{\mathrm{mla}}$ and the contrast at 3×10^{-5}. We adopted a $0.1\lambda/D$ rms telescope tip-tilt jitter with a normal distribution, corresponding to a 2 mas rms tip-tilt jitter at a wavelength of $\lambda = 750$nm. This level of tip-tilt jitter was chosen to mimic a SPHERE-like adaptive optics system, according to Fusco et al. (2016). The throughput is averaged over all pointing
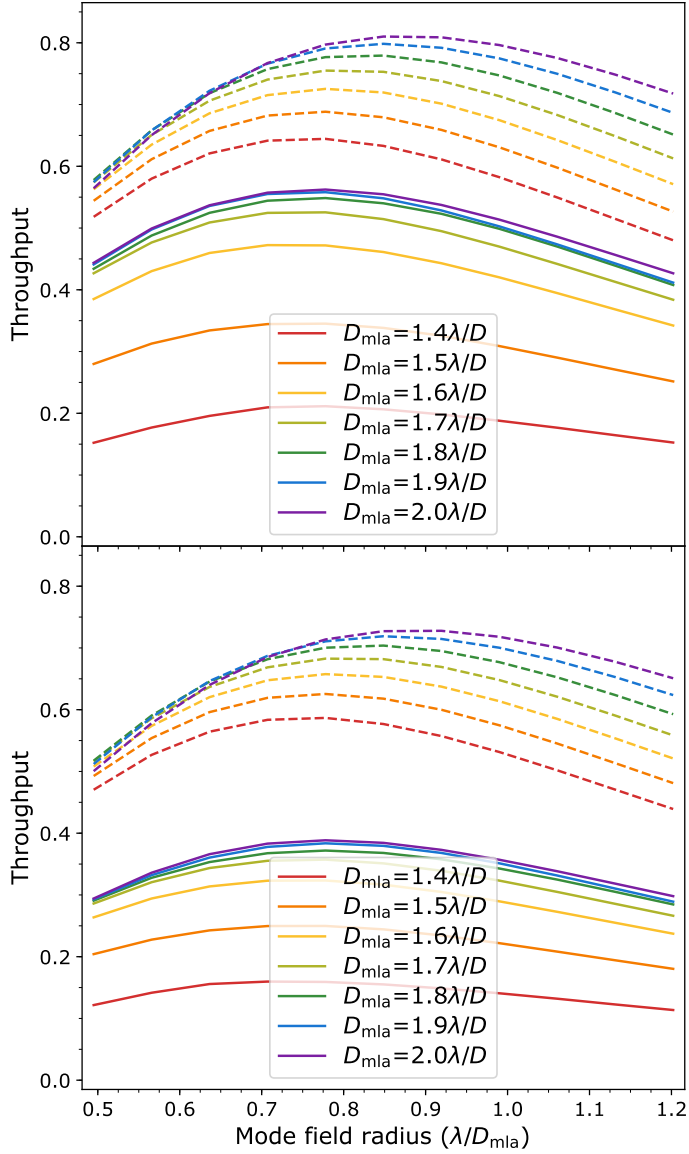
Figure 4.10: Throughput of the central lenslet as a function of mode field radius for various values of the microlens diameter. Each data point represents a different SCAR design. Solid lines indicate the SCAR PSFs, dashed lines an unaltered PSF. The top panel shows the throughput for an clear aperture, the bottom panel for a VLT aperture.

positions and over the full 10% spectral bandwidth. The throughput of off-center fibers is negligible to that of the central fiber: all throughput is concentrated in only one single-mode fiber.

As the stellar throughput is only minimized for the first ring of microlenses, we do not have much throughput beyond the edge of the first off-axis microlens. Designs can be made for more than one ring of microlenses, although this complicates the design procedure and will be discussed in future work. Extremely close to the star, we have no throughput, as the Airy core is still mostly on the central lenslet. At $\sim 0.5\lambda/D$ the throughput starts to rise, reaching a maximum at the center of the first microlens. A throughput of $\sim 50\%$ of the maximum SCAR throughput is already reached at $\sim 1\lambda/D$, which is the usual definition of inner working angle. Also, up to microlens diameters of $\sim 1.8\lambda/D$ the throughput at small angular separations ($< 1\lambda/D$) does not change much, but the maximum throughput still increases. For larger microlens diameter we still gain in throughput at the center of the microlens, however the throughput at these small angular separations starts to suffer, which is especially visible in the $D_{\mathrm{mla}} = 2.0\lambda/D$ throughput curve.

Lines for the theoretical throughput of other coronagraphs are overplotted in Fig. 4.11. Perfect coronagraphs refer to the notion introduced by Cavarroc et al. (2006) and Guyon et al. (2006). A second-order perfect coronagraph removes a constant term from the pupil-plane electric field. A fourth-order additionally removes the x and y components from the electric field. A sixth-order perfect coronagraph furthermore removes the x^2, xy and y^2 modes from the electric field. For the theoretical coronagraphs, the throughput is calculated using a circular aperture of $0.7\lambda/D$ centered around the off-axis planet. We can see that the SCAR throughput lags behind the theoretical second-order coronagraph, but stays close to the fourth-order and beats the sixth-order at angular separations $< 1.7\lambda/D$.

Figure 4.12 shows the relative integration time (η_s/η_p^2) under the same conditions as in Fig. 4.11. We now see that, even though the throughput of the theoretical second-order coronagraph is good, its integration time is minor because it does not outweigh the loss in starlight suppression. SCAR however performs similar to theoretical fourth-order coronagraph for angular separations $< 1.8\lambda/D$. A sixth-order coronagraphs does even better, but suffers from a lack of throughput which becomes noticeable in cases where the raw contrast (η_s/η_p) is limited, which is the case in any ground-based telescope. This suggests that SCAR is a close-to-optimal coronagraph.
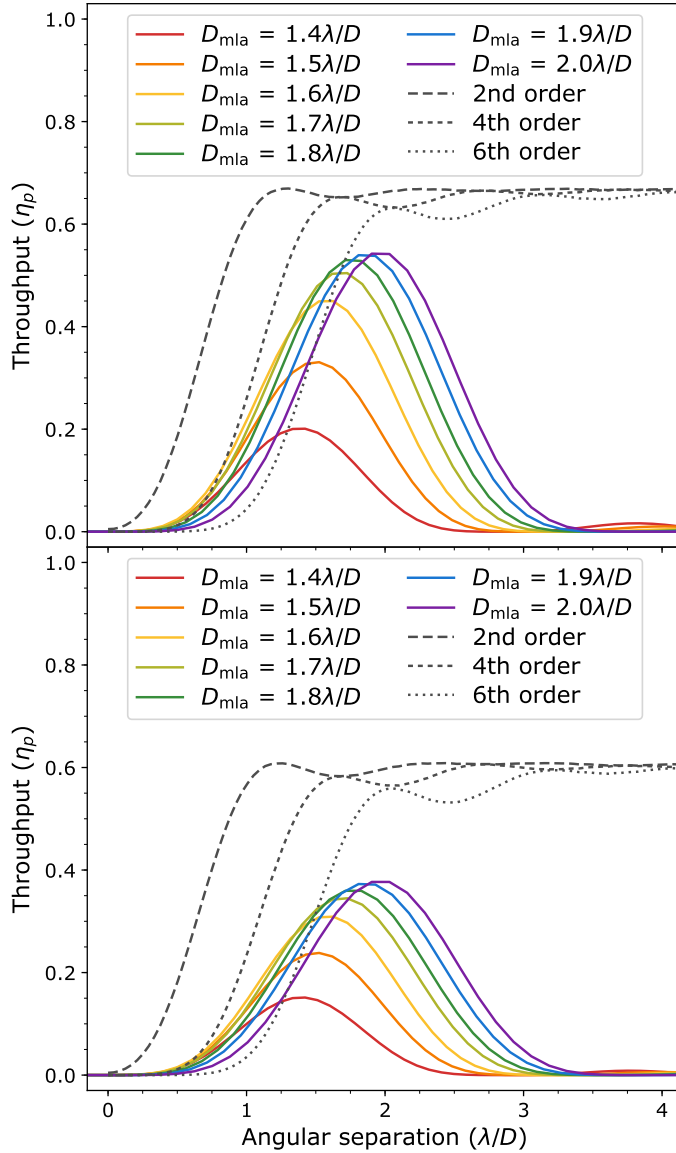
Figure 4.11: Throughput as function of off-axis angle for various values of the microlens diameter. The throughput of a perfect second, fourth and sixth-order coronagraph is also plotted. The top panel shows the throughput for an unobstructed aperture, the bottom panel for the VLT aperture. The throughput is calculated for the optimal position angle of the off-axis source (ie. directly across an off-axis microlens). The throughput for the theoretical coronagraphs is taken to be the fractional flux within an aperture of radius $0.7\lambda/D$ centered around the planet.
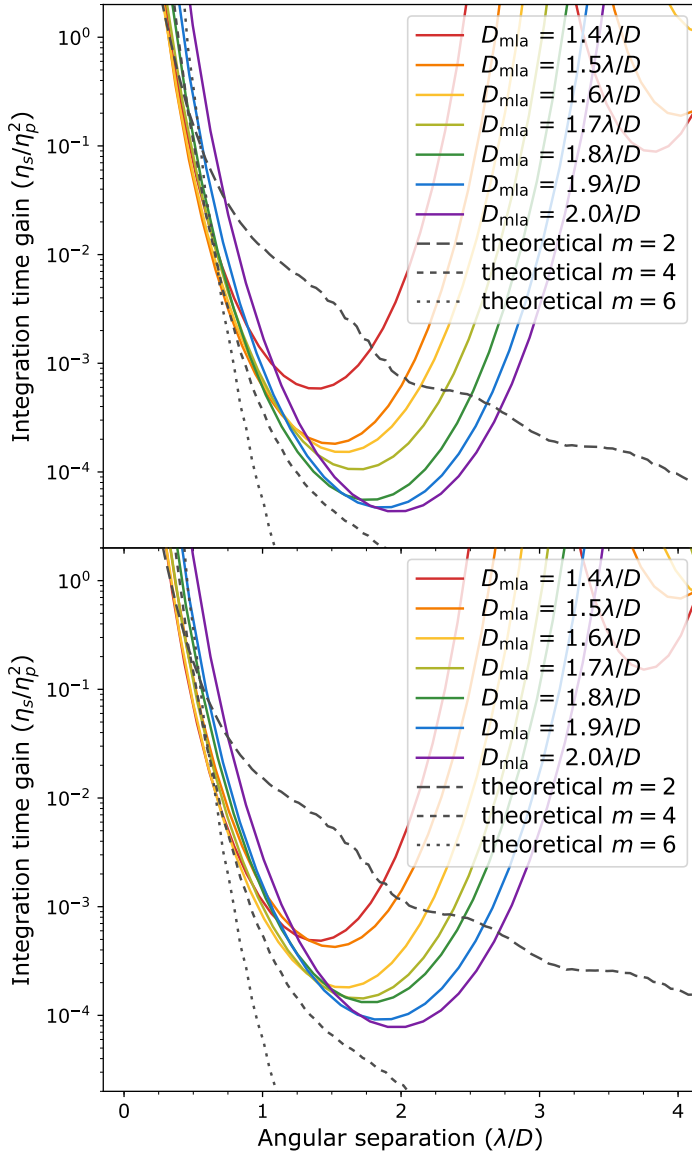
Figure 4.12: Relative integration time (η_s/η_p^2) as function of off-axis angle for various values of the microlens diameter. The top panel shows the relative integration time for an unobstructed aperture, the bottom panel for the VLT aperture. The integration time for the theoretical coronagraphs is calculated on the flux within an aperture of radius $0.7\lambda/D$ centered around the planet.
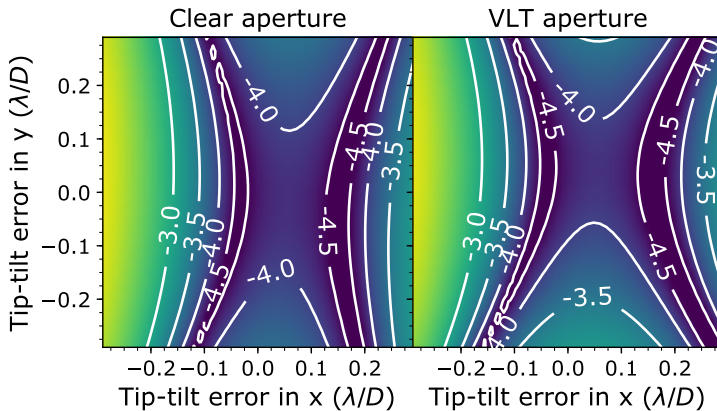
Figure 4.13: Map of the worst contrast through an off-axis fiber over a 10% bandwidth as a function of tip-tilt error upstream of the microlens array. This shows that the coronagraph is reasonably stable against tip-tilt, allowing for a $\sim 0.15\lambda/D$ tip-tilt error until the contrast drops to 10^{-4}. The contour labels indicate $\log_{10}(\eta_s/\eta_p)$.

4.4.3   Spectral bandwidth

Figures 4.7 and 4.8 show the chromatic response for all designs. Every design exhibits the double-dipped structure of the second-order null on the fiber. For all designs with a non-zero spectral bandwidth, we can also see that the contrast is hard to achieve on the long wavelength side. At these longer wavelengths the bright Airy core starts to grow into the microlens array. This means that the second Airy ring needs to be made much brighter to compensate, which requires substantial deviations in the phase pattern. Qualitatively, the location of the second null is chosen by the optimizer such that the spectral bandwidth requirement is reached.

4.4.4   Tip-tilt sensitivity and stellar diameter

Figure 4.13 shows the average contrast (η_s/η_p) over the full 10% bandwidth as a function of tip-tilt error upstream of the fiber injection unit. The double-dip structure is again clearly visible, which greatly improves the tip-tilt response. Both coronagraph designs achieve a tip-tilt stability of $\sim 0.1\lambda/D$ rms. This figure also shows that the SCAR coronagraph is insensitive for stars with an angular diameter up to $0.1\lambda/D$.

4.4.5   Sensitivity to other aberrations

To show the sensitivity to other aberrations, we perform a sensitivity analysis on the SCAR coronagraph: we aim to find the mode basis of orthogonal modes ordered by their sensitivity. These principal modes can be found by taking the first-order Taylor expansion of the phase in the pupil-plane around the nominal position. In this way a linear transformation G_λ can be constructed from a phase deformation $\delta\varphi$ to the resulting change in electric field in the fibers δE_λ:

$$\delta E_\lambda = G_\lambda \delta\varphi. \tag{4.6}$$

G_λ and δE_λ both depend on wavelength as the response of the coronagraph is inherently chromatic. A singular value decomposition of the matrix G_λ yields the monochromatic principal phase modes of the coronagraph. The corresponding singular values denote the importance of those modes. This expansion is similar to the one used in electric field conjugation (Give'on et al., 2007).

Broadband principal modes can be obtained by stacking several G_λ matrices for wavelengths within the spectral bandwidth into a single matrix G as

$$\begin{bmatrix} \delta E_{\lambda_1} \\ \delta E_{\lambda_2} \\ \vdots \\ \delta E_{\lambda_N} \end{bmatrix} = \begin{bmatrix} G_{\lambda_1} \\ G_{\lambda_2} \\ \vdots \\ G_{\lambda_N} \end{bmatrix} \delta\varphi. \tag{4.7}$$

A singular value decomposition on the matrix G now yields the broadband principal modes. The singular values are now indicative of the amount of electric field each phase mode induces in the fibers as a function of wavelength. This method is again similar to the one used in broadband electric field conjugation (Give'on et al., 2007).

Figure 4.14 shows the broadband principal modes for the SCAR design for the VLT aperture, along with their singular values. Only six modes are important for the final contrast. Naively we would expect two modes per fiber, so 12 modes in total, as we need to control both the real and imaginary part of the electric field. However in our case the system shows an antihermitian symmetry: the transmitted electric field on fibers in opposite points in the focal plane are not independent if only small phase aberrations are present. This means that one phase mode determines the electric field for both fibers so that only two modes per two fibers are needed. Only half of the original 12 modes determine the contrast in a monochromatic system, meaning that six modes are left. The omitted six modes correspond

to amplitude errors. For the broadband principal modes we of course expect some additional modes with low importance, corresponding to the spectral bandwidth increase. The first six of these are shown as modes 7 to 12 in Fig. 4.14.

The first principal mode is trefoil, which is the result of the six-fold symmetry in the fiber locations. The second trefoil is missing: its corresponding electric field change is completely filtered out by the single-mode fibers: it creates radial first-order nulls directly on the center of every lenslet. Other important modes include secondary-astigmatism-like modes for modes 2 and 3, coma-like modes for modes 4 and 5, and a perturbed spherical mode for mode 6.

In Fig. 4.15 we show the response of the SCAR coronagraph to each of these modes. The average normalized irradiance is the average raw contrast over the full spectral bandwidth and all six fibers in the first ring of microlenses. It can be seen that the response for the first six modes is generally a lot stronger than that of the last six. The average raw contrast is limited by the residual leakage from the SCAR coronagraph at the low aberration end, while the contrast increases when more aberration is added. Additionally, we can see different behaviour, depending on the mode that we are looking at. Some modes (modes 1 to 6, 9, 11 and 12) show quadratic behaviour, while others (modes 7, 8 and 10) show a fourth order behaviour. Also notice that mode 7 actually increase the average raw contrast. While this may seem an impossibility, as the SCAR coronagraph is optimized for raw contrast, in these cases the fibers on one side become brighter than the contrast constraint, while the others compensate by becoming dimmer. This would actually decrease the effectiveness of the coronagraph while still increasing the average raw contrast.

4.5 Comparison to the vortex coronagraph

The described performance of the SCAR coronagraph begs the question on how it compares to other coronagraphs using single-mode fibers. In this section we will provide a comparison of the SCAR coronagraph with the single-mode fiber injection unit with vortex coronagraph proposed by Mawet et al. (2017), and a comparison with a multiplexed fiber injection unit as shown in Sect. 4.3 behind a vortex coronagraph. Figure 4.16 shows the throughput and relative integration time of a conventional vortex coronagraph using a clear aperture. A conventional intensity detector (ie. sum of all flux in an aperture centered around the star) is compared with a
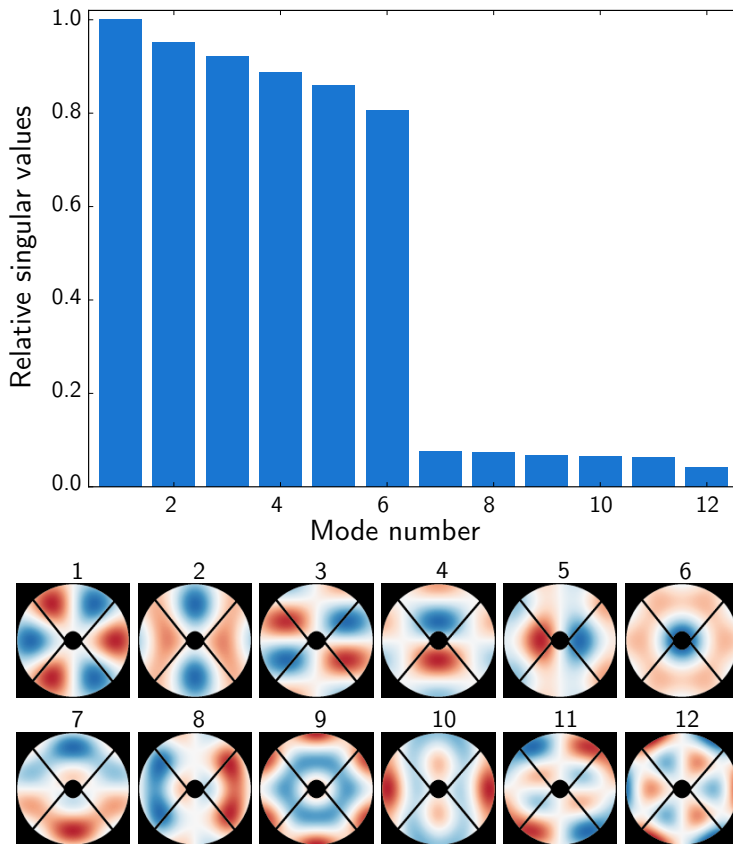
Figure 4.14: Principal phase modes for the SCAR coronagraph using the design described in the text. The top panel shows the singular value of each mode, indicating its significance for the obtained contrast after phase correction. The bottom panel shows the pupil-plane phase for each mode.
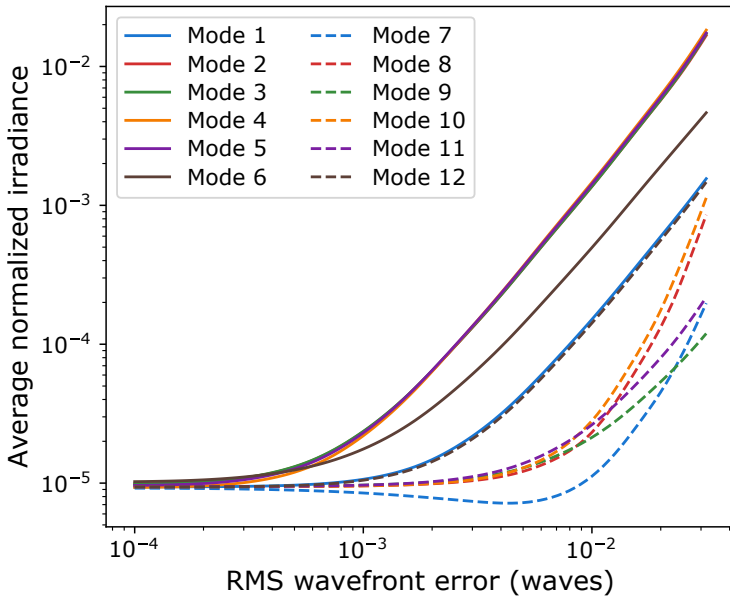
Figure 4.15: Average normalized irradiance for each of the modes in Fig. 4.14. The normalized irradiance is averaged over all fibers in the first ring of microlenses, and over the full 10% spectral bandwidth. These curves can yield constraints on the post-AO residual variance for each of the shown modes. Higher-order modes in this expansion generally have less response and do not have to be controller as well as low-order modes.

single-mode fiber centered around the planet. The mode field diameter was optimized for maximum throughput of the PSF without a coronagraph. To better capture the best and worst case performance for comparison with the vortex coronagraph, we take a telescope tip-tilt jitters of $0.05\lambda/D$ for the best case performance and $0.15\lambda/D$ for the worst case performance Similarly to Fig. 4.11, a telescope tip-tilt jitter of $0.1\lambda/D$ rms was chosen.

For charges $m = 4$ and $m = 6$ a decrease in throughput, compared to the vortex coronagraph with multimode fiber, can be seen, approximately corresponding with the maximum coupling of an Airy pattern through a Gaussian single-mode fiber. Additionally the vortex in the focal plane imprints a phase ramp on off-axis sources, which degrades throughput even further. This effect is more pronounced with smaller angular separations and higher charge vortices. Most of this phase ramp can be easily negated by tilting the fiber slightly, depending on the focal-plane position of the planet. We can see that the SCAR coronagraph wins in throughput compared to vortex coronagraphs with charger $m > 2$. However the charge 2 vortex coronagraph does not suppress the star very well, resulting in a moderate relative integration time compared to the SCAR coronagraph.

Figure 4.17 shows the throughput and relative integration time of a vortex coronagraph charge $m = 2$ through a microlens-fed single-mode fiber-array as the fiber injection unit. The diameter of the microlenses is varied from 1.4 to $2.0\lambda/D$, and the mode field diameter is optimized for maximum throughput of an Airy pattern. For large angular separations the throughput oscillates due to the transmission of the microlens array as shown in Fig. 4.4. For the first ring of microlenses the throughput rises quickly, again reaching its maximum at the center of the microlens. Even though the coupling efficiency for smaller microlenses is higher, the geometric throughput decreases more rapidly. A trade-off between these two throughput terms leads to an optimal microlens diameter of $\sim 1.8\lambda/D$ for the vortex coronagraph as well. The throughput at this microlens diameter is comparable to the performance of the SCAR coronagraph even though the vortex coronagraph has a more complicated optical setup. This multiplexed single-mode fiber vortex coronagraph however does not suppress starlight as well as the SCAR, leading to a worse relative integration time. The vortex coronagraph however does have the advantage of an infinite outer working angle.
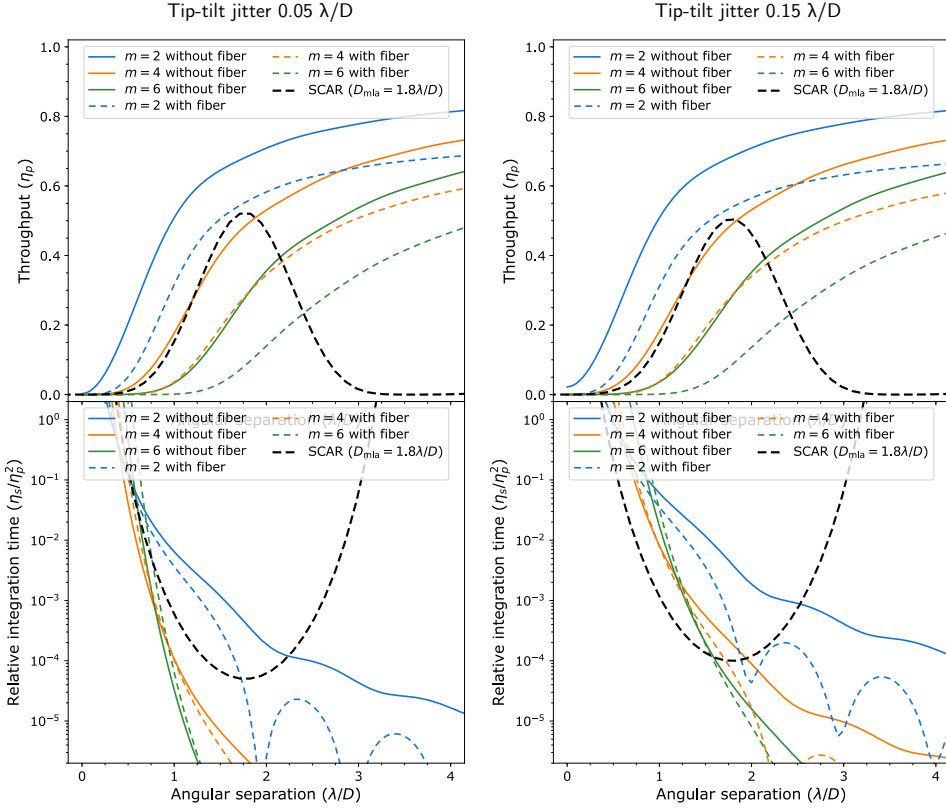
Figure 4.16: The throughput (η_p) and relative integration time (η_s/η_p^2) for a vortex coronagraph using a clear aperture for charges $m = 2, 4, 6$ using a conventional intensity detector or a single-mode fiber centered around the planet. A telescope tip-tilt jitter of (left column) $0.05\lambda/D$ or (right column) $0.15\lambda/D$ rms was taken into account. These values correspond to a best and worst case performance of the adaptive optics system. The throughput is calculated for the optimal position angle of the off-axis source (ie. directly across an off-axis microlens). For the vortex coronagraph without fiber, the throughput and relative integration time is calculated on an aperture of radius $0.7\lambda/D$ centered around the planet.
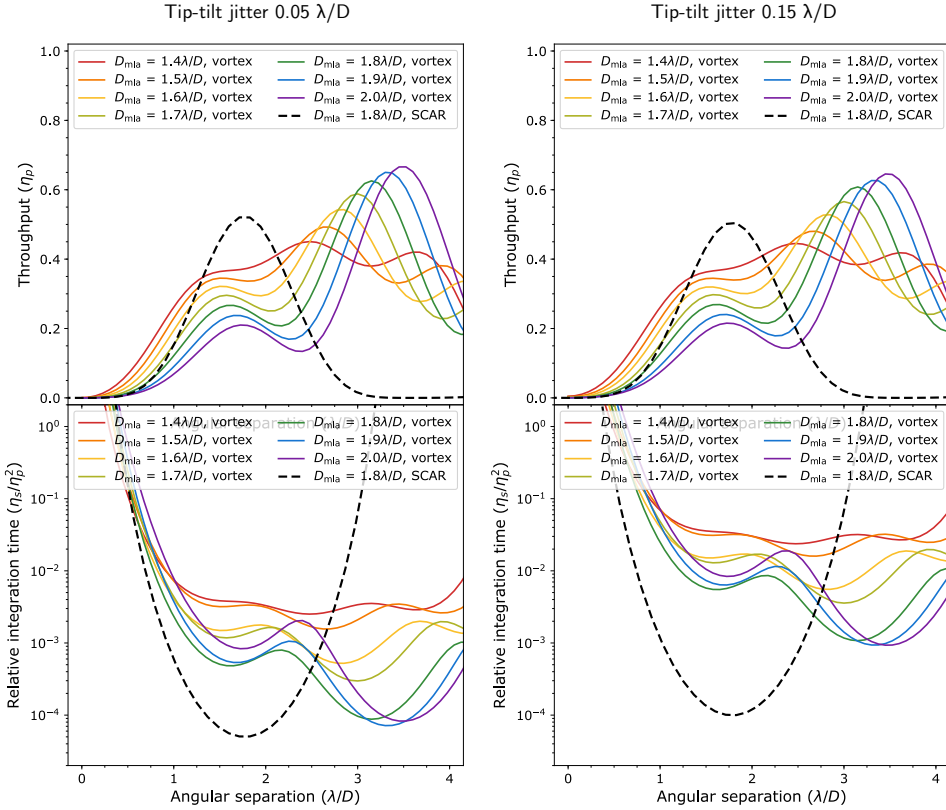
Figure 4.17: The throughput (η_p) and relative integration time (η_s/η_p^2) of a charge $m = 2$ vortex coronagraph on a microlens-fed single-mode fiber array. The diameter of the microlenses is varied from 1.4 to $2.0\lambda/D$, and the mode field diameter is optimized for maximum throughput of an Airy pattern. The throughput of the SCAR coronagraph designed for $1.8\lambda/D$ microlens diameter was added for comparison. The assumed tip-tilt jitter is (left column) $0.05\lambda/D$ or (right column) $0.15\lambda/D$ rms. These values correspond to a best and worst case performance of the adaptive optics system. The throughput is calculated for the optimal position angle of the off-axis source (ie. directly across an off-axis microlens).

4.6   Conclusion

In this paper we described the principle behind coronagraphs leveraging the design freedom offered by the use of single-mode fibers as a mode filter. We have shown the properties of a microlens-array fed single-mode fiber-array, making it possible to perform exoplanet searches. We combined this with a pupil-plane phase plate, yielding the SCAR coronagraph and presented the following advantages of this new coronagraph:

1. *Low inner working angles.* Inner working angles as low as $1\lambda/D$ can be reached using current designs.

2. *High throughput.* These designs reach a maximum throughput of 50% and 30% for a clear and the VLT aperture, respectively.

3. *High contrast.* Starlight can be suppressed to $< 3 \times 10^{-5}$ for the six fibers surrounding the star over the full spectral bandwidth until the throughput starts to drop.

4. *Broad spectral bandwidth.* This suppression is achieved over the full 20% spectral bandwidth.

5. *Robust against tip-tilt errors.* The SCAR coronagraph is stable against $\sim 0.1\lambda/D$ rms tip-tilt errors upstream due to the use of second order nulling on the fibers.

6. *Residual speckle suppression.* Residual speckles are are reduced by $\sim 3\times$ in intensity, due to the coupling efficiency of a random electric field into the single-mode fibers.

All advantages can be obtained into a single SCAR design. All these advantages make this coronagraph a prime candidate for future upgrades of extreme AO systems. In particular, the SCAR coronagraph is perfectly suited for spectral characterization of Proxima b: it satisfies all coronagraphic requirements set by Lovis et al. (2017). A companion paper (Haffert et al., 2018) provides a tolerancing study for this specific application.

Future research will explore active control of the fiber throughput of the SCAR coronagraph. Application of the SCAR methodology to other coronagraphs is also left for future research. An interesting example in this case is the design of a Lyot-plane mask for a conventional Lyot or vortex coronagraph, akin to Ruane et al. (2015a). Even optimizing the focal-plane mask itself might be realizable for the fiber array in these coronagraphs (Ruane et al., 2015b).

Another avenue is the use of photonic technologies to further process the light in the fibers. A simple example is the use of fiber Bragg gratings for filtering the atmospheric OH lines (Trinh et al., 2013). Another example is building a phase-shifting interferometer of the six fibers. This will provide information about the coherence of the light in each of the fibers with respect to the star, and would allow for synchronous interferometric speckle subtraction (Guyon, 2004).

Bibliography

Aime, C., & Soummer, R. 2004, The Astrophysical Journal Letters, 612, L85

Anglada-Escudé, G., Amado, P. J., Barnes, J., et al. 2016, Nature, 536, 437

Beuzit, J.-L., Feldt, M., Dohlen, K., et al. 2008, in SPIE Astronomical Telescopes+ Instrumentation, International Society for Optics and Photonics, 701418–701418

Borucki, W. J., Koch, D. G., Basri, G., et al. 2011, The Astrophysical Journal, 736, 19

Brogi, M., Snellen, I. A., de Kok, R. J., et al. 2012, Nature, 486, 502

Carlotti, A., Kasdin, N. J., Vanderbei, R. J., & Riggs, A. E. 2013, in SPIE Optical Engineering+ Applications, International Society for Optics and Photonics, 88641Q–88641Q

Cavarroc, C., Boccaletti, A., Baudoz, P., Fusco, T., & Rouan, D. 2006, Astronomy & Astrophysics, 447, 397

Codona, J., Kenworthy, M., Hinz, P., Angel, J., & Woolf, N. 2006, in SPIE Astronomical Telescopes+ Instrumentation, International Society for Optics and Photonics, 62691N–62691N

Corbett, J. C. 2009, Optics express, 17, 1885

Fusco, T., Sauvage, J.-F., Mouillet, D., et al. 2016, in SPIE Astronomical Telescopes+ Instrumentation, International Society for Optics and Photonics, 99090U–99090U

Give'on, A., Kern, B., Shaklan, S., Moody, D. C., & Pueyo, L. 2007, in Optical Engineering+ Applications, International Society for Optics and Photonics, 66910A–66910A

Gurobi Optimization, I. 2016, Gurobi Optimizer Reference Manual. `http://www.gurobi.com`

Guyon, O. 2004, The Astrophysical Journal, 615, 562

—. 2005, The Astrophysical Journal, 629, 592

Guyon, O., Pluznik, E., Kuchner, M., Collins, B., & Ridgway, S. 2006, The Astrophysical Journal Supplement Series, 167, 81

Haffert, S. Y., Por, E. H., Keller, C. U., et al. 2018, arXiv e-prints, arXiv:1803.10693. `https://arxiv.org/abs/1803.10693`

Haguenauer, P., & Serabyn, E. 2006, Applied optics, 45, 2749

Hanot, C., Mennesson, B., Martin, S., et al. 2011, The Astrophysical Journal, 729, 110

Jovanovic, N., Martinache, F., Guyon, O., et al. 2015, Publications of the Astronomical Society of the Pacific, 127, 890

Kawahara, H., Murakami, N., Matsuo, T., & Kotani, T. 2014, The Astrophysical Journal Supplement Series, 212, 27

Kipping, D. M., Cameron, C., Hartman, J. D., et al. 2017, The Astronomical Journal, 153, 93

Konopacky, Q. M., Barman, T. S., Macintosh, B. A., & Marois, C. 2013, Science, 339, 1398

Lovis, C., Snellen, I., Mouillet, D., et al. 2017, Astronomy & Astrophysics, 599, A16

Macintosh, B., Graham, J. R., Ingraham, P., et al. 2014, Proceedings of the National Academy of Sciences, 111, 12661

Marcuse, D. 1978, JOSA, 68, 103

Marois, C., Lafreniere, D., Doyon, R., Macintosh, B., & Nadeau, D. 2006, The Astrophysical Journal, 641, 556

Martin, S., Serabyn, E., Liewer, K., et al. 2008, in Proc. SPIE, Vol. 7013. `https://doi.org/10.1117/12.789484`

Mawet, D., Pueyo, L., Lawson, P., et al. 2012, in SPIE Astronomical Telescopes+ Instrumentation, International Society for Optics and Photonics, 844204–844204

Mawet, D., Ruane, G., Xuan, W., et al. 2017, The Astrophysical Journal, 838, 92

Otten, G. P., Snik, F., Kenworthy, M. A., et al. 2017, The Astrophysical Journal, 834, 175

Pepe, F. A., Cristiani, S., Lopez, R. R., et al. 2010, in SPIE Astronomical Telescopes+ Instrumentation, International Society for Optics and Photonics, 77350F–77350F

Por, E. H. 2017, in Techniques and Instrumentation for Detection of Exoplanets VIII, Vol. 10400, International Society for Optics and Photonics, 104000V

Riaud, P., & Schneider, J. 2007, Astronomy & Astrophysics, 469, 355

Ruane, G. J., Huby, E., Absil, O., et al. 2015a, Astronomy & Astrophysics, 583, A81

Ruane, G. J., Swartzlander, G. A., Slussarenko, S., Marrucci, L., & Dennis, M. R. 2015b, Optica, 2, 147

Snellen, I., de Kok, R., Birkby, J., et al. 2015, Astronomy & Astrophysics, 576, A59

Snellen, I. A., Brandl, B. R., de Kok, R. J., et al. 2014, Nature, 509, 63

Snik, F., Otten, G., Kenworthy, M., et al. 2012, in SPIE Astronomical Telescopes+ Instrumentation, 84500M–84500M

Sparks, W. B., & Ford, H. C. 2002, The Astrophysical Journal, 578, 543

Trinh, C. Q., Ellis, S. C., Bland-Hawthorn, J., et al. 2013, The Astronomical Journal, 145, 51

Wang, J., Mawet, D., Ruane, G., Hu, R., & Benneke, B. 2017, The Astronomical Journal, 153, 183

5 | The Single-mode Complex Amplitude Refinement (SCAR) coronagraph

II. Lab verification, and toward the characterization of Proxima b

We present the monochromatic lab verification of the newly developed SCAR coronagraph that combines a phase plate (PP) in the pupil with a microlens-fed single-mode fiber array in the focal plane. The two SCAR designs that have been measured, create respectively a 360 degree and 180 degree dark region from $0.8 - 2.4\lambda/D$ around the star. The 360 SCAR has been designed for a clear aperture and the 180 SCAR has been designed for a realistic aperture with central obscuration and spiders. The 360 SCAR creates a measured stellar null of $2 - 3 \times 10^{-4}$, and the 180 SCAR reaches a null of 1×10^{-4}. Their monochromatic contrast is maintained within a range of $\pm 0.16\lambda/D$ peak-to-valley tip-tilt, which shows the robustness against tip-tilt errors. The small inner working angle and tip-tilt stability makes the SCAR coronagraph a very promising technique for an upgrade of current high-contrast instruments to characterize and detect exoplanets in the solar neighborhood.

5.1 Introduction

We are currently at a breakthrough moment where more and more Earth-like exoplanets are being discovered. Every detection of Earth-sized planets brings us closer to finding life on another planet. The recent discovery of Proxima Centauri b (Anglada-Escudé et al., 2016) confirms that the solar neighborhood has many planets waiting to be discovered. From current surveys it is also clear that most of the planets in the habitable zone will have a separation close to the diffraction limit of current and future large telescopes. Characterization and detection of these planets can be done through high-contrast imaging, which overcomes the huge contrast between planet and star.

While the indirect methods have been very successful in discovering planets, direct imaging of exoplanets is lagging behind in the number of planets. This is mainly due to the difficulties involved in direct imaging. The largest problem is the close angular position of the planet to the star which is at best a few λ/D according to the current statistics of exoplanet orbits (Galicher et al., 2016). Here λ is the wavelength used to observe the system and D the telescope diameter.

The influence of the photon noise on the planet can be reduced by spatially separating the planet signal from the stellar signal. Current and future large optical telescopes have the resolution to resolve planets from their host star. This is done by using extreme adaptive optics (XAO) systems to enable imaging at the diffraction limit on ground based telescopes. The spatial separation also enables the use of coronagraphs to suppress the stellar light. This is the common approach on high contrast imaging (HCI) instruments like SPHERE (Beuzit et al., 2008), GPI (Macintosh et al., 2014) and SCExAO (Jovanovic et al., 2015).

Combining HCI with high-resolution spectroscopy (HRS) over a broad wavelength range gains further orders of magnitude in contrast close to the star (Riaud & Schneider, 2007; Sparks & Ford, 2002), because high-resolution spectra are able to exploit the difference in spectral lines between the star and planet. This difference can be due to a different Doppler velocity for reflected light and/or due to the presence of different molecular species. This technique has been successfully applied to characterize the atmosphere of several giant exoplanets (Brogi et al., 2012; Konopacky et al., 2013; Snellen et al., 2014). Recent papers (Kawahara et al., 2014; Snellen et al., 2015; Wang et al., 2017) show that this can be used as a robust post processing technique to remove residual stellar speckles which limit current HCI instruments (Aime & Soummer, 2004; Martinez et al., 2012). Snellen

et al. simulated a hypothetical Earth-like twin around Proxima Centauri for the European Extremely Large Telescope(E-ELT). The combination of HCI and HRS was able to detect and even characterize the Earth twin. The discovery of an actual Earth-like planet around Proxima Centauri makes this technique even more relevant as Lovis et al. show that an upgraded SPHERE (SPHERE+) can be used to characterize Proxima b if it is coupled to a high-resolution spectrograph. In this approach the focal plane of SPHERE+ would be coupled through a fiber link to the high-resolution spectrograph.

Mawet et al. (2017) argue that using a single-mode fiber (SMF) link between HCI and HRS instruments has an advantage over multi-mode fibers (MMF). A single-mode fiber is more robust against speckle noise due to the mode filtering capabilities. This property has been appreciated by the interferometry community, where single-mode fibers or waveguides are used to combine and filter multiple beams. Mawet et al. considers a system where the coronagraph and fiber injection unit (FIU) act separately on the stellar light. In the companion paper(Paper I) Por & Haffert (2017) we demonstrate the concept of the SCAR coronagraph, where am pupil plane phase plate is designed that uses the properties of the single-mode fiber to reach a deep null close to the star. This system is related to the Apodizing Phase Plate (APP) (Codona et al., 2006; Otten et al., 2017), which also uses an pupil plane phase optics to create dark holes in the PSF. The main difference is that the APP creates a dark hole by reducing the intensity, while SCAR changes the electric field such that the light can be rejected by a single-mode fiber. The SCAR coronagraph can work over a broad spectral bandwidth with high throughput and is tip-tilt insensitive to a large extent. It is well suited to be used as the interface between high-contrast imaging instruments and high-resolution spectrographs. This is the first system that combines the FIU and coronagraph in a single unit.

The SCAR coronagraph works on the basis of electric field filtering by electric field sensitive photonics. The implementation of this work uses single-mode fibers. With the advances of AO and especially extreme AO it is possible to achieve high coupling efficiency into SMFs (Bechter et al., 2016; Jovanovic et al., 2017). The amount of light that couples into a single-mode fiber is defined by the coupling efficiency

$$\eta = \frac{\left| \int E_{\mathrm{in}}^* E_{\mathrm{SMF}} dA \right|^2}{\int |E_{\mathrm{in}}|^2 dA \int |E_{\mathrm{SMF}}|^2 dA}. \tag{5.1}$$

Here η is the relative amount of light from E_{in} that is coupled into a single-mode fiber with mode profile E_{SMF}. For a SMF the mode profile

is Gaussian. The light that couples into a SMF is effectively averaged by a Gaussian weighing function. Due to this property if the electric field is zero on average it will not couple into the fiber and is rejected. A remarkable property here is that the intensity does not have to be zero, while the electric field can be. This is a much less stringent requirement than the zero intensity for normal high-contrast imaging. The phase plate is used to modify the point spread function (PSF) in such a way that the stellar light couples very badly into the fiber, but the planet still couples well. This coherent imaging approach is very reminiscent of interferometry where these kind of approaches have been used (Angel et al., 1986; Labadie et al., 2007). Because of the benefits of coherent imaging such approaches are now also starting to be exploited for conventional direct imaging (Mawet et al., 2017).

In this paper we show the first lab verification of the SCAR coronagraph and look at the manufacturing feasibility with Monte Carlo simulations. Section 2 describes the optical setup for the measurements and the lab results. And in Section 3 the manufacturing requirements are derived and a Monte Carlo simulation is done to estimate the expected performance. Section 4 summarizes the results of our study.

5.2   Optical setup details and first results

5.2.1   Lab setup description

The SCAR coronagraph uses a single-mode fiber array fed by a microlens array. A detailed theoretical description can be found in Paper I. To measure the SCAR performance we created a setup that can emulate the measurements of a microlens fed fiber array. The setup was built in Leiden on a vibration damped optical table in air without any active controlled components. The lab setup used for the measurements can be seen in Figure 5.1. The input source to our setup was a single-mode fiber with a 2.8-4.1 μm Mode Field Diameter(MFD) at 488 nm, that is fed by a helium neon laser. The fiber was mounted on a XYZ-translation stage. A Thorlabs AC508-1000-B achromatic doublet with a focal length of 1000 mm collimates the fiber. And just before the conjugated plane we placed a pupil stop with a diameter of 3.8 mm. This pupil diameter combined with the 1000 mm focal length ensures that the input source's MFD $\approx 0.02\lambda/D$ which is much smaller than λ/D and therefore creates a good clean point source.

In the conjugated plane slightly behind the pupil stop we placed the
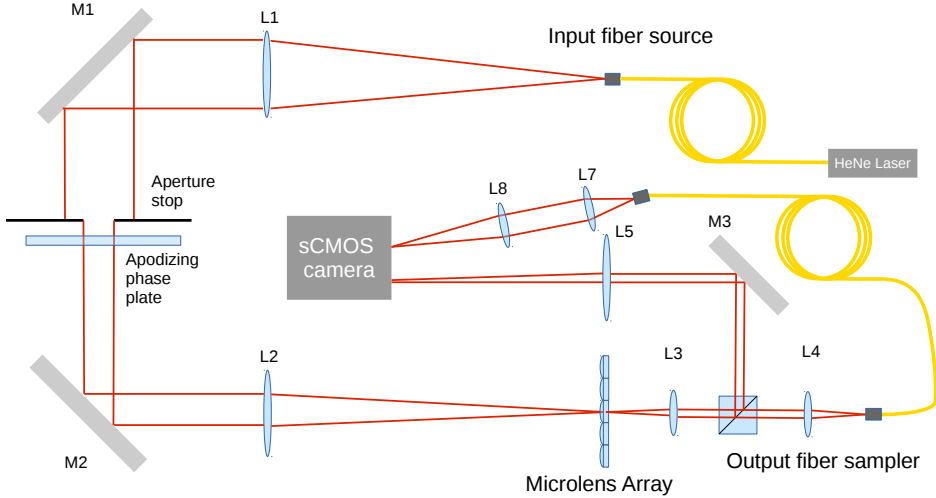
Figure 5.1: Schematic of the lab setup. The gray colored surfaces labeled M1 to M3 are mirrors. The blue shaded surfaces L1 to L8 are lenses. The yellow curves represent the single-mode fibers. The central wavelength of the setup is 0.633 nm.

phase plate which modifies the PSF. Another Thorlabs AC508-1000-B achromatic double focusses the light. The resulting PSF is sampled by Okotech APH-Q-P250-F2 hexagonal Micro Lens Array (MLA) with a pitch and diameter of 250 μm and a 2.18 mm focal length. The scale of the PSF is 166 μm per λ/D, this means that each microlens samples 1.5 λ/D. The MLA sampled PSF is relayed by a set of achromatic doublet lenses which have focal lengths of respectively 100 mm and 75 mm. In the intermediate collimated beam we placed a 90/10 beam splitter which splits 90 percent of the light toward a single-mode fiber and ten percent toward a camera. The transmitted beam was sampled by a LMA-8 photonic crystal fiber of NKT Photonics. This fiber has a mode field diameter of 8.4 μm $\pm$ 1.0 μm that is constant as a function of wavelength. The output of this fiber is reimaged on a Andor Zyla sCMOS camera by two positive achromatic doublets. The reflected beam is focused by a 500 mm lens to create an image of the MLA spots onto the same Andor camera. Both the microlens spots and the fiber coupling can be monitored at the same time in this way.

This setup was only able to measure the light coupling through the on-axis central lenslet because there is only a single fiber. So to emulate the

measurements through an off-axis lenslet the input source was shifted. This
relaxes the alignment requirements because the fiber alignment is critical.
The fiber has to be aligned within 1/8th of the MFD to create a deep null.
Moving the fiber every time to a new lenslet to sample its throughput would
be very time consuming due to this alignment requirement. Shifting the
PSF is easier because $1\lambda/D$ is 166 μm. With a set of digitial micrometer
actuators from Thorlabs we were able to shift the PSF with micron accu-
racy and precision. With this scanning strategy we were able to perform
repeatable sub-λ/D shifts and measure the throughput as function of shift
with respect to the central microlens. The actuator range is two inch which
allowed us to scan a range of $\pm 150\lambda/D$.

5.2.2   Fiber alignment procedure

A misalignment of the output fiber can lead to a reduction in throughput
and off-axis nulling. A good alignment is therefore critical. The fiber
alignment is done in multiple steps to ensure good nulling. First the input
source is aligned on the central microlens without a phase plate in the
beam. The microlens spots, which can be viewed on the camera, should
be radially symmetric in intensity after this first step because the PSF is
radially symmetric. During the second step the fiber is coarsely aligned to
find the brightest spot in the field which is done by moving the fiber such
that the brightest spot can be seen by eye on the fiber face. The last step
takes care of the fine alignment by moving the fiber such that the fiber
throughput is maximized.

5.2.3   Apodizing phase plate designs

Two different SCAR designs have been measured in our setup. The first
design is a phase pattern that generates a 360 degree dark region in the
first ring of lenslets around the PSF with a contrast of 5×10^{-5} and a
throughput of 30 percent. The throughput includes the coupling efficiency
into the SMF. The second design is a 180 degree phase pattern with a
central obscuration and spiders. This creates a one-sided dark region next
to the PSF with a contrast of 1×10^{-5} and a 60 percent throughput. Both
patterns are designed for a spectral bandwidth of 20 percent. The phase
patterns with their corresponding PSFs can be seen in Figure 5.2.
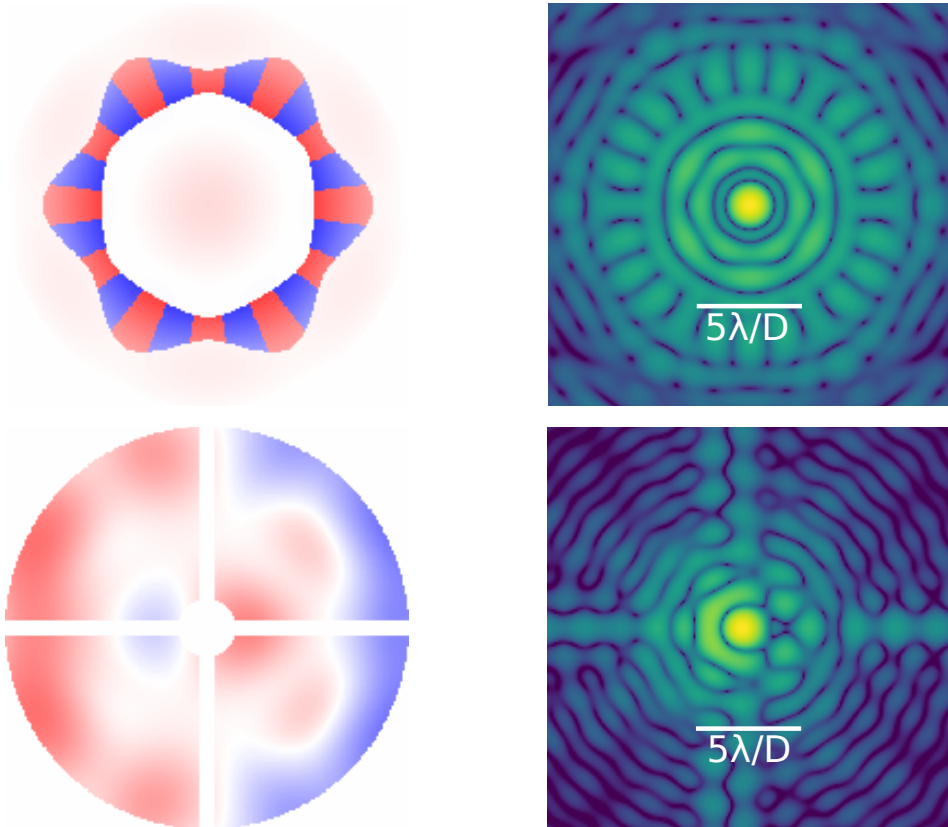
Figure 5.2: Left column shows theoretical phase pattern. Here blue is π phase, white is zero phase and red is $-\pi$ phase. The corresponding PSF is shown on the right with a 5 λ/D scale bar. Both images of the PSF are on log scale with the color scale shown on the right. The first phase pattern creates a 360 dark region for a clear aperture. The second pattern creates a one-sided dark region for a pupil that has a central obscuration and spiders.

5.2.4 Liquid crystal plate

The phase plates are manufactured by using a direct write approach where the fast axis of the liquid crystals is written with a laser (Miskiewicz & Escuti, 2014; Snik et al., 2012). The liquid crystals add a geometric phase to the incoming light which only depends on the angle of the fast axis. This then acts as an achromatic phase pattern with a chromatic piston term which can be ignored. An important aspect is that it acts on circular polarized light. Left circular and right circular polarizer light both get the same phase pattern but with a change of sign. Because of this it is important to separate the two polarizations. The separation is done by adding a tilt to the phase pattern, and because both polarization get opposite phase they split into different directions. This is also done in the grating-vAPP (Otten et al., 2014). If the liquid crystal plate is not perfectly half-wave there will be a leakage term that does not see the phase pattern. The leakage creates a normal Airy pattern. This can be seen in Figure 5.3.The leakage term can limit the contrast if the retarder substantially deviates from half wave. One way to reduced the effect of the leakage is to separate it like the grating-vAPP or use a technique like the double-grating vAPP where the leakage is scattered away (Doelman et al., 2017). For the results in this paper we used the grating-vAPP approach. The additional pair of spots in Fig. 5.3 are created by the grating mask (Doelman et al., 2017). The grating mask is a phase tilt that is applied outside the aperture. All the light that falls outside of the defined aperture diffracts due to the phase tilt. With the grating mask we can create a well defined aperture shape and size. Our phase plates were made with 8.75 μm LC pixels and the pupil itself is 3.8 mm allowing for 434 pixels across the pupil. The aperture spots fall off quickly enough that they do not influence the modified PSFs.

5.2.5 Lab setup results

The throughput as function of PSF position for the 360 SCAR can be seen in Fig. 5.4. The measured throughput is overlayed on the model curve. Given that the variables of our model are not fitted but taken as is from the manufacturing specifications, the measurements and the model agree very well. As said before this is the relative throughput as function of distance from a microlens center. This is not a contrast curve. For this system with microlenses the contrast curve is discrete and it only changes when going to another microlens as shown in Figure 5.5. The contrast is defined as the ratio between the coupling of the on-axis object and the

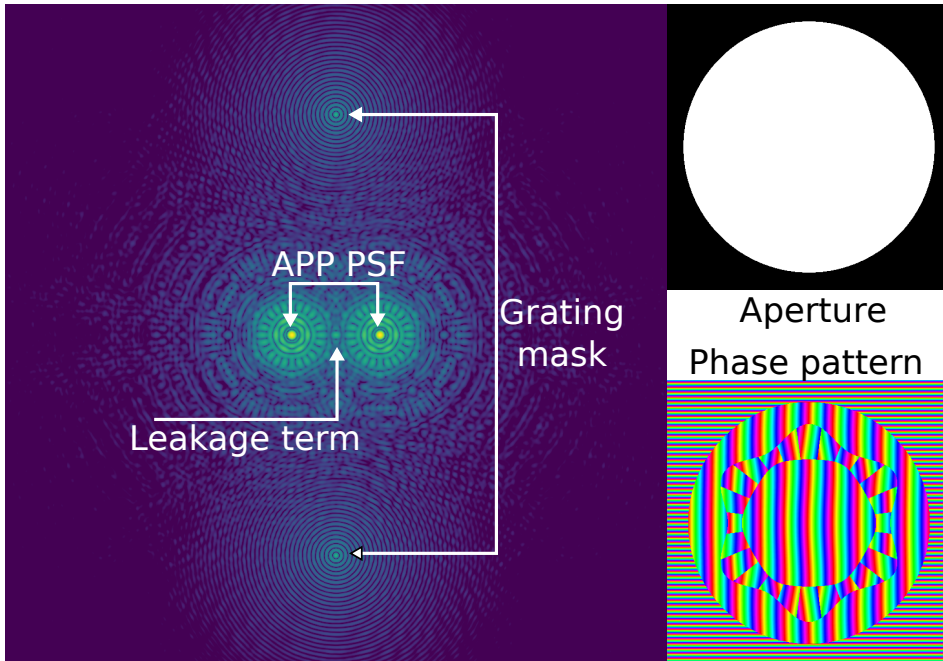Figure 5.3: Left: Simulated focal plane of the phase pattern. Right: Phase and aperture. On the focal plane several PSF's can be seen. The left and right PSFs are the PSFs that contain the phase pattern. The top and bottom correspond to the light that scatters away due to the grating mask. And in the center there is a 1 percent leakage term. The horizontal PSFs are at $\pm 10\lambda/D$ and the aperture PSFs are at $\pm 50\lambda/D$

off-axis object. Figure 5.5 shows that the contrast changes as the source moves over the microlens due to a change in throughput.

On the linear scale it is easier to read off the throughput loss as the source is shifted. The 50 % throughput is at an offset of 0.5 λ/D. We define the inner working angle as the smallest angular separation where the throughput of the companion is equal to 50% of the maximum, and the outer working angle as the largest angular separation where the throughput is equal to 50% of the maximum. A source has a maximum throughput when it is in the middle of a microlens and needs to shift by 0.5 λ/D for it to reach half the maximum throughput. Therefore we can define the effective inner and outer working angles as $1.1\lambda/D$ and $2.1\lambda/D$ for the first ring of lenslets.

At $0.75\lambda/D$ the PSF is precisely on the edge between two microlenses. At this position 25% throughput remains in each of the two fibers. So a total throughput of 50% is achieved by combining multiple fiber outputs. If a binary system is observed with field rotation then the relative throughput of the source fluctuates between 50% and 100% as it rotates over the lenslets. For an off-axis source that is on the edge between the central lenslet and an off-axis lenslet then we can only capture 25% of the off-axis source, but with an impressive source separation of $0.75\lambda/D$.

The contrast changes as a source moves over the micro-lens array because the throughput changes. This is shown in Figure 5.5. The MMF shows the intrinsic contrast for normal imaging. Compared to a MMF a SMF already increases the contrast by a factor of 10 due to the rejection of the nonGaussian modes that are in the PSF. The 360 SCAR can in theory reach an average contrast of 5×10^{-5} but we are limited by static aberrations in the system, which limit the contrast to 3×10^{-4} at $-1.5\lambda/D$ and 2×10^{-4} at $1.5\lambda/D$. The decrease of contrast can be attributed to 10 nm rms low order wavefront aberration, but this is a very rough estimate. The change in contrast is symmetric around $1.5\lambda/D$. The contrast of the right fiber stays below 1×10^{-3} and the left fiber stays below 2×10^{-3}. Figure 5.5 also shows that if the source is on a different microlens it can still couple into the other microlenses and reach an acceptable contrast.

The broad gap around $1.5\lambda/D$ in Figure 5.4 gives insight into the wavelength scaling and the effects of jitter. When the wavelength changes then λ/D changes and we have to check the stellar throughput at a different part of the curve. So the width of the gap is a measure for the bandwidth. The spectral bandwidth is then roughly $2 * \Delta\theta/\theta_0 \approx 0.2$ with $\Delta\theta$ the gap width and θ_0 the gap center. Next to the wavelength response it also says

something about the monochromatic jitter resistance. If the star jitters a bit then the off-axis throughput is still low because of the gap. The gap where we still achieve the contrast for the 360 SCAR is between $-1.8\lambda/D$ and $-1.3\lambda/D$. The gap on the right is from $1.36\lambda/D$ to $1.7\lambda/D$. This demonstrates that the coronagraph should be able to handle $\pm0.15\lambda/D$ monochromatic tip-tilt residuals. The SMF without any pupil phase optic in contrast has a very narrow rejection area. There is only one position at which it nulls the star and if there is a small amount of jitter the contrast quickly deteriorates to about 10^{-2}. This shows the advantage of SCAR, which creates a broad dark area. Because the system is completely passive it is also very robust. The dark region remained dark over several weeks.

The filtering effect of the -mode fiber can be seen in Figure 5.6, where the measured microlens spots around the deepest null are shown together with the fiber throughput. The spot has a triple peak structure that is created by the phase plate. The triple peak structure is the feature that increases the bandwidth and tip-tilt stability. This is characteristic of a second-order null. The triple peak structure can be seen in the middle frame of Figure 5.6. While the change in total power from frame to frame is small, the fiber throughput changes drastically. This shows the modal filtering capability of single mode fibers.

The throughput results for the 180 SCAR can be seen in Figure 5.7. The measurements reach a contrast of 1.15×10^{-4}. There is a mismatch between the measured and simulated throughput curves, but we can see that compared to the 360 design this design reaches a deeper contrast. The deepest part is also relatively flat between -1.7 and -1.4 λ/D. Because of the flat response the design can handle tip-tilt errors of $\pm0.15\lambda/D$. The corresponding constrast curves are shown in Figure 5.8. The contrast curves are asymmetrical due to the asymmetric PSF that is created by the 180 SCAR.

Apart from maximizing the contrast it is important to optimize the absolute throughput of the planet light through the fiber. For the proposed system we have defined the coupling not as the total amount of light that couples into the fiber, but as the amount of light that falls within the micro-lens aperture that couples into the fiber. The total amount of light that couples into the fiber depends on how much of the PSF the micro-lens captures. Therefore there is a trade-off between spatial resolution and throughput (Por & Haffert, 2017). The 360 SCAR has a maximum coupling of 87% percent for a single micro-lens. Due to the hexagonal shape of the micro-lens the maximum coupling efficiency is slightly higher than the 82%
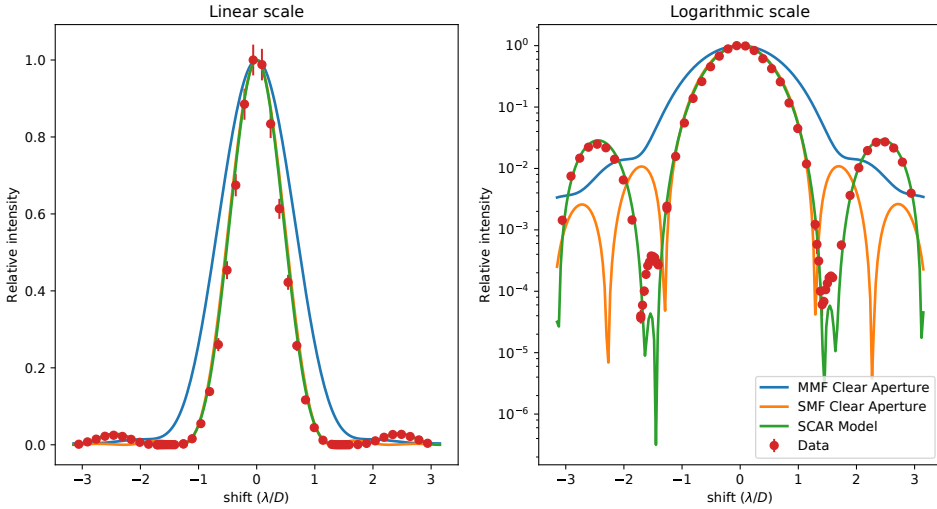
Figure 5.4: Left: Relative throughput on a linear scale as function of relative shift with respect to the microlens center. The red points are the measurements with errorbars due to random errors. The green line shows the model of this SCAR design. Right: Throughput on a logarithmic scale. The null is uneven between left and right and not as deep as designed. This is suspected to be caused by 10 nm rms residual low-order aberrations. The blue line shows the amount of light that falls on the microlens with a clear aperture and without SCAR. This is comparable to the contrast curve for normal imaging or using a multi-mode fiber. The orange line shows the normalized throughput with a unobstructed aperture and a SMF. The SMF shows a gain compared to the MMF.
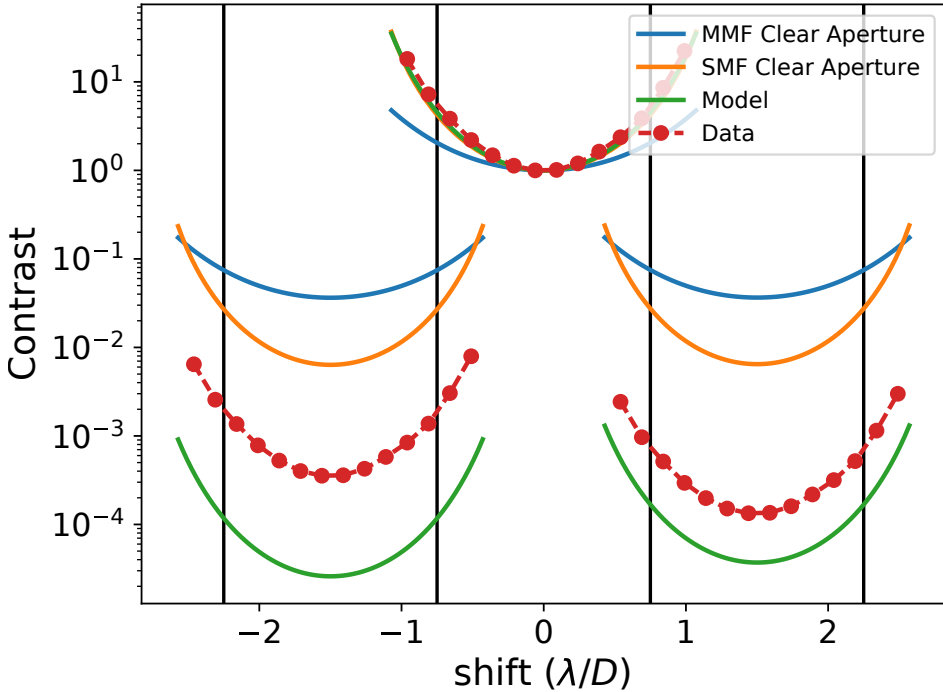
Figure 5.5: Contrast as a function of position on the microlens array. The black lines show the borders of the microlenses. The blue lines show the contrast for a multi-mode fiber. The orange lines show the contrast for a single-mode fiber. A single-mode fiber already provides extra contrast compared to a multi-mode fiber. The green lines show the model of the SCAR coronagraph, and the red dots are the measurements.
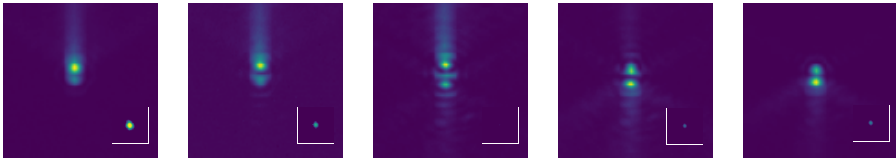
Figure 5.6: Measured microlens spot structure for the 360 SCAR. The inset shows the throughput of the single mode fiber. The deepest null occurs with a triple spot structure, which is a second order null due to the two zero crossings. The white circle shows the position and MFD of the fiber.
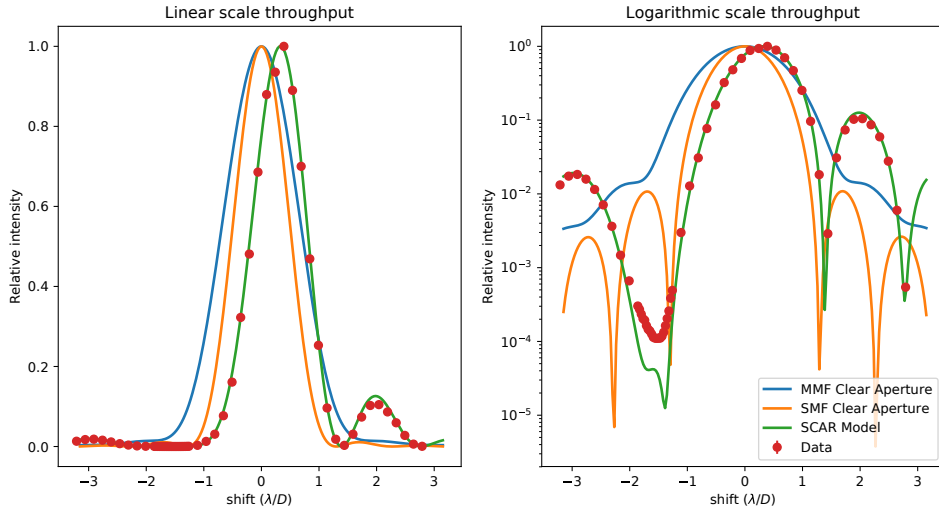
Figure 5.7: Left: Relative throughput on a linear scale as function of relative shift with respect to the microlens center. The green points are the measurements. Errorbars are included but are smaller than the size of the plotting symbols. The errorbars are very small and show that random errors can not explain the difference between the model and the measurements. The orange line shows the nonfitted model of this SCAR design. Right: Throughput on a logarithmic scale. The deepest contrast that we reach is 1.15×10^{-4}. The throughput curve is also flat between -1.6 and -1.4 λ/D. The measured null does not reach the design null due to residual low order aberrations aberrations on the order of 10 nm rms. The blue curve shows the amount of light that falls in a microlens of a clear aperture, which shows the contrast without SCAR. This is comparable to the raw contrast curve for normal imaging or using a multi-mode fiber. The orange line shows the normalized throughput with an unobstructed aperture and a SMF. The SMF shows a gain compared to the MMF.
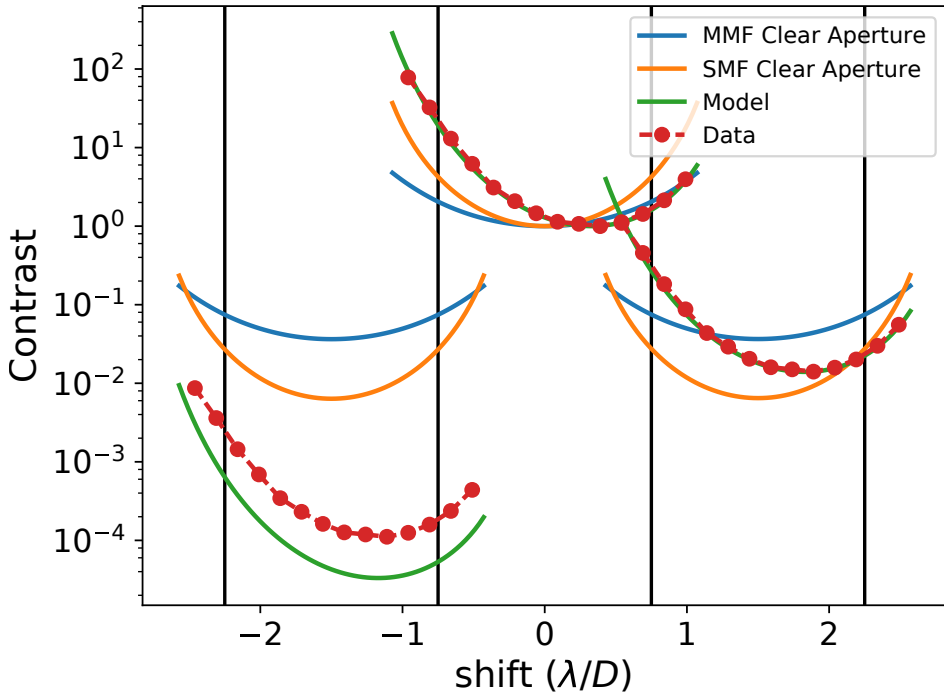
Figure 5.8: Contrast as a function of position on the microlens array. The black lines show the borders of the microlenses. The blue lines show the contrast for a multi-mode fiber. The orange lines show the contrast for a single-mode fiber. A single-mode fiber already provides extra contrast compared to a multi-mode fiber. The green lines show the model of the SCAR coronagraph, and the red dots are the measurements.

theoretical maximum for circular apertures (Shaklan & Roddier, 1988). Our lab measurement of the coupling was defined as the ratio between the fiber spot intensity and the MLA spot intensity. After correcting for the uneven beam-splitter between the two spots our absolute coupling is 76 ± 3 %. This includes Fresnel losses at the interface of the fiber, fiber propagation losses and roughness due to the polishing of the fiber. The measured coupling is very close to the theoretical maximum if we consider these losses. The absolute throughput is the product of the coupling, a correction for the spatial sampling and the Strehl ratio of the phase plate. The measured absolute throughput is $26 \pm 1\%$.

5.3   Tolerance simulation analysis

Lovis et al. (2017) show that within certain assumptions about Proxima b that it can be characterized by combining SPHERE+ with a high-resolution spectrograph (ESPRESSO in this case). Several challenges are to be solved. Current coronagraphs on SPHERE are not able to suppress the stellar diffraction halo at the position of Proxima b with the required contrast, and the AO system is not good enough at the angular separation of Proxima b. Lovis et al. (2017) propose SPHERE+ where both the coronagraph and the AO system are upgraded. Switching from a Shack-Hartmann wavefront sensor to a Pyramid wavefront sensor would greatly improve performance at small inner working angles (Fusco et al., 2006; Vérinaud et al., 2005). For SPHERE+ Lovis et al. assumed a hypothetical coronagraph. The listed requirements of this coronagraph are:

- A contrast of at least 5000.

- A relatively broad wavelength range of at least 20 percent.

- The stellar rejection region should encompass the orbit of Proxima Centauri b, which has a maximum estimated separation of 36 milliarcseconds ($2.2 \lambda/D$ at 0.7 μm).

- An inner working angle of 1 λ/D to reach the full resolving power of the telescope.

- Either circular or asymmetric dark holes.

- The coronagraph should be able to handle tip-tilt errors within 3 mas.

We designed a phase plate for the SCAR coronagraph that would fit these requirements in Paper I. This SCAR design is able to null a circular area from 0.8 to 2.4 λ/D, which is large enough as Proxima b has a maximal separation of 2.2 λ/D at 0.7 μm. The design bandwidth is 10%. Within this bandwidth the raw contrast is 3×10^{-5}, which is 10 times higher than required. Outside of the design bandwidth it still works well as the contrast stays below 1×10^{-4} up to 20% bandwidth. The bandwidth of the coronagraph is slightly smaller than required. With this design we would be able to reach almost all requirements of the coronagraph for the characterization of Proxima b. The final requirement is necessary as the tip-tilt jitter of SPHERE is 3 mas (Fusco et al., 2016).

It is important to estimate the effects of manufacturing errors which change the reachable contrast. Our target contrast including manufacturing errors is 10^{-4}. There are three major parts that can influence the final performance. The SCAR phase plate is manufactured with the same techniques as the APP. Because the APP has demonstrated on sky that it can achieve a high contrast (Otten et al. (2017)). For the required contrast levels we can safely assume that the manufacturing errors in the phase plate are negligible. The other two aspects are the manufacturing tolerances on the fiber array and the residual wavefront error after the SPHERE AO system. We focussed on the manufacturing tolerances of the fiber injection unit because residual wavefront errors can not be solved by the coronagraph.

5.3.1   Fiber alignment tolerance

To couple well into a single mode fiber it is necessary to have a good alignment of the fiber with respect to the center of the microlens surface. For normal operations of a single mode fiber, which is getting in as much light as possible, the alignment tolerance is already strict. For the fiber coronagraph the alignment tolerance becomes even stricter. In Figure 5.9 the throughput as function of the fiber shift is shown. The figure shows the throughput of the central lenslet (which is the planet coupling) and the throughput on an off-axis lenslet (which is the nulling of the star) as function of fiber offset. The white circle shows the largest fitting circular region where the contrast is still below 10^{-4}. In the same region the on axis relative throughput is above 95 percent. This shows that injecting light into a fiber is easier than using a fiber to cancel the light as the off-axis throughput surface is a much steeper function of misalignment. The white circle has a radius of 1/8 of the mode field diameter of the fiber. The fiber alignment should be within this diameter to reach the required contrast.

Step index single mode fibers are the most used single mode fiber and they have a mode field diameter with a size around 5 μm at a wavelength of 700 nm. Given this size the alignment tolerance would be roughly ± 0.6 μm. This is very strict and most manufacturing procedures have an alignment tolerance of 1 μm. The submicron tolerance can be circumvented with the use of fibers with a larger mode field diameter. Fibers with a large mode field diameter can be made with Photonic Crystal Fibers(PCF). Photonic crystal fibers do not use internal reflection to guide the light as step index fiber do, but use the geometry of the fiber structure. Specific geometric configurations create bandgaps which allows certain optical modes to propagate (Corbett (2006)). Large mode area photonic crystal (LMA) fibers are fibers with a large mode field diameters which can be up to 50 μm (Jansen et al. (2012); Stutzki et al. (2014)) and only allow propagation of the fundamental mode. Another advantage of the PCFs is their endlessly single mode property that allows for a very large wavelength range to be propagated through the fiber, which is convenient for spectrographs. The manufacturing tolerances of 1 μm would require a fiber with a MFD of at least 8 μm. Fibers with a mode field diameter of 12.5 μm are readily available and would fulfill the alignment tolerance requirement. These fibers have a less strict tolerance which is $\approx 1.5\mu$m. With the PCFs the alignment of the fibers should not be an issue, and a manufacturer has been identified.

The LMA fibers have a constant MFD but the numerical aperture (NA) depends on wavelength because of the conservation of etendue. The common step-index fibers have the opposite behaviour: the NA is fairly constant but the MFD changes with wavelength. The microlens launches the light with a constant NA into the fiber, which can lead to a mode-mismatch in the case of LMA fibers. The mode-mismatch reduces the coupling as a function of wavelength and is optimal only for a single wavelength. In Paper I we simulated and designed the phase plates with the LMA fibers in mind. There we saw that the throughput as a function of bandwidth changes very slowly. If the wavelength changes by 50%, the throughput drops from 55% to 40%. Within the design bandwidth of 20% the throughput varies between 50-55%. For our bandwidth this will lead to a slightly lower efficiency compared to step-index fibers.

5.3.2   MLA surface

The microlens array will have surface errors. Therefore it is important to know how much the errors influence the final contrast. The effects of
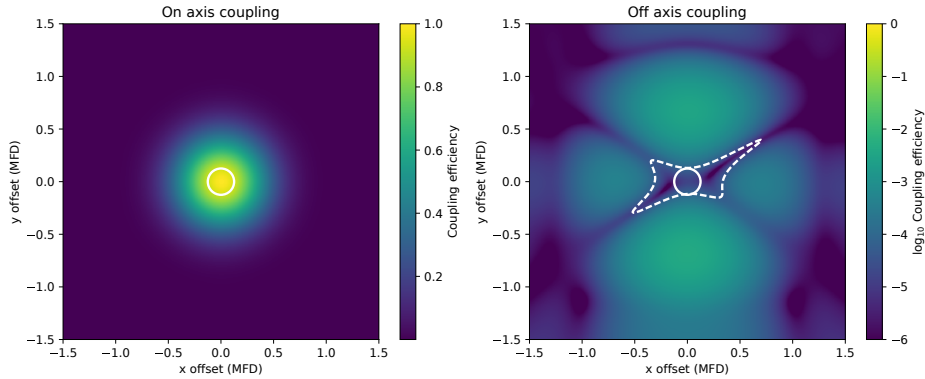
Figure 5.9: Throughput of an on-axis source as function of fiber misalignment is shown on the left. The right shows the off-axis contrast as function of misalignment. The white contour encircles the area where the contrast is below 1×10^{-4}. The white circle is the largest circle that fits within the contour with a radius of 1/8th of the mode field diameter

Zernike wavefront errors on the microlens array are shown in Figure 5.10. For the low order Zernike modes there are two curves per figure which show the contrast for two different fibers. Due to symmetry the other four fibers behave in the same way as one of these two. The most important surface errors are defocus and astigmatism. Both rapidly degrade the contrast. The higher order Zernike modes have almost no influence on the contrast this can be seen in the fourth panel in Figure 5.10. The defocus can be partially compensated by moving the fiber in the axial direction. The astigmatism can not be compensated by changing the alignment of the fibers, so it puts a requirement on the surface deviation of the microlens array. The astigmatism of the microlenses should be smaller than $\lambda/6$ peak to valley to reach the required 10^{-4} contrast.

5.3.3 Fiber mode shape

From our investigations we noticed that the mode profile is not very important. In this analysis we changed the mode radius, eccentricity and the orientation of the resulting multivariate Gaussian mode. The mode field radius can change by $\pm 10\%$ while still create a contrast below 1×10^{-4}. Usual manufacturing constrains on the mode field radius are also within $\pm 10\%$, therefore the mode field radius is not an issue. Eccentricities up to 0.5 and the orientation of the ellipse had no significant impact on the
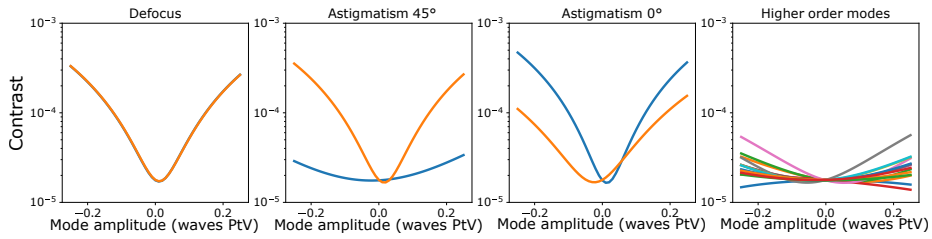
Figure 5.10: Effect of wavefront errors in the microlenses on the contrast due to a certain Zernike mode. The first three panels show the effects on two different fibers. Due to symmetry the other four fibers behave in the same way as these two. The radial symmetry of the defocus mode causes the same effect in all fibers, therefore the curves of the two fibers overlap. In the rightmost panel the effects of Zernike modes 6 to 10 are shown. Focus and astigmatism are the most dominant wavefront errors for lowering the contrast.

throughput and contrast. The average contrast went up from 2.7×10^{-5} to $\approx 3 \times 10^{-5}$ due to these two parameters. From this we conclude that the tolerances on the mode profile of the fiber will be easily met.

5.3.4   FIU Monte Carlo analysis

In the previous section several manufacturing errors have been looked at independently of other errors. A Monte Carlo analysis is performed to estimate the degradation of the coronagraph due to all manufacturing errors. The Monte Carlo analysis generated 3000 realizations of the system within the parameter space given in Table 5.1. The results of this analysis can be seen in Figure 5.11, where the probability density function as function of wavelength and contrast is plotted. The expected performance of the coronagraph plotted on the figure is well under 1×10^{-4}. The three sigma threshold shows that within the manufacturing specifications we will reach the required contrast with very high certainty. The expected stellar nulling within 15% bandwidth is below 3×10^{-5}, within 20% below 1×10^{-4} and within 25% below 2×10^4. After correction for throughput variations this meets the required specifications for characterizing Proxima b with SPHERE+.

Table 5.1: The Monte Carlo parameters for the tolerance analysis. The parameter column shows which parameters are varied and the distribution column shows what distribution is assumed for a parameter.

Parameter	Distribution parameter	Distribution
Mode field diameter	± 5 percent	Uniform
Fiber misalignment	$\pm 1/12$ MFD	Uniform
Microlens focus	$\sigma = 0.01$ percent	Gaussian
Microlens astigmatism	$\sigma = \lambda/4$	Gaussian
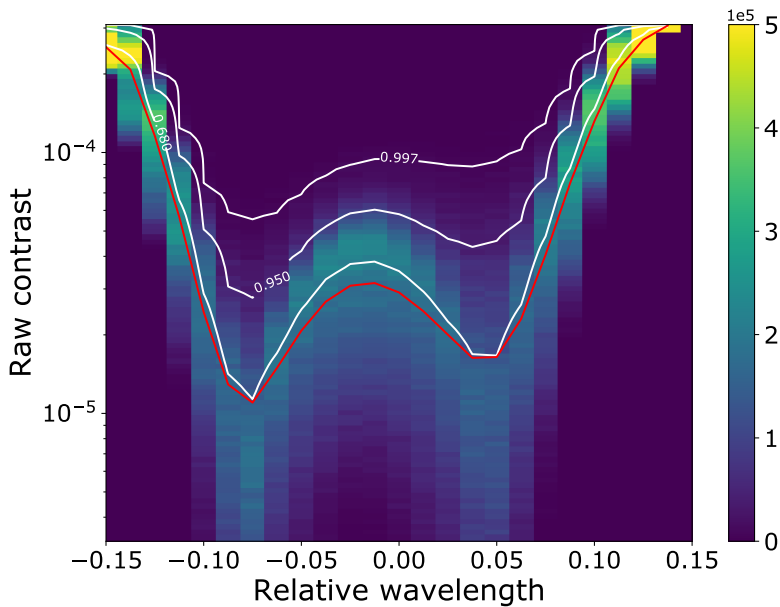
Figure 5.11: Results of the Monte Carlo tolerance analysis as function of wavelength. The red curve shows the expectation value of the contrast. The white curves are the 0.68, 0.95 and 0.997 percentile confidence limits. The analysis indicates that within specified tolerances a contrast below 1×10^{-4} can be reached over a 15 percent bandwidth. Within the full 20 percent bandwidth the contrast is below 2×10^{-4}.

5.4   Conclusions

Combining a pupil plane phase plate with a single mode fiber array creates a new coronagraph that can be used to search for planets very close to their host star. Adding the high-resolution spectroscopy post-processing makes this a very robust system for exoplanet characterization. From the lab measurements and tolerance simulations we can conclude that:

1. We have shown a proof of principle for the SCAR coronagraph in the lab and reached a contrast 1×10^{-4} for the 180 SCAR and $2 - 3 \times 10^{-4}$ for the 360 SCAR. These contrasts limit were due to residual wavefront errors, which requires an active system to remove.

2. The monochromatic tip-tilt stability of the coronagraph has been measured and is estimated to be on the order of $\pm 0.15 \lambda/D$ for both the 360 and 180 design. This agrees with the designed tip-tilt stability and falls within the expected jitter of SPHERE.

3. Within expected manufacturing tolerances the coronagraph will be able to meet the requirements with a high degree of confidence (more than 3σ).

4. The most important aspect of the FIU is the alignment of the fiber with respect to the microlens center according to the tolerance simulations. The tolerance requirement can be achieved by using photonic crystal fibers with large mode field diameters.

With the SCAR coronagraph we meet the requirements for the characterization of Proxima b with SPHERE+ and high-resolution spectroscopy. Due to the simplicity of the optical setup only minor modifications are necessary to accommodate the SCAR coronagraph. Furthermore the single mode fibers simplify the design and decrease the size of the high-resolution integral field spectrograph as the input becomes diffraction limited. Therefore adding the new coronagraphic system as an upgrade to existing HCI instruments at current-generation telescopes will allow characterization of exoplanets in the solar neighborhood. An on-sky prototype is being built as the next step in the development process.

Bibliography

Aime, C., & Soummer, R. 2004, The Astrophysical Journal Letters, 612, L85

Angel, J. R. P., Cheng, A. Y. S., & Woolf, N. J. 1986, Nature, 322, 341, doi: `10.1038/322341a0`

Anglada-Escudé, G., Amado, P. J., Barnes, J., et al. 2016, Nature, 536, 437

Bechter, A., Crass, J., Ketterer, R., et al. 2016, in Proc. SPIE, Vol. 9909, Adaptive Optics Systems V, 99092X

Beuzit, J.-L., Feldt, M., Dohlen, K., et al. 2008, in SPIE Astronomical Telescopes+ Instrumentation, International Society for Optics and Photonics, 701418–701418

Brogi, M., Snellen, I. A., de Kok, R. J., et al. 2012, Nature, 486, 502

Codona, J., Kenworthy, M., Hinz, P., Angel, J., & Woolf, N. 2006, in SPIE Astronomical Telescopes+ Instrumentation, International Society for Optics and Photonics, 62691N–62691N

Corbett, J. C. W. 2006, New A Rev., 50, 305, doi: `10.1016/j.newar.2006.02.028`

Doelman, D. S., Snik, F., Warriner, N. Z., & Escuti, M. J. 2017, in Proc. SPIE, Vol. 10400, Techniques and Instrumentation for Detection of Exoplanets VIII, 10400 – 10400 – 12. `http://dx.doi.org/10.1117/12.2273406`

Fusco, T., Rousset, G., Sauvage, J.-F., et al. 2006, Opt. Express, 14, 7515, doi: `10.1364/OE.14.007515`

Fusco, T., Sauvage, J.-F., Mouillet, D., et al. 2016, in Proc. SPIE, Vol. 9909, Adaptive Optics Systems V, 99090U

Galicher, R., Marois, C., Macintosh, B., et al. 2016, A&A, 594, A63, doi: `10.1051/0004-6361/201527828`

Jansen, F., Stutzki, F., Jauregui, C., Limpert, J., & Tünnermann, A. 2012, Opt. Lett., 37, 4546, doi: `10.1364/OL.37.004546`

Jovanovic, N., Martinache, F., Guyon, O., et al. 2015, Publications of the Astronomical Society of the Pacific, 127, 890

Jovanovic, N., Schwab, C., Guyon, O., et al. 2017, A&A, 604, A122, doi: `10.1051/0004-6361/201630351`

Kawahara, H., Murakami, N., Matsuo, T., & Kotani, T. 2014, The Astrophysical Journal Supplement Series, 212, 27

Konopacky, Q. M., Barman, T. S., Macintosh, B. A., & Marois, C. 2013, Science, 339, 1398, doi: `10.1126/science.1232003`

Labadie, L., Le Coarer, E., Maurand, R., et al. 2007, A&A, 471, 355, doi: `10.1051/0004-6361:20067005`

Lovis, C., Snellen, I., Mouillet, D., et al. 2017, A&A, 599, A16, doi: `10.1051/0004-6361/201629682`

Macintosh, B., Graham, J. R., Ingraham, P., et al. 2014, Proceedings of the National Academy of Sciences, 111, 12661

Martinez, P., Loose, C., Aller Carpentier, E., & Kasper, M. 2012, A&A, 541, A136, doi: `10.1051/0004-6361/201118459`

Mawet, D., Ruane, G., Xuan, W., et al. 2017, The Astrophysical Journal, 838, 92

Miskiewicz, M. N., & Escuti, M. J. 2014, Opt. Express, 22, 12691, doi: `10.1364/OE.22.012691`

Otten, G. P., Snik, F., Kenworthy, M. A., Miskiewicz, M. N., & and, Johanan L. Codona, M. J. E. 2014, in Proc. SPIE, Vol. 9151, 9151 – 9151 – 10. `https:`

`//doi.org/10.1117/12.2056096`

Otten, G. P., Snik, F., Kenworthy, M. A., et al. 2017, The Astrophysical Journal, 834, 175

Por, E. H., & Haffert, S. Y. 2017, Astronomy & Astrophysics, submitted (not yet accepted)

Riaud, P., & Schneider, J. 2007, A&A, 469, 355, doi: `10.1051/0004-6361:20077085`

Shaklan, S., & Roddier, F. 1988, Appl. Opt., 27, 2334, doi: `10.1364/AO.27.002334`

Snellen, I., de Kok, R., Birkby, J., et al. 2015, Astronomy & Astrophysics, 576, A59

Snellen, I. A., Brandl, B. R., de Kok, R. J., et al. 2014, Nature, 509, 63

Snik, F., Otten, G., Kenworthy, M., et al. 2012, in Proc. SPIE, Vol. 8450, Modern Technologies in Space- and Ground-based Telescopes and Instrumentation II, 84500M

Sparks, W. B., & Ford, H. C. 2002, The Astrophysical Journal, 578, 543

Stutzki, F., Jansen, F., Otto, H.-J., et al. 2014, Optica, 1, 233, doi: `10.1364/OPTICA.1.000233`

Vérinaud, C., Le Louarn, M., Korkiakoski, V., & Carbillet, M. 2005, MNRAS, 357, L26, doi: `10.1111/j.1745-3933.2005.08638.x`

Wang, J., Mawet, D., Ruane, G., Hu, R., & Benneke, B. 2017, AJ, 153, 183, doi: `10.3847/1538-3881/aa6474`

6 | Two accreting protoplanets around the young star PDS 70

Adapted from
S. Y. Haffert, A. J. Bohn, J. de Boer, I. A. G. Snellen, J.
Brinchmann, J. H. Girard, C. U. Keller and R. Bacon
Nature Astronomy (2019)

Newly forming proto-planets are expected to create cavities and sub-structures in young, gas-rich proto-planetary disks (Dodson-Robinson & Salyk, 2011; Kley & Nelson, 2012; Zhu et al., 2011), but they are difficult to detect as they could be confused with disk features affected by advanced image-analysis techniques (Huélamo et al., 2018; Rameau et al., 2017). Recently, a planet was discovered inside the gap of the transitional disk of the T-Tauri star PDS 70 (Keppler et al., 2018; Müller et al., 2018). Here we report on the detection of strong H-alpha emission from two distinct locations in the PDS 70 system, one corresponding to the previously discovered planet PDS 70 b, which confirms the earlier Hα detection (Wagner et al., 2018), and another located close to the outer-edge of the gap, coinciding with a previously identified bright dust spot in the disk and with a small opening in a ring of molecular emission(Keppler et al., 2018; Long et al., 2018; Müller et al., 2018). We identify this second Hα peak as a second proto-planet in the PDS 70 system. The Hα emission spectra of both proto-planets indicate ongoing accretion onto the proto-planets(Natta et al., 2004; Rigliaco et al., 2012), which appear to be near a 2:1 mean motion resonance. Our observations show that adaptive-optics-assisted, medium-resolution, integral-field spectroscopy with MUSE (Bacon et al., 2010) targeting accretion signatures will be a powerful way to trace ongoing planet formation in transitional disks at different stages of their evolution. Finding more young planetary systems in mean motion resonance would give credibility to the Grand Tack hypothesis in which Jupiter and Saturn migrated in a resonance orbit during the early formation period of our Solar System (Walsh et al., 2011).

6.1   Content

PDS 70 (V* V1032 Cen) is a young T-tauri star at a distance of 113.43±0.52 pc (Gaia Collaboration et al., 2016, 2018) with a spectroscopically determined age of 5.4±1.0 Myr (Müller et al., 2018). Its proto-planetary disk was first discovered through spectral energy distribution(SED) modelling (Gregorio-Hetem & Hetem, 2002), and later directly imaged at near-infrared and sub-mm wavelengths (Hashimoto et al., 2012, 2015; Long et al., 2018). Both the SED modelling and direct imaging show that PDS 70 harbours a transitional disk in which a large radial region from 20 AU – 40 AU (Hashimoto et al., 2015; Keppler et al., 2018), as seen in the near-infrared, is cleared of dust. The gap is found to be larger at sub-mm wavelengths (Hashimoto et al., 2015; Keppler et al., 2018), indicating that there is a radial segregation of dust grains possibly generated by a radial pressure gradient in the disk. A potential mechanism for such a pressure bump is the dynamical clearing of the disk by the planetary-mass companion PDS 70 b (Pinilla et al., 2012a,b). PDS 70 b is estimated to be a 4-17 $M_{\rm J}$ planet at a projected angular separation of 195 milli-arcseconds (22 AU) and position angle of about 155°. Follow-up imaging observations with MagAO on the Magellan 6.5m telescope revealed a tentative 4σ Hydrogen α(Hα) emission signal (Wagner et al., 2018). Hα emission is commonly associated with accretion (Natta et al., 2004; Rigliaco et al., 2012) and therefore indicates that PDS 70 b is still in formation.

The PDS 70 system was observed with the Multi Unit Spectroscopic Explorer (MUSE) (Bacon et al., 2010) at ESO's Very Large Telescope (VLT) in the Laser Tomography Adaptive Optics (LTAO) assisted narrow-field mode during the commissioning night of 20 June 2018. MUSE is an optical, medium-resolution, integral-field spectrograph that covers 480-930nm at a spectral resolving power ranging from $\lambda/\Delta\lambda = 1740$ in the blue to 3450 in the red, targeting several important accretion tracing emission lines including Hα at λ=656.28 nm. We processed the data by applying a high-resolution Spectral Differential Imaging (HRSDI) technique, in which a scaled, continuum-normalized stellar spectrum is subtracted from the data at each spatial pixel (spaxel) position, and further residuals in the spectrum of each spaxel are removed using a principle component analysis (see Methods for a detailed description). HRSDI is only sensitive to sharp spectral features, such as spectral lines, because the continuum-normalization step removes all differential broadband features between different spaxels. Excess continuum light from starlight that is reflected by the disk around PDS

70 and the continuum of potential planets is also removed. With HRSDI we can side-step the common issues that conventional high-contrast imaging techniques like Angular Differential Imaging(ADI) have, where the spatial information is used to build up a stellar reference. Such techniques are sensitive to the spatial structure of the source and can generate artifacts that look like a planet (Huélamo et al., 2018; Rameau et al., 2017).

Using HRSDI we detect a strong Hα emission line at two distinct locations in the PDS 70 system (Figure 6.1, left panel), with a 11σ source at the position of PDS 70 b, and a second, 8σ source detected at 240 mas away from the host star at a position angle of 283°. The former detection is an independent confirmation of the earlier observations of PDS 70 b (Keppler et al., 2018; Müller et al., 2018; Wagner et al., 2018). The latter source coincides with a previously identified bright spot in 2.1 and 3.8-μm broadband images (Keppler et al., 2018), which is confirmed by our re-analysis of the 2.1 and 3.8 μm data from SPHERE and NACO at the VLT (Figure 6.2, middle and right panel).

Gaussian profiles fitted to the extracted emission spectra (see Figure 1) show that the Hα lines from both PDS 70 b and the other source are red-shifted with respect to the stellar Hα emission. This line-of-sight shift is measured with respect to the stellar Hα line before the removal of the starlight; every spaxel is therefore self-calibrated. The Hα line-of-sight redshift for PDS 70 b is 25 +- 8 km s-1, and 30 +- 9 km s-1 for the second source. The full width at half maximum (FWHM) of the two emission lines are 123 +- 13 km s-1 and 102 +- 19 km s-1 for PDS 70 b and the other source, respectively. These lines are significantly narrower than the stellar line, which has a width of 147 +- 5 km s-1. A third difference between the emission lines are their shapes. The Hα line of the star exhibits an inverse P Cygni profile with a blue-shifted emission and a red-shifted absorption component, which is quite common and a sign of magnetospheric accretion (Edwards et al., 1994; Reipurth et al., 1996). The Hα line profile from PDS 70 b and the other source do not exhibit these features, and show just a single Gaussian-like profile.

The fact that the line shape, velocity offset, and the line widths differ from what is expected from reflected star-light excludes reflected light as the origin and indicates that the line emission is locally generated. The multi-epoch astrometry (see Table 1) of the new point source reveals that it orbits in the direction of the Keplerian rotation of the circumstellar disk and is co-moving with its host star, which makes it improbable to be a background object. We therefore identify this second source of Hα emission as the
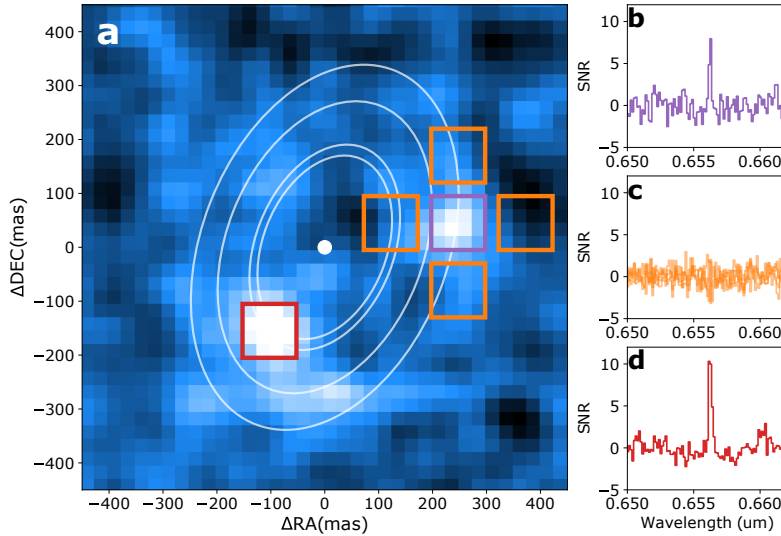
Figure 6.1: Overview of the PDS 70 system. a, The Hα detection map with an overlay of the contours of the orbital radii and a white dot in the center that marks the position of the star. The contours for PDS 70 c are the minimum and maximum orbital radii found for the different wavelength observations. For both objects the square apertures that were used for the photometry are shown, with the red aperture for PDS 70 b and the purple aperture for PDS 70 c. b, c, d, The corresponding spectra divided by their standard deviation are on the right and centered around the Hα line position. The four apertures in orange indicate reference areas that are used to compare with PDS 70 c. The orange reference spectra on the right do not show any spectral feature, while both PDS 70 b and c clearly show Hα in emission.
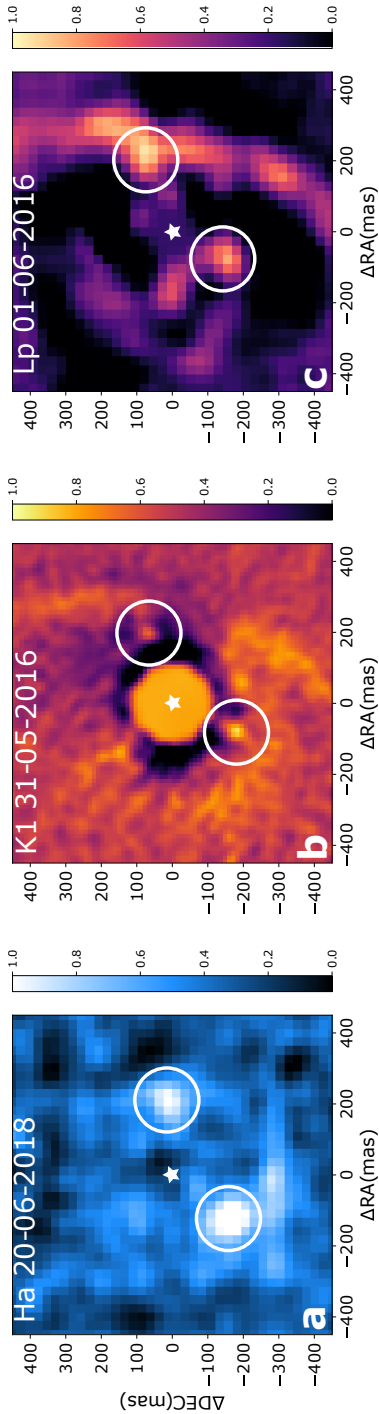
Figure 6.2: Multi-epoch detection of PDS 70 b and c. a, The Hα detection map of PDS 70 after removal of all direct and scattered starlight. PDS 70 b and c have their position marked with white circles. The white star in the middle shows the position of the star. The feature just south of PDS 70 b is most likely caused by image slicing and field splitting axis and we do not see it in the other datasets. b, The K1-band observations of PDS 70 with SPHERE/IRDIS after Angular Differential Imaging processing. Both companions, with their positions marked by the white circles, are recovered in the data. The position of the star is marked by the white star in the center. C, NACO observations in L-band. PDS 70 b is clearly visible, while PDS 70 c is connected to the disk. This is due to the large full width half maximum of the PSF in L-band. The disk should be a smooth ring according to previous research, the extension at the position of PDS 70 c is therefore most likely due to the planet itself. The position of the star is marked by the white star in the center.

location of a second, forming planet, PDS 70 c. The significant difference between the line-of-sight radial velocity of Hα emission from the accreting proto-planets compared to their Keplerian velocities, 4.3 km s-1 and 3.4 km s-1 for PDS 70 b and c, indicates that the dynamics of planetary accretion are different from the orbital dynamics of the planets. This is also the case for accreting stars, where the line-of-sight velocity of the accreting material is different from the system velocity.

The K-L color and non-detection in H-band imply that PDS 70 c is redder than PDS 70 b, which could be either due to a lower temperature and mass or due to obscuration by dust from the disk. Comparing the K-L color of PDS 70 c to evolutionary models indicates that the planet has a mass within the range of 4-12 MJ after having included possible biases from the circumstellar disk and extinction (see Methods section). There is a high likelihood that the estimated mass of the companion, even by including some of the biases, is overestimated due to possible other structures around the planet (see Figure 6.3) like additional scattered star light, a circumplanetary disk or potential streamers that connect the planet to the circumstellar disk. Detailed hydrodynamical modelling of the system may put a better constraint on the planet masses.

We estimated the mass accretion rates of both companions using an empirical relation between the Hα 10-percent width, which is the full width at 10-percent of the maximum, and the mass accretion rate (Natta et al., 2004; Rigliaco et al., 2012). The derived 10-percent widths are 224+-24 km s-1 and 186+-35 km s-1 for planets b and c, which indicate a mass accretion rate of 2x10-8+-0.4 MJ yr-1 for b and 1x10-8+-0.4 MJ yr-1 for c. The combined mass accretion rates of the planets are comparable to the stellar accretion rate, which is 5.5x10-8+-0.4 MJ yr-1. A previous estimate of the accretion rate of planet b, based on Hα the luminosity (Wagner et al., 2018), estimated the mass accretion of PDS 70 b to be 1x10-8+-1 MJ yr-1. The estimate of (Wagner et al., 2018) based on the absolute Hα luminosity needs to take the extinction into account, which was chosen as 3.0 magnitudes to include the effects of a possible circum-planetary disk and the extinction by the circum-stellar disk. Their measurement is consistent with the low accretion rate found here, which is not affected by extinction as it is based on the width of the Hα line instead of the luminosity. At the current accretion rate, it would take 50-100 Myr to form Jupiter-mass planets, which is much longer than the typical disk lifetime of 10 Myr. The accretion rates of young stars are significantly decreasing near the end of their formation when they exhibit episodic accretion bursts (Armitage
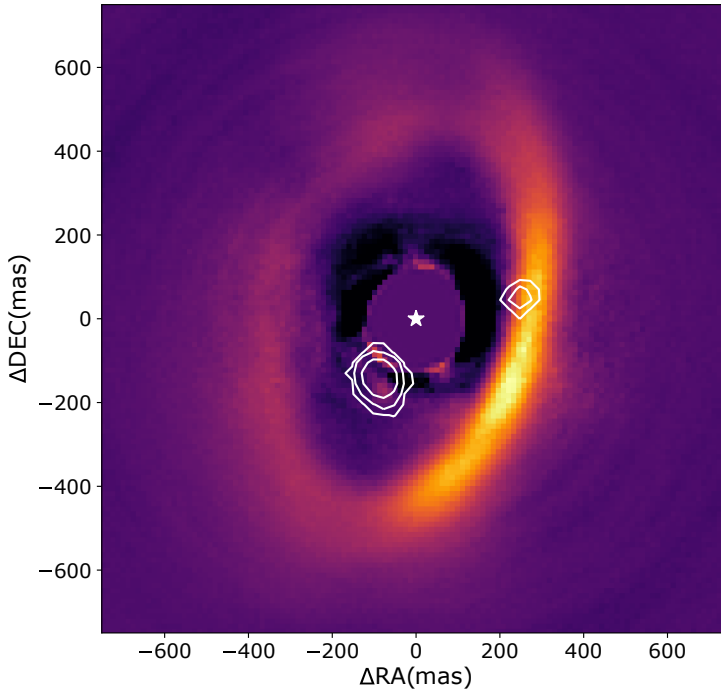
Figure 6.3: Composite image of the proto-planetary disk and the two companions. The disk image from SPHERE H-band observations is overlaid with the contours of the Hα emission of the two planets to indicate their positions in the disk. The disk features a smooth outer disk and a perturbed inner disk. The darker features around the inner disk are due to over-subtraction of the inner-disk by the post-processing algorithm. The planets are clearing out the large gap between the outer and inner disk edges, which can be seen in the scattered light image. The outer planet is partially obscured by the outer disk.

et al., 2001). A similar scenario of long-term variable accretion might apply to the planets in this system. Short term variability is due the accreting gas dynamics, which for example could be a rotating hotspot on the planet surface or an orbiting accretion funnel from the circum-planetary disk.

Based on the wide gap in the disk and the low accretion rate of the star, PDS 70 was already predicted to contain a multi-planet system (Hashimoto et al., 2015) where the planets block the mass flow towards the star. Hydro-dynamical modelling of viscous disks suggests that a single, massive planet is only able to open a small gap (¡15 AU) (Kley & Nelson, 2012; Zhu et al., 2011). In contrast, multi-planet systems are thought to be able to carve large gaps in disks with azimuthal asymmetries (Dodson-Robinson & Salyk, 2011; Zhu et al., 2011), where the gap width is governed by the dynamical and viscous time scales of the disk. Detailed hydrodynamical modelling will be necessary to constrain the disk-planet interaction of the PDS 70 system. Another indication of a planet at a larger orbital distance came from the 870-μm ALMA observation of the HCO+ molecule that shows a hole in the disk structure, while the dust continuum does not show this (Long et al., 2018). We suspect that this is caused by PDS 70 c since the location of the hole and PDS 70 c coincide.

Assuming that the orbits of the planets and the disk are coplanar (at an inclination of 49.7o (Hashimoto et al., 2015)), angular separations to the host star imply orbital distances for PDS 70 b and c of 20.6±1.2 AU (consistent within the 1σ uncertainties of earlier measurements (Keppler et al., 2018; Müller et al., 2018)) and 34.5±2 AU, respectively, suggesting that the planets are in or near a 2:1 mean motion resonance if the orbits are circular. Mean motion resonance migration is proposed as an early orbital evolution scenario for massive gas giant planets (Xu et al., 2018). During a migration-II scenario, in which planets are massive enough to carve a gap in the disk, the inward migration speed depends inversely on the mass of the planet (Nelson et al., 2000). If the inner planet is more massive than the outer, the latter will migrate towards the inner planet until it is captured in resonance, locking their relative orbits (Kley et al., 2004). A specific version of such an orbital evolution scenario is suggested for the gas giant planets in the early solar system as the Grand Tack Hypothesis (Walsh et al., 2011). While the most massive planet Jupiter was formed first and was migrating towards the young Sun, the formation and subsequent faster inward migration of Saturn locked the two planets in a 3:2 mean motion resonance. This is thought to have reversed their, now coupled, migration direction outward towards their current orbits. Finding other systems,

like PDS 70, in mean-motion resonance lends credibility to this formation scenario for our solar system.

The observations with MUSE show that adaptive-optics assisted, medium-resolution, integral-field spectrographs are highly efficient instruments to observe accretion emission spectra from planets in formation. We suspect that more accreting planets could be found and characterized in transition disks with this technique. Another exciting opportunity, which is now possible due to the high efficiency of both the HRSDI data processing technique and MUSE, is the detailed investigation of accretion on short and long time scales. This will shed light on the variability of planetary accretion and will lead to a better understanding of the formation of planets, allowing us to infer the formation history of the solar system.

6.2   Methods

6.2.1   VLT/MUSE observations and data reduction.

The PDS 70 system was observed during the commissioning run of the adaptive optics assisted MUSE narrow-field mode in June 2018. MUSE is a medium resolution integral field spectrograph (IFS), which acquires a spectrum for every spatial pixel in a continuous field of view of 7.5"x7.5" (Bacon et al., 2010). It is coupled with GALACSI, the advanced laser tomography adaptive optics system of the VLT Adaptive Optics Facility (Madec et al., 2018; Oberti et al., 2016), which was also used during the observations of PDS 70. PDS 70 itself was used as the low-order tip-tilt star. The observations were split into six individual exposures of 300 seconds each in field stabilizing mode with a total of 1800 seconds on target. Between each observation the field of view was rotated by 90 degrees. This was done to reduce the impact of possible bad pixels, reduce flatfield errors and improve the sampling of the line spread function. Each observation was processed with version of 2.4 of the MUSE pipeline which is available through ESO's web pages (Weilbacher et al., 2014). The pipeline performs background subtraction, flat fielding for non-uniform pixel response, spectral extraction and the wavelength calibration. Spatial offsets between the individual exposures were determined manually by finding the centroid position of the star. After the extraction the individual data cubes were stacked to create the combined data cube from all observations.

6.2.2   High-resolution spectral differential imaging (HRSDI).

We subtracted a reference stellar spectrum from every spatial pixel to find
the faint companions. A stellar model could in principle be used to sub-
tract out the star, but this will leave strong residuals either due to intrinsic
variability of the host star or due to uncalibrated instrumental effects. We
therefore used a data-driven approach to create the reference spectrum,
similar to the approach that was used for the characterization of Beta Pic-
toris b (Hoeijmakers et al., 2018). The changes in the spectrum between
spatial pixels can be separated into two parts, low-order effects and high-
order effects. The low-order effects change the continuum profile, while
the high-order effects change the spectral lines. To calibrate the low-order
effects, we first normalized all spectra by their total flux and created a ref-
erence spectrum by taking the median over all spatial pixels. The median
is a robust estimator for the mean in the presence of outliers. As the exo-
planets are only present in a few spatial pixels, the median will lower the
influence of the planet spectra on the reference spectrum. The spectrum
for each individual spatial pixel is then divided by this reference spectrum.
Assuming that no high-order effects are present, we will be left with a dif-
ferential low order continuum signal. This residual is low-passed filtered by
applying a first-order Savitzky-Golay filter with a window width of 101 pix-
els (126.25 ANG). Each spectrum is divided by its low-passed differential
continuum to correct for the low order residuals. The high-order residu-
als are due to several instrumental effects, such as a changing wavelength
calibration or a changing resolving power across the field. Because MUSE
is an IFS with 310 by 310 spatial pixels, we acquired many realizations
of the high-order instrumental effects. We used these to build a reference
library through principle component analysis (PCA). Each PCA compo-
nent will remove different correlated residuals. PCA was applied over the
spectral direction where the first few components corrected for differential
wavelength solutions and the subsequent components mainly correct re-
gions that are strongly contaminated by telluric absorption (Oxygen A and
B bands). We found the optimum number of components to subtract to
be 5 by maximizing the signal-to-noise of PDS 70 b. Only after subtract-
ing on the order of 20 components did the signal from PDS 70 b start to
decrease. The HRSDI method is only sensitive to sharp spectral features,
such as spectral lines, because the continuum-normalization step removes
all differential broadband features between different spaxels. Excess con-
tinuum light from starlight that is reflected by the disk around PDS 70
and the continuum of potential planets is also removed. With HRSDI we

can side-step the common issues that conventional high-contrast imaging techniques like Angular Differential Imaging(ADI) have where the spatial information is used to build up a stellar reference. Such techniques are sensitive to spatial structure of the source and can generate features that look like a planet[9,10].

6.2.3 Aperture photometry of both companions and SNR determination.

We estimated the relative flux by applying aperture photometry to every wavelength channel. Square apertures of 100 by 100 milli-arcseconds (4 by 4 pixels) were chosen because the MUSE PSF during the observations had a full width half maximum of 60-80 milliarcseconds at 656 nm. No background correction for the aperture photometry was necessary as this was already done during the pre-processing. A major concern for high-contrast image processing techniques is the subtraction of the planet signal during the post-processing, which will lead to strongly biased photometry of the companions (Pueyo, 2016). We injected fake sources into the dataset to determine how much the HRSDI method would influence the photometry. The recovered signals of the fake sources were within a few percent of the injected signal, indicating that the HRSDI did not influence the photometry. We estimated the error in the photometry by taking the standard deviation along the spectral direction for each region. The extracted one-dimensional spectra were sub-sequentially used to fit spectra line profiles with the Markov chain Monte Carlo(MCMC) sampler emcee (Foreman-Mackey et al., 2013). The Hα emission line was modelled by a Gaussian line profile on top of a constant continuum. To determine the radial velocity reference we fitted a PHOENIX model with an effective temperature of 4000 K and a log(g) of 4.5 (Keppler et al., 2018) at the same spatial positions but before removing the star. From these two measurements we could determine the relative radial velocity of the planets. The uncertainties of the measurements were derived from the posterior distributions from the MCMC procedure (see Supplementary Figures 1 and 2). The ratio between the line flux of the planets compared to the stellar continuum around the Hα line was used to define the contrast ratio.

6.2.4 Astrometry of the Hα emission from PDS 70 b and c.

We fitted a Moffat profile to the cleaned Hα data cubes. The initial starting point of the fitting procedure was estimated from the Hα image. We used
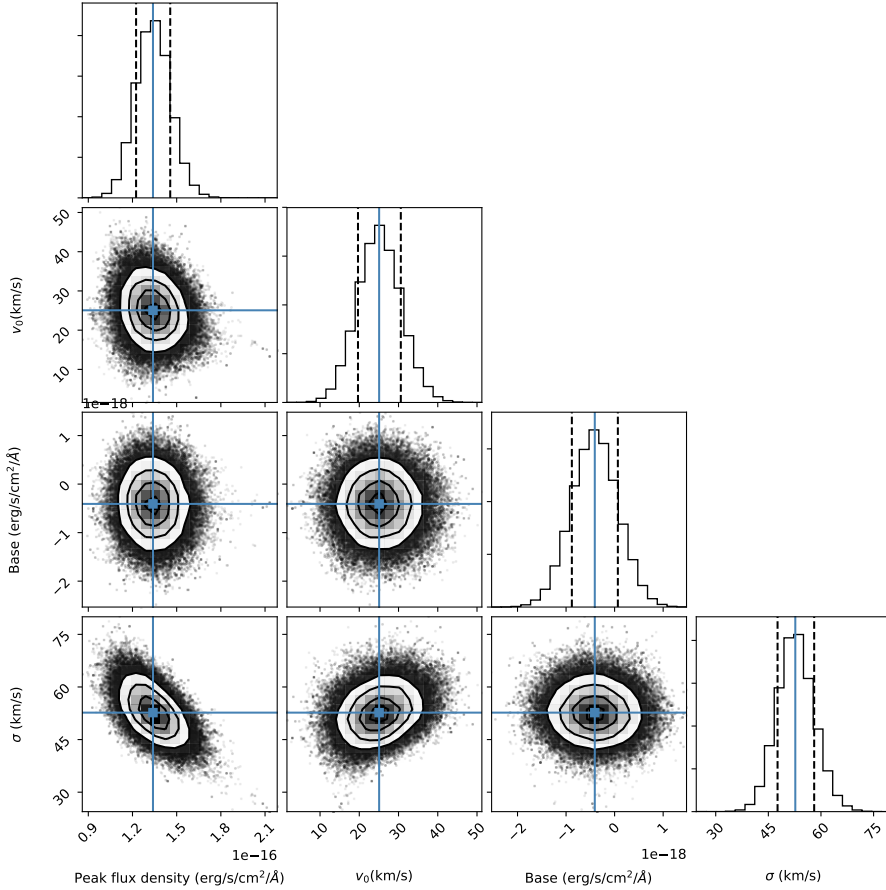
Figure 6.4: Corner plots of the Gaussian spectral line fitting of PDS 70 b. The peak flux and baseline are in flux density units of ergs/s/cm^2/$\mathring{A}$. Both the radial velocity (v_0) and the width (σ) are in units of kms$^-$1. The radial velocity of the planet has not yet been corrected for the systematic radial velocity. From the amplitude measurement we can estimate that the detection has an 11σ significance.

Figure 6.5: Corner plots showing the posterior distributions from emcee for the Gaussian spectral line fitting of PDS 70 c. The peak flux and baseline are in flux density units of ergs/s/cm^2/$\mathring{A}$. Both the radial velocity (v_0) and the width (σ) are in units of kms^{-}1. The radial velocity of the planet has not yet been corrected for the systematic radial velocity. From the amplitude measurement we can estimate that the detection has an 8σ significance.
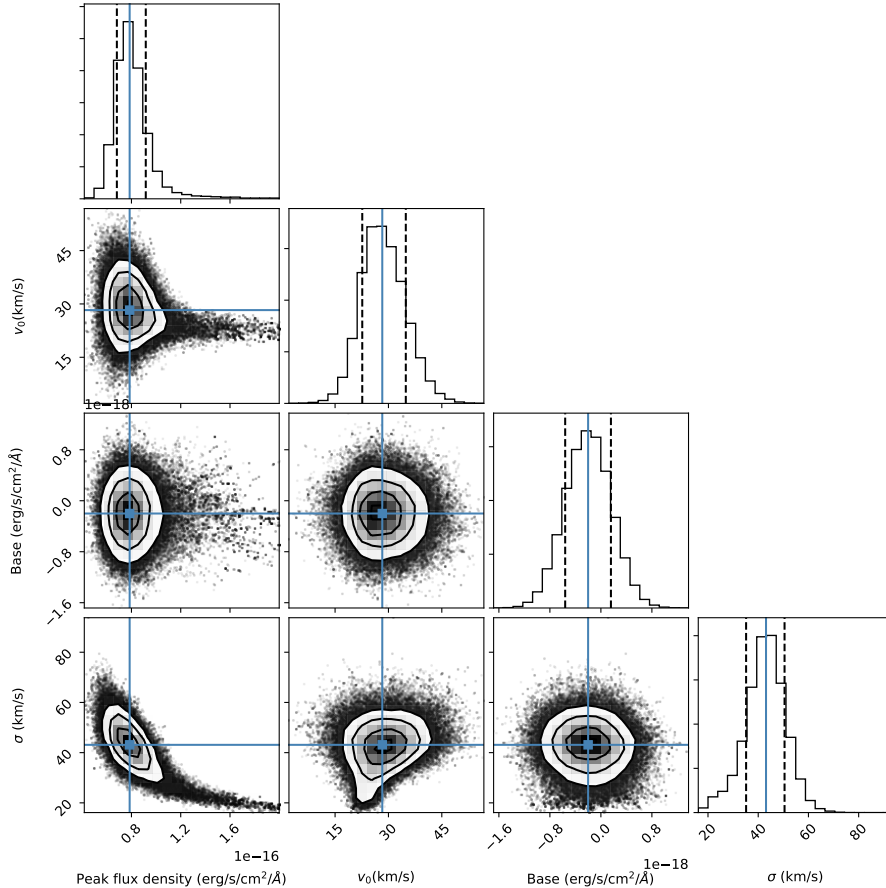
a least-squares approach to fit the astrometry, and we estimated the errors by analyzing the covariance matrix around the optimal χ^2 value. The retrieved error bars from the least-square method were less than one pixels. This is not realistic because the PSF of MUSE is not Nyquist-sampled by the image slicer, and the image slicer causes strong diffraction effects when part of the light hits an edge of any of the slicer mirrors. The effects becomes more apparent when the AO is delivering higher quality images. This makes it difficult to achieve sub-pixel astrometry without a good PSF model, and we therefore used the size of a single spatial pixel as the astrometric uncertainty. We verified the astrometric solution with a background star that was in the field-of-view. This star is roughly 2.3 arcseconds to the north. We can use the astrometric measurements of GAIA (Gaia Collaboration et al., 2016, 2018), because PDS 70 and the background star were observed with GAIA. After correction for the proper motion of the two stars, we measure a 0.3 percent difference in the angular separation of the two stars between GAIA and MUSE and a 0.76 degree offset from true north. Using the astrometry points from the SPHERE/NACO and MUSE observations we exclude both planets as background objects (See Figure 6.6).

6.2.5   Orbit radius and mean motion resonance estimation.

While the L and K-band data were taken on different nights, they are too close in time (1 night apart) to count as different epochs. A minimum of 3 epochs are necessary to fit all parameters of a Keplerian orbit, and we only have two ($H\alpha$ and K+L-band). Under the assumption of co-planarity with the protoplanetary disk and a circular Keplerian orbit, we determined the orbital radius for both companions. We used earlier measurements of the disk inclination and position angle, which are 49.7° and 158.6° respectively (Hashimoto et al., 2012, 2015), to deproject the apparent positions of the planets onto the circumstellar disk plane. After the deprojection we used a weighted mean to calculate the orbital radius for both planets. With the orbital radii and under the assumption of Keplerian motion we measured the ratio of the orbital periods to be 2.0±0.15, 2.5±0.25 and 2.6±0.75 for the K-band, L-band and $H\alpha$. In L-band the astrometry is biased to longer orbital radii, due to the close proximity of PDS 70 c to the disk. The measurements suggest a mean motion resonance close to 2:1. To account for the astrometric errors we used a parametric bootstrap method, with a Gaussian error model to estimate the probability distribution of the period ratio (see Figure 6.7).
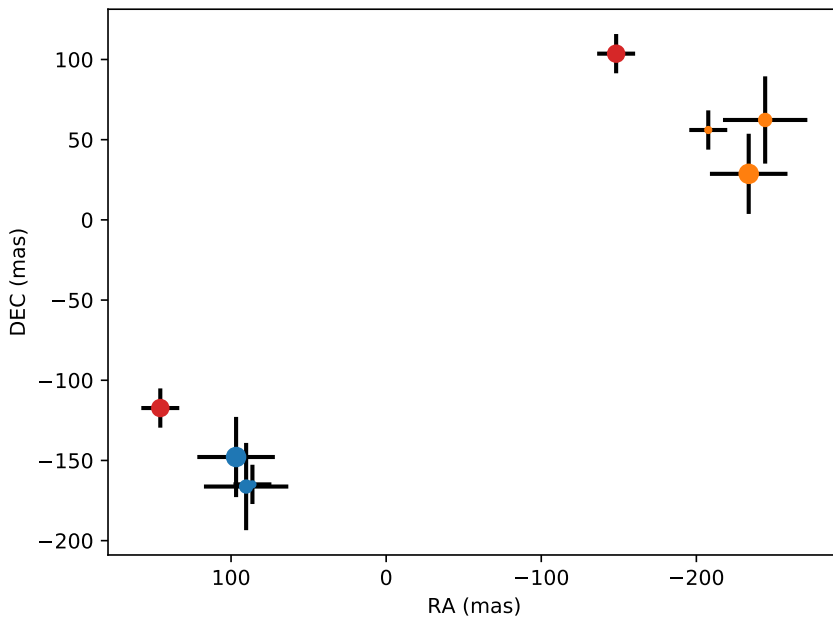
Figure 6.6: The projected motion for a background object. The points in blue indicate the measured astrometry for PDS 70 b, and the orange points are the astrometry measurements for PDS 70 c. The red dots show the positions if both companions were background objects. The K-band detection was taken as the reference position and epoch. The epoch difference between K-band and Hα is 2 years.
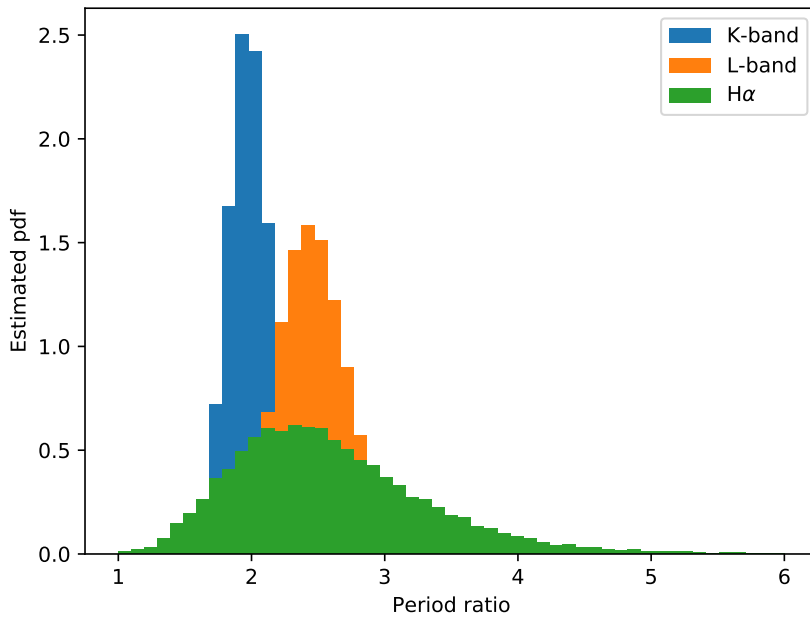
Figure 6.7: The bootstrapped probability density function of the period ratio between planet b and c. The K-band and Hα measurements suggest a peak close to a period ratio of 2. The L-band data is biased to longer periods due to the astrometric bias from the entanglement with the scatter light from the disk. We conclude that a mean motion resonance orbit of 2:1 is likely and well within the error margins.

6.2.6   SPHERE and NACO archival data reduction.

We obtained three archival datasets on PDS 70 including raw calibration files from the ESO archive: (i) Coronagraphic SPHERE/IRDIS data (PI: Beuzit, ESO ID: 095.C-0298(A)) taken with the H23 dual-band filter combination (Vigan et al., 2010), (ii) non-coronagraphic SPHERE/IRDIS (PI: Matter, ESO ID: 097.C-1001(A)) data taken with the K12 dual-band filter combination, and (iii) non-coronagraphic NACO L' data (PI: Launhardt, ESO ID: 097.C-0206(A)).

The data reduction was performed with our own image processing pipeline, which is based on the new release of the PynPoint package (Stolker et al., 2019). This includes basic steps such as dark subtraction, flat-fielding, and correction of bad detector pixels with a 5 σ box filtering algorithm. The NACO data were obtained with a dither pattern, placing the star at three offset positions on the detector. Because one quadrant of the detector showed strong, non-static readout artefacts, we discarded every third cube of the NACO data. For the SPHERE data, we performed the subtraction of the sky and instrumental background using the additional images taken at an offset sky position without any source. Due to the large offsets between the NACO dither positions, we subtracted the thermal background from the science images themselves. We defined regions of interest around the star for each of the two dither positions and obtained a stack of science frames and background frames for each of the two positions. Then, we modelled and subtracted the background in each science frame with an approach based on PCA of the corresponding background stack as described in (Hunziker et al., 2018). Afterwards, the resulting background-subtracted science frames were merged again.

Both SPHERE data in K1-band and NACO data were obtained without a coronagraph and without saturating the detector. Therefore, we were able to center the frames on PDS 70 with a two-dimensional Gaussian fit. The SPHERE data in the H2- band was obtained with an apodized-pupil Lyot coronagraph (Marois et al., 2006) in place. To center the science images, we made use of the center frames that were taken alongside the science observations. For these frames, a sinusoidal shape was applied to the deformable mirror to create four calibration spots around the star's position behind the coronagraph. These spots were used for the centering procedure, following the instructions in the SPHERE manual.

To detect and to reject bad science frames, we measured the flux inside circular apertures with a radius of 3 FWHMs of the instrumental PSF around the star for the non-coronagraphic data. For the coronagraphic

data, we used circular annuli around the coronagraphic mask with inner and outer radii of 100 mas and 160 mas instead. Finally, we discarded all frames deviating from the average aperture flux by more than 3 sigma. After this pre-processing, 60, 672, and 12346 centred images remained for SPHERE H23-, SPHERE K12-, and NACO L', respectively.

Since the data were taken in pupil-stabilized mode, a PSF subtraction based on angular differential imaging (Amara & Quanz, 2012) in combination with PCA (Soummer, 2005) was applied. To model the stellar PSF, we fitted 1 and 20 principal components for SPHERE K12 and NACO data, respectively. The number of fitted components were optimised in order to maximise the signal-to-noise ratio of PDS 70 b.

Because ADI-based algorithms tend to produce unphysical residuals when applying them to extended structures such as disks (Choquet et al., 2014), we used an approach based on reference star differential imaging (RDI, (Smith & Terrile, 1984)) in combination with PCA to reduce the coronagraphic SPHERE data instead. We chose the K9IVe-star TYC 7433-1102-1 as a reference, which was observed during the same night (2015-05-03) with the exact same observational setup (PI: Beuzit, ESO ID: 095.C-0298) as the data on PDS 70. The pre-processing was performed analogously to the reduction of the coronagraphic SPHERE data described above. After frame rejection, we were left with 63 centred reference images. These were analysed with respect to their principal components and 5 components were fitted to the pre-processed science images of PDS 70 to model the stellar halo and the instrumental artefacts. The PSF models were subtracted from the science images, the residual frames were rotated such that north is up and east is left, and the remaining stack was median combined. We optimised the number of fitted principal components to maximise the signal-to noise ratio of the disk around PDS 70 in the final image.

6.2.7   Astrometry and photometry extraction of PDS 70 b and c from NACO and SPHERE data.

The astrometry and photometry of each companion were extracted simultaneously by injecting artificial fake companions using the SimplexMinimizationModule of the new PynPoint release (Soummer, 2005). For the astrometric extraction we use plate scales and true north corrections provided by (Rigliaco et al., 2012) for the corresponding datasets. We used the PSF of PDS 70 as a template for the artificial companions and minimized the curvature in the residual image around the planets' positions within

a circular aperture with a radius of 80 mas. To explore the correlation between astrometric and photometric extraction of the companions and to assess the statistical uncertainties of this optimisation, we performed an MCMC sampling using the MCMCSamplingModule of PynPoint. We used 100 walkers and 200 steps. We excluded the first 20 steps of the chains as the burn-in to the sampling. The presented lower and upper uncertainties represent the 16th and 84th percentiles of the samples, which coincides with 1-σ confidence levels in the case of a Gaussian posterior distribution.

6.2.8   Mass determination of PDS 70 c.

The mass of the second companion was estimated by comparing the K-L color and the absolute L magnitude to evolutionary models (Allard et al., 2001). To include possible effects of extinction by a circum-planetary disk or the circum-stellar disk, we varied the extinction between 0 and 3 magnitudes. Another strong bias comes from the blending of the circum-stellar disk and the planet in the L-band observations. To estimate this blending we added a conservative 0 to 3 magnitudes to the measured the L-band magnitude to include possible blending effects of the disk. The resulting region in the color-magnitude diagram was overlapping with the 4-12 M_J mass range for the evolutionary model.

Bibliography

Allard, F., Hauschildt, P. H., Alexander, D. R., Tamanai, A., & Schweitzer, A. 2001, ApJ, 556, 357, doi: 10.1086/321547

Amara, A., & Quanz, S. P. 2012, MNRAS, 427, 948, doi: 10.1111/j.1365-2966.2012.21918.x

Armitage, P. J., Livio, M., & Pringle, J. E. 2001, MNRAS, 324, 705, doi: 10.1046/j.1365-8711.2001.04356.x

Bacon, R., Accardo, M., Adjali, L., et al. 2010, in Society of Photo-Optical Instrumentation Engineers (SPIE) Conference Series, Vol. 7735, Proc. SPIE, 773508

Choquet, É., Pueyo, L., Hagan, J. B., et al. 2014, in Society of Photo-Optical Instrumentation Engineers (SPIE) Conference Series, Vol. 9143, Proc. SPIE, 914357

Dodson-Robinson, S. E., & Salyk, C. 2011, ApJ, 738, 131, doi: 10.1088/0004-637X/738/2/131

Edwards, S., Hartigan, P., Ghandour, L., & Andrulis, C. 1994, AJ, 108, 1056, doi: 10.1086/117134

Foreman-Mackey, D., Hogg, D. W., Lang, D., & Goodman, J. 2013, PASP, 125, 306, doi: 10.1086/670067

Gaia Collaboration, Prusti, T., de Bruijne, J. H. J., et al. 2016, A&A, 595, A1, doi: 10.1051/0004-6361/201629272

Gaia Collaboration, Brown, A. G. A., Vallenari, A., et al. 2018, A&A, 616, A1, doi: 10.1051/0004-6361/201833051

Gregorio-Hetem, J., & Hetem, A. 2002, MNRAS, 336, 197, doi: 10.1046/j.1365-8711.2002.05716.x

Hashimoto, J., Dong, R., Kudo, T., et al. 2012, ApJ, 758, L19, doi: 10.1088/2041-8205/758/1/L19

Hashimoto, J., Tsukagoshi, T., Brown, J. M., et al. 2015, ApJ, 799, 43, doi: 10.1088/0004-637X/799/1/43

Hoeijmakers, H. J., Schwarz, H., Snellen, I. A. G., et al. 2018, A&A, 617, A144, doi: 10.1051/0004-6361/201832902

Huélamo, N., Chauvin, G., Schmid, H. M., et al. 2018, A&A, 613, L5, doi: 10.1051/0004-6361/201832874

Hunziker, S., Quanz, S. P., Amara, A., & Meyer, M. R. 2018, A&A, 611, A23, doi: 10.1051/0004-6361/201731428

Keppler, M., Benisty, M., Müller, A., et al. 2018, A&A, 617, A44, doi: 10.1051/0004-6361/201832957

Kley, W., & Nelson, R. P. 2012, ARA&A, 50, 211, doi: 10.1146/annurev-astro-081811-125523

Kley, W., Peitz, J., & Bryden, G. 2004, A&A, 414, 735, doi: 10.1051/0004-6361:20031589

Long, Z. C., Akiyama, E., Sitko, M., et al. 2018, ApJ, 858, 112, doi: 10.3847/1538-4357/aaba7c

Madec, P. Y., Arsenault, R., Kuntschner, H., et al. 2018, in Society of Photo-Optical Instrumentation Engineers (SPIE) Conference Series, Vol. 10703, Proc. SPIE, 1070302

Marois, C., Lafrenière, D., Doyon, R., Macintosh, B., & Nadeau, D. 2006, ApJ, 641, 556, doi: 10.1086/500401

Müller, A., Keppler, M., Henning, T., et al. 2018, A&A, 617, L2, doi: 10.1051/0004-6361/201833584

Natta, A., Testi, L., Muzerolle, J., et al. 2004, A&A, 424, 603, doi: 10.1051/0004-6361:20040356

Nelson, R. P., Papaloizou, J. C. B., Masset, F., & Kley, W. 2000, MNRAS, 318, 18, doi: 10.1046/j.1365-8711.2000.03605.x

Oberti, S., Kolb, J., Le Louarn, M., et al. 2016, in Society of Photo-Optical Instrumentation Engineers (SPIE) Conference Series, Vol. 9909, Proc. SPIE, 99091U

Pinilla, P., Benisty, M., & Birnstiel, T. 2012a, A&A, 545, A81, doi: 10.1051/0004-6361/201219315

Pinilla, P., Birnstiel, T., Ricci, L., et al. 2012b, A&A, 538, A114, doi: 10.1051/0004-6361/201118204

Pueyo, L. 2016, ApJ, 824, 117, doi: 10.3847/0004-637X/824/2/117

Rameau, J., Follette, K. B., Pueyo, L., et al. 2017, AJ, 153, 244, doi: 10.3847/1538-3881/aa6cae

Reipurth, B., Pedrosa, A., & Lago, M. T. V. T. 1996, A&AS, 120, 229

Rigliaco, E., Natta, A., Testi, L., et al. 2012, A&A, 548, A56, doi: `10.1051/0004-6361/201219832`

Smith, B. A., & Terrile, R. J. 1984, Science, 226, 1421, doi: `10.1126/science.226.4681.1421`

Soummer, R. 2005, ApJ, 618, L161, doi: `10.1086/427923`

Stolker, T., Bonse, M. J., Quanz, S. P., et al. 2019, A&A, 621, A59, doi: `10.1051/0004-6361/201834136`

Vigan, A., Moutou, C., Langlois, M., et al. 2010, MNRAS, 407, 71, doi: `10.1111/j.1365-2966.2010.16916.x`

Wagner, K., Follete, K. B., Close, L. M., et al. 2018, ApJ, 863, L8, doi: `10.3847/2041-8213/aad695`

Walsh, K. J., Morbidelli, A., Raymond, S. N., O'Brien, D. P., & Mandell, A. M. 2011, Nature, 475, 206, doi: `10.1038/nature10201`

Weilbacher, P. M., Streicher, O., Urrutia, T., et al. 2014, in Astronomical Society of the Pacific Conference Series, Vol. 485, Astronomical Data Analysis Software and Systems XXIII, ed. N. Manset & P. Forshay, 451

Xu, W., Lai, D., & Morbidelli, A. 2018, MNRAS, 481, 1538, doi: `10.1093/mnras/sty2406`

Zhu, Z., Nelson, R. P., Hartmann, L., Espaillat, C., & Calvet, N. 2011, ApJ, 729, 47, doi: `10.1088/0004-637X/729/1/47`

7 | Highly multiplexed Bragg gratings for large field of view gas sensing in planetary atmospheres.

Detecting and monitoring gas species is an important part of remote sensing because the state of the environment can be retrieved from the state of the gas species. This can be used to track temperature and pressure structures in the atmosphere for weather predictions, or monitor the air quality. Discriminating different species is easier at higher spectral resolution when the spectral lines are clearly resolved. The need to do this at high spatial resolution and over large fields of view leads to a trade-off between spectral and spatial resolution and spectral bandwidth. We propose to use a highly multiplexed Bragg grating that can optically combine the relevant information from the spectrum without the need to disperse the whole spectrum. This allows us to circumvent the spatial and spectral trade-off and therefore substantially increase the field of view compared to conventional hyperspectral imagers. A dynamic implementation based on acousto-optical filters that can be adapted on the fly is discussed as an easy and flexible way to create the multiplexed gratings. We describe the details of multiplexed Bragg gratings and show that we can retrieve the spatial distribution of individual species abundances in gas mixtures, and we show that we can even do this for the atmospheres of exoplanets orbiting far-away stars.

7.1   Introduction

Hyperspectral imaging is a corner stone of modern remote sensing. An important application is the monitoring of gases in the atmosphere, especially in urban areas where air pollution can be a serious health problem (Snik et al., 2014). Gas tracing is also done in industrial settings for the detection and monitoring of hazardous emissions from large industrial facilities (Williams et al., 2005; Wu et al., 2018), finding leaks in large gas pipes or the indoor formation of gases during production processes. Nowadays we also observe the atmospheres of other planets, even planets around stars other than our own Sun. In all these cases it is important to know where, when, which and how much gas is present. A sensor that is built to remotely detect these gases will need to be able to spatially and spectrally resolve the spectral absorption lines of these gases.

Gases have a specific spectral signature that is created by their atomic or molecular structure. These signatures become more distinct from each other at higher spectral resolution. An example can be seen in Fig. 1, where high-resolution transmission spectra of various molecules are generated with HAPY (Kochanov et al., 2016), the python interface of HITRAN2012 (Rothman et al., 2013). In the selected wavelength range methane shows a set of strong, distinct spectral lines that are quite different from the signatures of CO_2 and water. The difference is even more extreme compared to O_2, which does not have any features in this spectral range. By measuring the spectral information we can exploit the differences in spectral signatures between gases to classify and monitor them from a distance.

The presence of a molecular species in a spectrum can be found by using a matched spectral filter (Manolakis, 2002) that is tuned to the signature of the species of interest. A simple matched filter can be made with a binary mask that is equal to one where a spectral line is present and zero otherwise. Because most spectral lines of interest are absorption lines, the binary matched filter (BMF) will have a low signal when all the lines are present, as there is less flux inside the absorption line. On the other hand if the spectral lines are not present the signal will be high as there is no absorption.

For moving objects it is important to take the Doppler shift into account, which shifts the position of spectral lines. If the Doppler shift is neglected, it could lead to a miss-classification because the species is present but shifted. Small shifts can be accounted for by cross-correlating the measured spectrum with the matched filter. This has been successfully used

in astronomy to look for very weak signatures of molecular species in the atmospheres of extra-solar planets that are buried in the light of their host star (Brogi et al., 2012; Konopacky et al., 2013; Macintosh et al., 2015). For a clear detection of several gases it is important to have high-spectral resolving power, but a high-resolution spectrum for every point in the field-of-view is very costly in terms of detector real estate. Therefore most conventional hyperspectral imagers need to compromise between spatial and spectral resolving power.

An alternative way of measuring gases is by using a gas-filter correlation sensor[3, 8]. Here the light passes through a gas-cell that is filled with the species of gas that needs to be detected. If light of interest passes through a gascell containing methane, for example, the absorption features of methane will be imprinted in the light. Suppose that the light already had the lines of methane imprinted in it, because it passed through some clouds of methane in the Earth's atmosphere, then the total amount of light will not change much because all light that could have been absorbed by the methane in the gas-cell is already gone. If the light did not have the imprints of methane, the total intensity will decrease because light is lost due to the absorption by methane. Therefore if we pass the light through two gas cells, one containing methane and one empty reference cell, the ratio in intensity between the two will correlate with the presence of methane. This mimics the behaviour of a binary matched spectral filter. The gas-cell correlation method allows for a large field of view as the correlation signal can be recorded with only two pixels. A downside of the gas-cell sensor is its ability to only measure species with vanishing relative Doppler shift. If the input is Doppler-shifted, the absorption lines do not align anymore with the absorption lines of the gas-cell sensor, and the differential measurement will no longer detect the species.

For some species it may to be possible to create a solution that is purely optical and does not need gas cells. An example is the HIGS sensor that has been developed for NO_2 measurements (Verlaan et al., 2017). HIGS replaces the gas-cell correlation with an all-optical filter. HIGS uses an interferometer that has periodic fringes to create a matched spectral filter, which matches the periodic spectral lines of NO_2. Another example are the OH-suppression fiber Bragg gratings (Bland-Hawthorn et al., 2004). These are used to remove the atmospheric OH emission lines to decrease the amount of contamination they have on the astronomical spectrum of interest. While these methods may decrease the number of pixels, they lose precious information because the line shapes are sensitive to tempera-
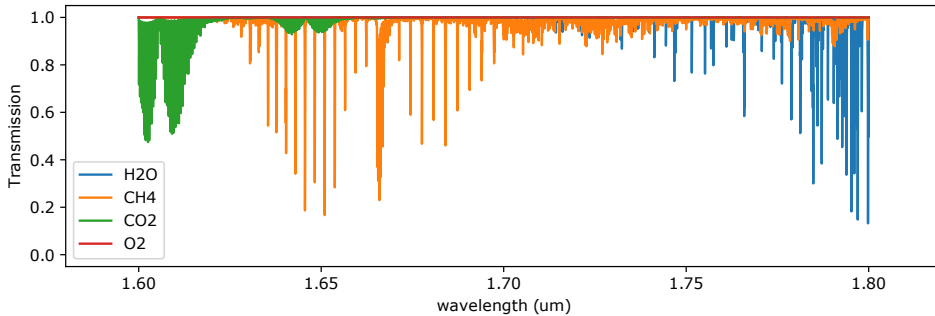
Figure 7.1:   The spectra of water, methane and carbon-dioxide are shown in the wavelength range from 1.6 to 1.8 μm. Each spectrum consists of many sharp spectral lines, but due to the amount and close proximity of the spectral lines, these can merge and form an absorption band, which can be seen as the shaded areas. The different molecules have distinct spectral features at high spectral resolution.

ture, pressure, velocity and molecular abundance variations. With careful monitoring of the spectral lines of interest it is possible to retrieve these parameters. But approaches like the gas-cell sensor or the HIGS lose this information as they reduce the full spectrum to a single intensity difference and therefore can only measure the abundance of the molecule.

In this work we present a dynamic, eletro-optical solution based on highly multiplexed acousto-optical volume Bragg gratings (HMBG), which can do the same measurement as gas-cell sensors but retain the spectral line shape information. The HMBG are also very flexible as it is possible to electronically switch the spectral filter. In Section 2 we discuss the principles of a Bragg grating and its multiplexing capabilities that are relevant for trace-gas measurements. In section 3 we highlight the advantages of the HMBG. In section 4 we discuss the trade-offs between different implementations of the HMBG. And in section 5 we showcase a few selected examples where the HMBG will have a major advantage over current approaches.

7.2   Multiplexed Bragg gratings

7.2.1   Bragg grating basics

Volume Bragg Gratings (VBG) are transmission gratings where the grating is written inside a piece of transparent material with as a periodic refractive index modulation. VBGs predominantly exhibit first-order diffraction while conventional transmission gratings diffract into multiple orders. These diffraction properties of Bragg gratings have been known since the 60's when Kogelnik proposed his coupled wave theory (Kogelnik, 1969). According to Kogelnik's theory a VBG optimally diffracts the wavelengths that satisfy the Bragg condition,

$$\lambda_B = 2n\Lambda \sin \theta_B. \tag{7.1}$$

λ_B is the Bragg wavelength, n the average refractive index of the material, Λ the pitch of the modulation and θ_B the angle of incidence. The Bragg wavelength is the wavelength that is matched to the period of the grating according to Eq. 7.1. The Bragg condition is nothing more than the blaze condition for conventional gratings. Wavelengths that deviate from the Bragg condition will be diffracted according to the grating equation,

$$\lambda = 2n\Lambda \left(\sin \theta_i + \sin \theta_d \right). \tag{7.2}$$

The geometry of the grating setup is similar to a normal grating spectrometer working in first order and can be seen in Fig. 7.2. The VBGs should not be confused with Fiber Bragg Gratings where the light travels along the modulation direction, which is the x-direction in Fig. 7.2.

The diffraction efficiency (DE) is the ratio between the amount of light that is diffracted into the first order and the amount of incoming light. A DE of 1 means that all the light is diffracted into the first order, while a DE of 0.5 means that half the light is diffracted and half the light remains in the zeroth order. Currently it is possible to manufacture VBGs with DEs above 99 percent (Glebov et al., 2012). The refractive index modulation that is necessary to obtain a 100 percent DE is (Ciapurin et al., 2005),

$$\delta n = \frac{\lambda_B \cos \theta_B}{2t}. \tag{7.3}$$

Here δn is the amplitude of the refractive index modulation and t is the thickness of the grating. The differential optical-path delay that is accrued while travelling through the grating is $\delta \text{OPD} = \delta n t / \cos \theta_B$. If Eq. 7.3 is
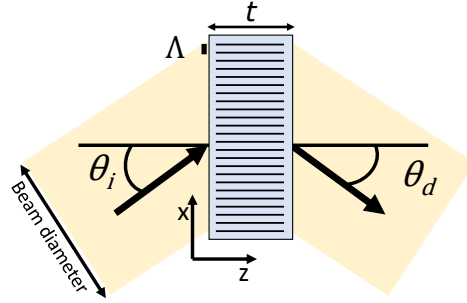
Figure 7.2: The geometry of the Volume Bragg Grating setup where a collimated beam enters the grating from the left. The grating with a line spacing of Λ is modulated along the x direction. The incidence and diffracted angle are defined as θ_i and θ_d, respectively. The incident beam propagates from the left to the right through the grating. The thickness t is the width of the grating along the z-direction while the transverse size is the size along the x-direction.

used to substitute δn we arrive at $\delta\mathrm{OPD} = \lambda/2$. For optimal diffraction efficiency the $\delta\mathrm{OPD}$ has to be half a wave. When the $\delta\mathrm{OPD}$ differs from half-wave the DE lowers, which can happen either due to a wrong angle of incidence or a wavelength that deviates from the Bragg wavelength. If the thickness of the grating is increased it becomes easier to violate the phase matching conditions, and therefore a smaller wavelength range will be diffracted. This reduces the effective spectral bandwidth of the grating. The diffraction efficiency curves for different thicknesses are shown in Fig. 7.3, which shows that thicker gratings have a sharper responses. We define the spectral bandwidth of the VBG as the half width at the first zero (HWFZ) (Ciapurin et al., 2005),

$$\frac{\Delta\lambda}{\lambda_B} = \frac{\sqrt{3}}{4}\frac{\Lambda}{t}\frac{\cos\theta_B}{\sin^2\theta_B}. \tag{7.4}$$

Here $\Delta\lambda$ is the HWFZ of the diffracted spectrum. The current range of volume phase gratings make it possible to have a spectral bandwidth below 0.1 nm to more than 100 nm (Ciapurin et al., 2005). This spectral bandwidth should not be confused with the spectral resolving power of the grating. The spectral bandwidth is the spectral range that is diffracted, while the resolving power of a VBG follows the same equation as a normal grating and therefore depends on the number of lines N that are illuminated and
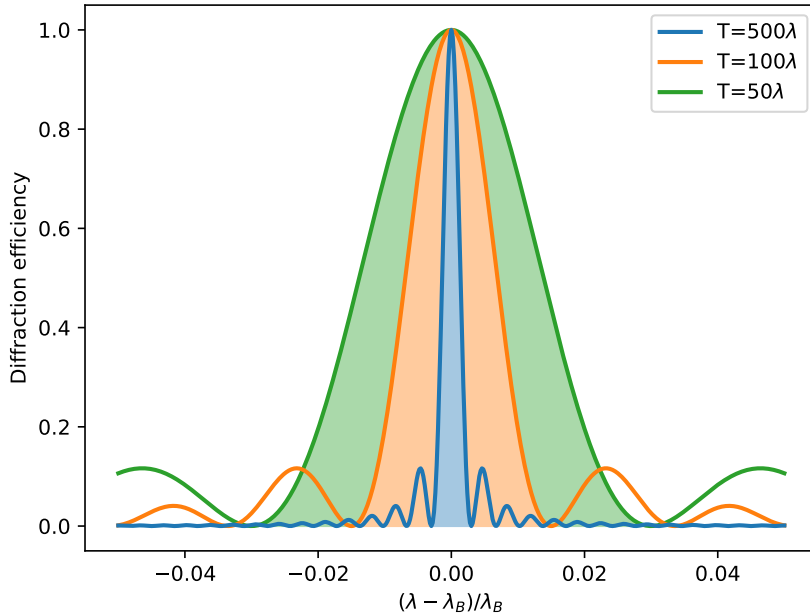
Figure 7.3: The diffraction efficiencies as function of the relative devia-
tion from the Bragg wavelength; each color represents a different grating
thickness. The shaded region below the curves highlight the area that is
spanned by the spectral bandwidth as defined by the Full Width at First
Zero (FWFZ). To first order the diffraction efficiencies follow a sinc^2 profile.

the order of diffraction m. Hence the transverse size of the grating deter-
mines the resolving power, while the thickness determines the diffracted
wavelength range.

7.2.2   Multiplexed Bragg gratings

It is possible to write multiple VBGs inside a single piece of glass where
each one addresses a different Bragg wavelength allowing multiple spectral
lines to be diffracted at once. By writing multiple VBGs the refractive
index modulation is not a simple cosine or sine any more but a coherent
superposition of many cosines. The multiplexed refractive index amplitude

is,

$$\delta n(x) = \sum_i^N \delta n_i \cos\left(2\pi x / \Lambda_i\right). \tag{7.5}$$

Here $\delta n(x)$ is the total refractive index modulation, δn_i is the amplitude for each individual grating and Λ_i is the pitch of each grating. We propose to use a Highly Multiplexed Bragg Grating (HMBG) that multiplexes tens to hundreds of gratings, each grating addresses a spectral line of interest. Each spectral line will be chosen as the Bragg wavelength of its grating, and we adjust the pitch according to Eq. 7.1 in such a way that the diffracted output angle is the same. A lens can then re-image all the different beams onto a detector. Because all spectral lines are diffracted into the same output direction, they will end up at the same position on the detector. This optically combines all spectral lines. An example of the output of a HMBG can be seen in Fig. 7.4. Because all lines are optically combined we do not need to sample the full spectrum but only the footprint of a single spectral line.

If we now assume that the spectral bandwidth of the grating is broader than the spectral lines of interest, then the spectrum of the object will be diffracted by the VBG such that a narrow slice around the line of interest will be isolated. The multiplexed grating will then create an incoherent sum of the individual slices, where the center of the summed spectra will show the average line profile. When many lines are multiplexed it becomes problematic to describe the dispersion axis with a wavelength coordinate as there are many wavelengths superimposed on the same pixel. The output angle of the relative change of wavelength can be found with the grating equation,

$$\frac{\delta\lambda}{\lambda_B} = \frac{1}{2}\frac{\sin\left(\theta_B + \Delta\theta\right) - \sin\theta_B}{\sin\theta_B}. \tag{7.6}$$

With $\delta\lambda$ the deviation from the Bragg wavelength. From this relation we can see that each output angle corresponds to the same amount of relative wavelength shift irrespective of the chosen λ_B. Under the assumption that the spectral lines of interest are chosen as the λ_B for their respective grating, they will all propagate in the same direction. We can relate the relative change of the wavelength to the relative radial velocity of the object of interest. Substituting the formula the for classical Doppler shifts we obtain,

$$\frac{\delta v}{c} = \frac{1}{2}\frac{\sin\left(\theta_B + \Delta\theta\right) - \sin\theta_B}{\sin\theta_B}. \tag{7.7}$$
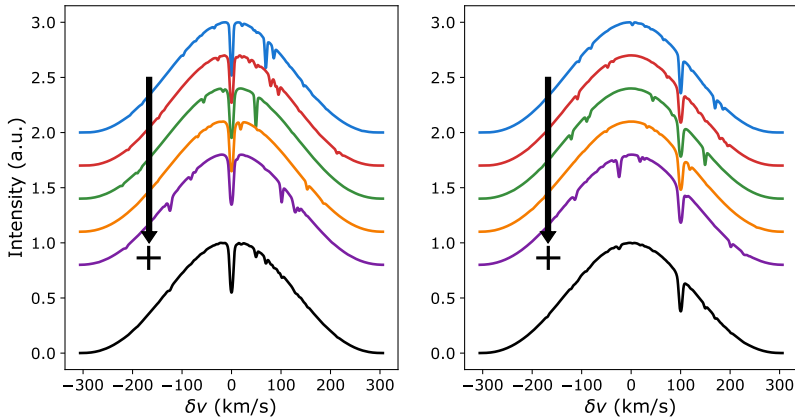
Figure 7.4: Two example signals from the HMBG for 5 randomly chosen
lines from a stellar spectrum. The individual responses for each grating
are shown by the coloured spectra. For readability each spectrum was
offsetted in the vertical direction. The HMBG creates a slice around each
spectral line of interest onto the detector. The actual detected response
is the integrated signal shown in black. The envelop of the signal is the
diffraction efficiency curve, and if the species of interest is present we can
see the average line profile at the objects Doppler shift. Depending on
the velocity of the target the average line profile will coherently shift and
remains detectable as can be seen in the figure on the right where the
object has a Doppler shift of 100 km/s. All spectral features other than
the spectral lines of interest are washed out due to the incoherent sum of
different slices.

The output angle is independent of any of the grating periods and only
depends on the velocity shift $\frac{\delta v}{c}$. The HMBG maps the quasi-matched
filter response of a species at a certain radial velocity to an output angle
independent of the chosen grating period; it is therefore natural to use
velocity coordinates.

   The velocity shift that can be resolved depends on the spectral resolving
power of the grating, $\delta v = c/R$. The velocity bandwidth is set by the
spectral bandwidth, which in turn is set by the thickness of the grating.
A thicker grating will have a narrower velocity bandwidth, which can be

derived from Eq. 7.6,

$$\frac{\Delta v}{c} = \frac{\sqrt{3}}{4} \frac{\Lambda}{t} \frac{\cos \theta_B}{\sin^2 \theta_B}.$$

(7.8)

Here Δv is the velocity bandwidth. These two parameters need to be taken into account during the design of a HMBG. The design of a HMBG starts with the choice of a velocity bandwidth, because this determines the minimum spacing between spectral lines that can be multiplexed together. Then the spectral lines can be chosen and the grating period can be calculated from Eq. 7.1.

7.2.3   Simulating diffraction efficiencies

To design an efficient instrument the grating diffraction efficiency should not decrease with the number of lines that are multiplexed, otherwise there would be no point in trying to add more lines. Multiplexed Bragg gratings are usually calculated with Rigorous Coupled Wave Theory (Moharam & Gaylord, 1981). This is an extension of the simple coupled-wave theory of Kogelnik. The downside to RCWT-like codes is that they couple all the modes that are present in the system. The gratings will couple with each other, and if we want to know the diffraction efficiencies of M diffraction orders on N multiplexed spectra, we need to include M^N modes. For $M = 2$, which includes the 0th and 1st order, and $N = 100$ this already leads to an unmanageable computing time.

   The RCWT only needs to be used if the spectral lines are close to each other. As said before if the lines are separated enough, the response can be calculated as an incoherent superposition of the individual responses. To check this we wrote a symmetric split-step Fourier beam propagation code (BPM) (Blanes & Moan, 2000). This code can propagate an electric field through arbitrary refractive index profiles. The speed of the code only depends on the spatial sampling of the grating, and therefore it is independent of the amount of multiplexed gratings as opposed to RCWT-like codes. The BPM code has been validated on several test cases including free-space propagation, waveguide propagation and diffraction from a single Volume Bragg Grating. In all cases the power was conserved to better than 0.1 %, and the single VBG simulation showed a diffraction efficiency curve that followed the curve as derived by Kogelnik.

   As an initial test case, we created N randomly positioned spectral lines between 0.5 μm to 1.0 μm. The lines are separated by at least three times the FWHM of the spectral bandwidth (Fu et al., 1997). This directly gives the spectral bandwidth necessary for the uncoupled regime. The

peak diffraction efficiency of each grating is then calculated by propagating its Bragg wavelength. The average diffraction efficiency of the grating converges to 100 percent for all number of lines that we tried. The grating that multiplexes a 100 lines converges to 97 percent, which is slightly lower than 100 percent because of numerical inaccuracies. The BPM code includes all possible types of crosstalk between the gratings, and we see no major cross talk, which we expected based on (Fu et al., 1997). This result encouraged us to use a simpler model where the response is just a superposition of the individual responses.

7.3   Advantages of multiplexed Bragg gratings

Our method has several advantages over recording the full spectrum. The most important one is that it can reduce the amount of pixels per spatial pixel (spaxel) considerably because we do not need to record the complete spectrum. This substantially decreases the required number of pixels per spatial pixel and makes it possible to increase the field of view compared to a conventional spectrograph for a fixed detector size. The downside to this method is that we lose the full spectral information. The number of pixels required per spaxel depends on the velocity bandwidth and velocity resolution. The bandwidth is given by the maximum Doppler shift one wants to measure. The velocity resolution is directly related to an equivalent spectrograph resolution,

$$\delta v = \frac{c}{N_{\mathrm{sampling}} R}. \tag{7.9}$$

Here δv is the velocity sampling, and N_{sampling} is the number of pixels per spectral resolving element and R is the resolving power defined as $R = \lambda/\delta\lambda$. The amount of pixels that is necessary to sample the full velocity bandwidth on a detector is,

$$N_{\mathrm{v}} = \frac{\Delta v}{\delta v} = \frac{\Delta v}{c} N_{\mathrm{sampling}} R. \tag{7.10}$$

To know the reduction in detector space we need to compare this to a traditional spectrograph. A spectrograph must have a bandwidth $\Delta\lambda$ that is large enough to contain all the spectral lines. The wavelength sampling should be,

$$\delta\lambda = \frac{\lambda}{N_{\mathrm{sampling}} R}. \tag{7.11}$$

The amount of pixels this will require is

$$N_\lambda = \frac{\Delta\lambda}{\delta\lambda} = \frac{\Delta\lambda}{\lambda}N_{\text{sampling}}R. \tag{7.12}$$

The reduction in detector space is then

$$N_{\text{gain}} = \frac{N_\lambda}{N_{\text{v}}} = \frac{c}{\Delta v}\frac{\Delta\lambda}{\lambda}. \tag{7.13}$$

Interestingly the detector space reduction is independent of the resolving power and purely depends on the bandwidths that are required. Following this equation we estimate the amount of detector space that can be gained for Earth observations. Earth observations are usually done from Low-Earth Orbit (LEO) satellites that have velocities of roughly 10 km/s. We should therefore select a velocity range that can easily accommodate this speed, which we chose at $\Delta v = \pm 50$ km/s. To contain the most interesting lines we would like spectral coverage from 1μm to 3.5 μm. For this spectral range and velocity bandwidth we estimate that the detector area reduction is between 2500 and 18000, depending on which wavelength is Nyquist sampled.

The signal-to-noise(SNR) ratio of the HMBG signal is, to first order,

$$\text{SNR} = \frac{F_0\sqrt{NR}}{\sqrt{F_0 + \sigma_{\text{D}}^2}}. \tag{7.14}$$

Here F_0 is the average photon flux ratio between the continuum and the selected spectral lines, N the number of spectral lines that are multiplexed, R the spectral resolving power and σ_{D} the read and dark noise. Comparing this to the SNR ratio of normal spectroscopy,

$$\text{SNR} = \frac{F_0\sqrt{NR}}{\sqrt{F_0 + \sigma_{\text{D}}^2 N}}, \tag{7.15}$$

we see that the effects of read noise and dark noise are decreased by the number of spectral lines that are multiplexed because the spectral lines are added together on the same pixel. For faint signals the HMBG will achieve higher SNR compared to normal spectroscopy because the HMBG spreads the light over fewer pixels. A disadvantage of the HMBG is that it cannot multiplex all spectral lines, as some will be too close together. Therefore the HMBG cannot use all available spectral lines, and the SNR of the HMBG

compared to normal spectroscopy will be lower in the photon-noise limited regime. To estimate the SNR decrease we used the spectra of Fig. 7.1 to estimate the number of lines and the average line depth for each species. We again assumed a velocity bandwidth of $\Delta v = \pm\ 50$ km/s, and found that we are able to multiplex on average 75 spectral lines per species from 1.6 μm to 1.8 μm. Not all spectral lines are of the same importance as their depth, and therefore their contribution to the SNR budget, varies. The ratios of the SNR of the HMBG compared to the SNR of normal spectroscopy for the three species are, 0.5 for CO_2, 0.77 for H_2O and 0.77 for CH_4. The HMBG will be at most a factor of 2 less sensitive in the photon-noise limited regime for the considered case.

Another advantage of the multiplexed grating over gas-cell correlations is that it is also allows for correlation measurements for species that are difficult to contain in a gas cell. Therefore the HMBG can achieve the same kind of sensitivity as the gas-cell correlators but for a wider range of objects. The second advantage compared to the gas-cell sensor is that the HMBG measurements retain spectral line information.

7.4   Multiplexed Bragg grating implementation

7.4.1   Static system

There are several ways to implement multiplexed gratings. The simplest solution is to physically put several transmission gratings in series (Alessio et al., 2017). The disadvantage of stacking gratings is that it quickly becomes a very thick optical element as the number of multiplexed lines increase. For a few tens of lines the thickness can quickly reach several tens of centimeters, which will require a substantial over-sizing of the grating to avoid issues with vignetting. The different gratings will also diffract the light at different planes as the gratings are physically stacked after each other. This will put very stringent requirements on the imaging lens, if at all possible, to make sure that all the chosen spectral lines will still fall on the same location on the detector. Therefore, if a multiplexed grating with many lines is required, it will be necessary to write the gratings in a single piece of glass. There are several manufacturing techniques that can write complicated refractive-index profiles. For Volume Bragg Gratings the most common technique is holography.

In holographic writing two beams are tilted with respect to each other, which creates a sinusoidal interference pattern. The angle between the

beams can be adjusted to create the correct line spacing. With holography the different gratings will be written sequentially. This creates an incoherent addition of the gratings in the material, leading to a refractive index profile given by,

$$\delta n(x) = \sum_i^N \delta n_i \frac{1 + \cos\left(2\pi x / \Lambda_i\right)}{2}. \tag{7.16}$$

Due to the incoherent addition the refractive index modulation grows linearly with the number of spectral lines, quickly saturating the writing material (Hong et al., 1990; Kaim et al., 2015). This can be circumvented by coherently writing the gratings that create a refractive index profile as determined by Eq. 7.5. For a coherent multiplexed grating the refractive index modulation grows as the square root of the number of gratings allowing for many more gratings to be written in the material. Recent literature on the dynamic range of holographic materials shows that the maximum refractive index modulation can be as high as 0.03 (Alim et al., 2018). A grating with a thickness of 1000 waves at a 25 degree incidence angle requires an index modulation of 0.00045 according to Eq. 7.3. The number of lines that can be written before the material saturates is about 60 for incoherent writing while coherent writing could reach roughly 4000 lines. This demonstrates the clear advantage of the coherent approach over the incoherent approach, but it requires a different manufacturing strategy.

Direct write methods where the refractive index is modified point-by-point can write coherent multiplexed gratings. An example of a highly multiplexed grating is the OH suppression filter written inside single-mode fibers (Bland-Hawthorn et al., 2004; Ellis et al., 2012). This filter is able to multiplex tens to hundreds of gratings for the suppression of the atmospheric OH lines. Direct write techniques are now also being used to write 2D gratings that can achieve diffraction efficiencies higher than 90% (Butcher et al., 2017; MacLachlan et al., 2013; Mikutis et al., 2013).

7.4.2   Dynamic system

The down-side of writing a multiplexed grating into glass is that the grating cannot be changed afterwards. The resulting HMBG can only measure the signal of a single species. This leads to a cumbersome system for situations where multiple species need to be measured. An active system where the spectral template can be changed on the fly would address this issues; it can be achieved with acousto-optical (AO) gratings. In acousto-optical materials the local refractive index can be changed by passing sound waves

through the transparent material. High-quality acousto-optical materials have been on the rise in the past decades and have become quite common in recent years. Low-resolution versions of the proposed idea have been in use as acousto-optical tunable filters. In AOTFs the sound waves are tuned to the central wavelength to create bandpass filters that are digitally tunable. There are versions which can have multiple bandpasses at the same time. Another advantage of the AOTFs is the use of multiple transducers to create the sound waves. If the transducers are used as a phased array one can create an arbitrary 3D refractive index profile (Grinenko et al., 2015). This can be used to apodize the sidelobes of the diffraction efficiency curve for a more uniform efficiency over the spectral bandwidth because for normal VBGs the efficiency drops off as the spectral lines of interest are more Doppler shifted.

7.4.3   Challenges when implementing as a hyper-spectral imager

An sketch of the proposed hyperspectral camera can be seen in Fig. 7.6. The main challenge for the HMBG for large fields of view will be the acceptance angle of the grating itself. The output angle of the grating shifts if the input angle is different from the Bragg angle. If the angular shift is too large, the spectral line of interest can move beyond the spectral bandwidth and make it unobservable. This constraints the acceptance angle of the HMBG. The output angle can be found with the grating equation,

$$\lambda = n\Lambda \left(\sin \left[\theta_B + \theta_{\text{in}}\right] + \sin \left[\theta_B + \theta_{\text{out}}\right] \right). \tag{7.17}$$

Here θ_{in} and θ_{out} are the deviations from the Bragg angle. Expanding the input and output angles around the Bragg angle and subtracting the Bragg wavelength leads to,

$$\lambda - \lambda_B = n\Lambda \cos \theta_B \left(\theta_{\text{in}} + \theta_{\text{out}} \right). \tag{7.18}$$

From this equation we can see that when we consider the Bragg wavelength ($\lambda - \lambda_B = 0$), the output angle will shift by the same amount as the input angle is shifted away from the Bragg angle. The input acceptance angle is therefore the same as the output acceptance angle. We can derive the maximum output angle from Eq. 7.7 using the velocity bandwidth. The acceptance angle as a function of velocity bandwidth is shown in Fig. 7.5 for several different Bragg angles. Here we can see that the angle of acceptance is smaller than one degree for most cases.
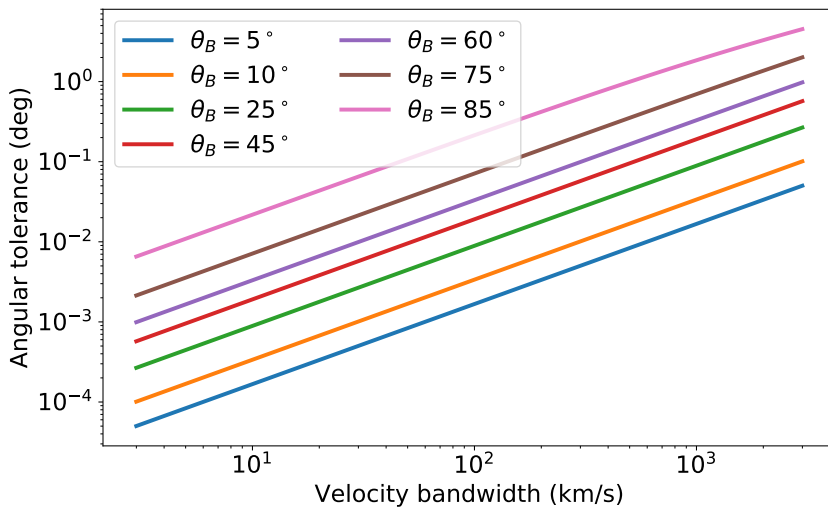
Figure 7.5: The angular tolerance as a function of velocity bandwidth. The velocity bandwidth is shown from 3 to 3000 km/s. The colored lines represent different Bragg angles. As the Bragg angle increases, the acceptance angle increases.
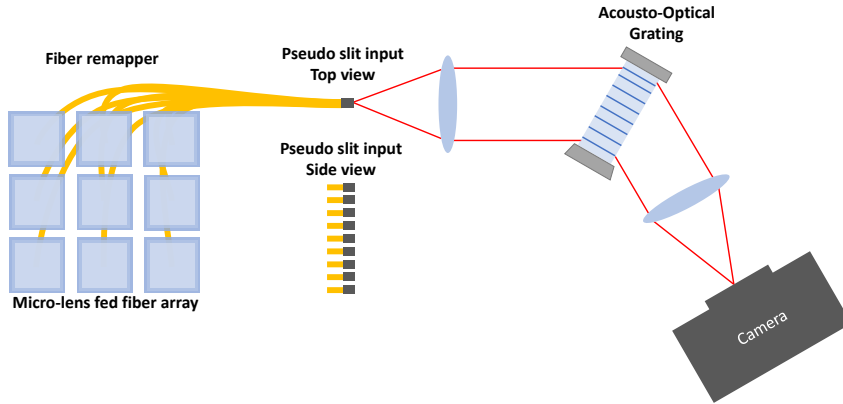
Figure 7.6: A sketch of the proposed setup. The two-dimensional input is remapped through a fiber array into a pseudo-slit. The pseudo-slit feeds the spectrograph in a first-order grating configuration.

Due to the small acceptance angle of the HMBG any deviation of the input angle from the Bragg angle needs to be minimized. Therefore the HMBG can only accept slit-like inputs where all light has the same angle of incidence on the grating. For two-dimensional field-of-views we need to map the field into a slit, which can be done with either advanced image slicers (Content, 1998) or fiber bundles (Smith et al., 2004).

7.5 Applications of the Highly Multiplexed Bragg Grating

7.5.1 Highly Multiplexed Bragg Grating instrument model

The HMBG response is simulated with a simple model where all gratings are considered independently. This assumption is valid as long as we make sure that all gratings are in the uncoupled regime. For this model the intensity on a pixel for grating i with a fixed input angle θ_{in} is,

$$I_i\left(\theta\right) = \int S\left(\lambda\right)\eta_i(\lambda, \theta_{\text{in}})H_i\left(\lambda, \theta, \theta_{\text{in}}\right)d\lambda, \qquad (7.19)$$

where θ is the output angle of the grating, S is the input spectrum of the scene, η_i is the diffraction efficiency of the grating and H_i is the line spread function (LSF). The LSF is taken as a simple sinc function with a full-width half maximum that is matched to the spectral resolving power R. This shape of the LSF arises because of the assumption of an uniformly illuminated square grating. The spectral dispersion of the LSF is calculated from the grating equation. For a multiplexed grating we sum over all gratings i, which results in the detector signal,

$$I\left(\theta\right) = \sum_i I_i\left(\theta\right). \tag{7.20}$$

7.5.2 Abundance retrieval of molecular species

A key aspect of remotely sensing a gas is to measure the amount of gas that is present, which can be achieved with the HMBG. Here we first show that for optically thin lines there exists a linear relation between the amount of gas and the HMBG output. We start by considering a single, plane-parallel layer of material for which the transmission can be written as,

$$T\left(\lambda\right) = e^{-\tau(\lambda)}. \tag{7.21}$$

Here $T\left(\lambda\right)$ is the transmission as a function of wavelength λ, and τ is the total optical depth at wavelength λ. From here on the explicit dependence of T and τ on λ will be left out. For a mixture of gases the optical depth can be described by,

$$\tau = \sum_i \tau_i = \sum_i n_i \sigma_i. \tag{7.22}$$

This sum is over all species i with a column density n_i and absorption cross-section σ_i. The optical depth of each individual species is the product of the wavelength-independent column density and the absorption cross-section. In the optically thin regime $\tau \ll 1$ the transmission becomes,

$$T = 1 - \tau + \mathcal{O}(\tau^2) \approx 1 - \sum_i n_i \sigma_i. \tag{7.23}$$

For optically thin lines the transmission depends linearly on the column density. Our model of the HMBG, according to Eq. 7.19, is a linear transformation from the input spectrum to the multiplexed dispersed measurement. Therefore there should be a linear relation between the HMBG output and the column density for optically thin lines.

This relation can be empirically calibrated by measuring the response of the HMBG to known amounts of each species of interest. The individual measurements from templates are stacked together in one vector $\vec{S}$. These measurements are then fitted by the following linear model,

$$\vec{S} = A\vec{n} + \vec{b}. \tag{7.24}$$

Here $\vec{S}$ is the stacked response, which contains the full line shape information, for all templates, A is the transformation matrix and $\vec{b}$ is the offset. We test the accuracy of the retrieval with a mixture of H_2O, CH_4 and CO_2. The HMBG template is made from the spectral lines shown in Fig. 7.1. For each template we search for the strongest spectral lines in the wavelength range. Our algorithm searches iteratively for the strongest spectral line and adds it to the line-list. Each time a line is selected we check if the distance to any of the spectral lines in our line-list is smaller than a threshold. If it is smaller we reject the new line and go to the next strongest line. The threshold is set at three times the FWHM of the spectral bandwidth to make sure we are in the regime where the gratings are uncoupled (Fu et al., 1997). This is not necessarily the optimal way of choosing which lines to multiplex for the different templates, but one that is relatively easy to implement.

We used column densities from $n = 10^{10} - 10^{15}$ cm^{-2} to determine the linear retrieval model parameters since the simulations had shown that these densities were well within the optically thin regime. Then we applied this model to retrieve densities from $n = 10^{10} - 10^{21}$ cm^{-2}. The results are shown in Fig. 7.7. The column density of each species is retrieved over the full range. Methane shows a small deviation above 10^{19}cm^{-2} where the selected spectral lines become optically thick. The linear response can be extended over a larger range by selecting only spectral lines that are optically thin for the column densities of interest, which is an advantage of dynamically selecting the spectral template. This is not possible with gas-cell correlators because the gas-cell contains all spectral lines including the lines that become optically thick. There is also cross-talk between the species. The cross-talk of methane to the other species is the strongest, which was expected as the cross-section of methane is the largest in this range. The cross-talk itself grows as the square of the column density because of the linear approximation of Eq. 7.23. The cross-talk can be decreased by carefully selecting the spectral lines that will not blend with the lines of other species. This can be accomplished by orthogonalizing the cross-section spectra of the different species with a Gram-Schmidt procedure (Sparks & Ford, 2002). The influence of cross-talk can also be reduced
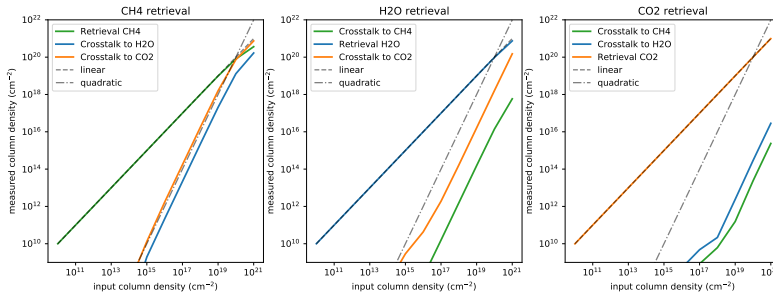
Figure 7.7: This figures shows the accuracy of the HMBG in combination with the linear retrieval algorithm for estimating the column density for single species. The input column density versus the retrieved column density is shown for CH_4, H_2O and CO_2. While each species has its own measurement template in the HMBG, there will still be cross-talk in due to non-linearities that are not taken into account in the retrieval. The cross-talk lines show the influence that the presence of the other species have on the retrieval. In the optically thin regime the cross-talk is very small and grows as the square of the column density.

by selecting a larger or different wavelength range that includes more distinct lines.

7.5.3 Molecule maps

To estimate the accuracy of the linear extraction for a mixture of gases we simulated a single two-dimensional map with a variable mixture of H_2O, CH_4 and CO_2. The spatial distributions of the gases were randomly created with column densities ranging from $10^{10} cm^{-2}$ to $10^{18} cm^{-2}$. For every pixel we simulated the response to the different templates from the previous section and applied the linear reconstructor to measure the column densities. The results can be seen in Fig. 7.8. The method recovers the column densities with high accuracy and precision. The average relative reconstruction error is much smaller than one percent. We can see that in the regions with a higher density of CH_4 there is more cross-talk. This influences the reconstruction of the other species. The non-linear cross-talk is stronger for CO_2 than for H_2O, which was also expected based on Fig. 7.7.
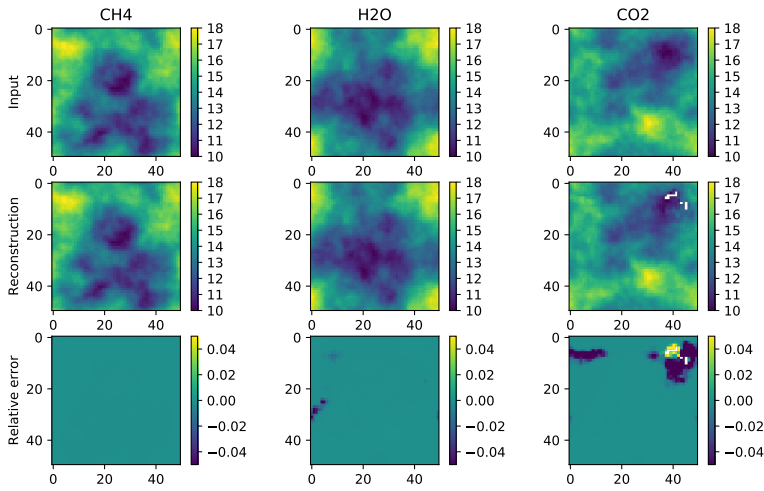
Figure 7.8: The retrieval of the column density is shown separately for CH_4, H_2O and CO_2. The top row shows the input column density and the middle row shows the retrieved column density. The bottom row shows the relative error in the retrieval. The relative error for CH_4 is much smaller than a percent. The other two species have larger relative errors with a maximum relative error of 15 percent. The large deviations occur at the places with high CH_4 column densities where the non-linearities that were not taken into account in the retrieval become important.

7.5.4   Exoplanet detection

Another application of the HMBG technique is in the field of astronomy for the detection and/or characterization of exoplanet atmospheres. The main problem for exoplanet detection is the contrast in intensity between the host star and the planet itself. The host star is usually brighter by a factor of a million for the largest and hottest exoplanets to a billion for old and cold Earth-like planets (Bowler, 2016). The standard method for detecting exoplanets is through very careful subtraction of the Point-Spread Function (PSF) of the star (Bowler, 2016; Marois et al., 2006). If the incoming wavefront changes the PSF of the star, then this subtraction scheme will not reach the ultimate sensitivity given by photon noise. This can happen for example due to turbulence in the Earth's atmosphere or slowly varying instrumental wavefront errors (Martinez et al., 2013).

High-resolution spectroscopy ($R \approx 100000$) has been proposed as a solution to find planets because we can discern the difference between the star and the planet based on the difference in their spectral lines (Snellen et al., 2015; Sparks & Ford, 2002). The downside of the method is its need for a large amount of pixels, and therefore it has a small discovery space. With the HMBG we can do exactly the same measurement but with less pixels, which substantially increases the discovery space for exoplanets. To show the potential of the HMBG we simulated a dataset of a star with a planet around it. The simulation has been done with wavefront errors that vary in time to simulate residual turbulence and varying instrumental effects. We used a PHOENIX model (Husser et al., 2013) with an effective temperature of 6000 K to create a sun-like spectrum for the star. For the planet spectrum we assumed that we only see reflected starlight and took the spectrum as a Doppler-shifted and flux-scaled replica of the stellar spectrum with a contrast of 10^{-6}. To search for the planet we created a HMBG template that stacked the 120 deepest lines of the stellar spectrum in the wavelength range from 0.9μm to 1.1μm. The velocity bandwidth around each line is 100 km/s, and the resolving power is set to 3 km/s. We expect to see two absorption lines in the multiplexed signal, one from the star at zero velocity and one at 25 km/s, which is the planet's radial velocity.

The planet signal can be recovered from the HMBG data cube by subtracting the spatially averaged HMBG measurement from every point in the field of view. The results of the simulations can be seen in Fig. 7.9 where we compare the HMBG planet detection with a classical PSF subtraction algorithm, namely Angular Differential Imaging (ADI) (Marois
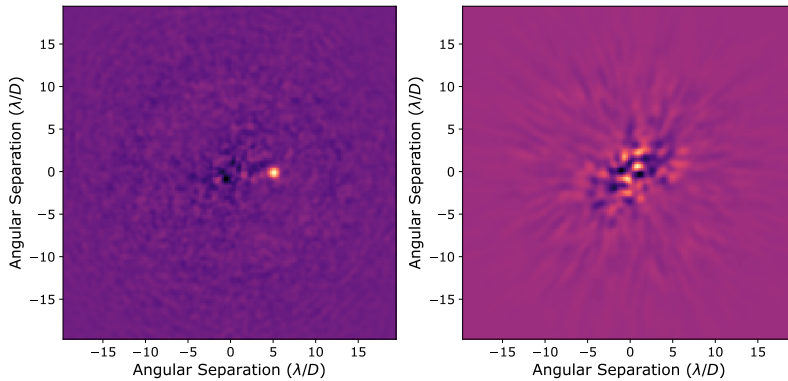
Figure 7.9:   The HMBG holds great promise for the detection and characterization of exoplanets. The two figures show the greatly enhanced capabilities of the HMBG (left) vs the classical approach currently used by astronomers (right). The planet is clearly visible with the HMBG while the ADI processed data still show strong speckle noise. This demonstrates that the HMBG is not limited by speckle noise, which is the major limiting factor for current observations of exoplanets.

et al., 2006). ADI creates a references PSF by averaging the PSF in time while the field is rotating. Due to the field rotation the apparent position of the planet will rotate and, if the planet rotates enough, it will not appear in the time-averaged PSF. The limits of ADI will be mainly dictated by how fast the PSF changes due to varying wavefront errors and how fast these will average out. In our simulations the ADI technique is limited to a contrast of 3000 at an angular distance of 5 λ/D for this dataset, while the HMBG can still clearly detect the planet at a contrast of 10^{-6}. This simple simulation shows that the HMBG measurements are robust to the speckle noise, while algorithms like ADI are not. The HMBG can therefore image fainter objects at smaller angular separations where observations are strongly speckle-noise limited.

7.6 Conclusion

We have shown that Volume Bragg gratings with many multiplexed gratings can be used for the quantitative detection of gas species with a significantly smaller detector than a comparable hyperspectral imager. This allows for a larger field-of-view given the same amount of detector real estate. We proposed to implement the HMBG with acousto-optical gratings that can be dynamically tuned at high speed and work from the near UV to the infrared. The dynamical aspect of the acousto-optical materials will allow us to use the same optics to detect different species. This simplifies the whole instrument as we can digitally choose what we would like to observe and thereby make the instrument highly flexible.

A major advantage of the HMBG over the traditional gas-cell correlation is that the HMBG retains the line profile and information about the continuum. This enables us to estimate column densities over a large range of densities and species mixtures. And we have also shown its use as a method for detecting reflected light from exoplanets, but detailed end-to-end simulations will be necessary to determine the exact performance gain of the HMBG compared to traditional exoplanet detection methods. The next step will be to build a prototype HMBG to verify the proposed concept and explore several aspects of the acousto-optical implementation such as the limits of the multiplexing capability and the angular tolerance.

Funding Information

Bibliography

Alessio, Z., Marco, L., Marco, R., & Andrea, B. 2017, ArXiv e-prints. `https://arxiv.org/abs/1704.08150`

Alim, M. D., Mavila, S., Glugla, D. J., et al. 2018, in Society of Photo-Optical Instrumentation Engineers (SPIE) Conference Series, Vol. 10558, 105580D

Bland-Hawthorn, J., Englund, M., & Edvell, G. 2004, Optics Express, 12, 5902

Blanes, S., & Moan, P. 2000, Physics Letters A, 265, 35

Bowler, B. P. 2016, PASP, 128, 102001, doi: `10.1088/1538-3873/128/968/102001`

Brogi, M., Snellen, I. A., de Kok, R. J., et al. 2012, Nature, 486, 502

Butcher, H. L., Lee, D., Brownsword, R., et al. 2017, Opt. Express, 25, 33617, doi: 10.1364/OE.25.033617

Ciapurin, I. V., Glebov, L. B., & Smirnov, V. I. 2005, in Proc. SPIE, Vol. 5742, Practical Holography XIX: Materials and Applications, ed. T. H. Jeong & H. I. Bjelkhagen, 183–194

Content, R. 1998, in Infrared Astronomical Instrumentation, Vol. 3354, International Society for Optics and Photonics, 187–200

Ellis, S. C., Bland-Hawthorn, J., Lawrence, J., et al. 2012, MNRAS, 425, 1682, doi: 10.1111/j.1365-2966.2012.21602.x

Fu, X., Fay, M., & Xu, J. M. 1997, Opt. Lett., 22, 1627, doi: 10.1364/OL.22.001627

Glebov, A. L., Mokhun, O., Rapaport, A., et al. 2012, in Proc. SPIE, Vol. 8428, Micro-Optics 2012, 84280C

Grinenko, A., MacDonald, M. P., Courtney, C. R. P., et al. 2015, Opt. Express, 23, 26, doi: 10.1364/OE.23.000026

Hong, J. H., Yeh, P., Psaltis, D., & Brady, D. 1990, Opt. Lett., 15, 344, doi: 10.1364/OL.15.000344

Husser, T.-O., Wende-von Berg, S., Dreizler, S., et al. 2013, Astronomy & Astrophysics, 553, A6

Kaim, S., Mokhov, S., Divliansky, I., et al. 2015, J. Opt. Soc. Am. A, 32, 22, doi: 10.1364/JOSAA.32.000022

Kochanov, R. V., Gordon, I., Rothman, L., et al. 2016, Journal of Quantitative Spectroscopy and Radiative Transfer, 177, 15

Kogelnik, H. 1969, Bell System Technical Journal, 48, 2909, doi: 10.1002/j.1538-7305.1969.tb01198.x

Konopacky, Q. M., Barman, T. S., Macintosh, B. A., & Marois, C. 2013, Science, 339, 1398

Macintosh, B., Graham, J., Barman, T., et al. 2015, Science, 350, 64

MacLachlan, D. G., Thomson, R. R., Cunningham, C. R., & Lee, D. 2013, Opt. Mater. Express, 3, 1616, doi: 10.1364/OME.3.001616

Manolakis, D. G. 2002, in Society of Photo-Optical Instrumentation Engineers (SPIE) Conference Series, Vol. 4725, 4725 – 4725 – 14. https://doi.org/10.1117/12.478752

Marois, C., Lafrenière, D., Doyon, R., Macintosh, B., & Nadeau, D. 2006, Astrophysical Journal, 641, 556, doi: 10.1086/500401

Martinez, P., Kasper, M., Costille, A., et al. 2013, Astronomy & Astrophysics, 554, A41

Mikutis, M., Kudrius, T., Šlekys, G., Paipulas, D., & Juodkazis, S. 2013, Opt. Mater. Express, 3, 1862, doi: 10.1364/OME.3.001862

Moharam, M., & Gaylord, T. 1981, JOSA, 71, 811

Rothman, L. S., Gordon, I. E., Babikov, Y., et al. 2013, Journal of Quantitative Spectroscopy and Radiative Transfer, 130, 4

Smith, G. A., Saunders, W., Bridges, T., et al. 2004, in Ground-based Instrumentation for Astronomy, Vol. 5492, International Society for Optics and Photonics,

410–420

Snellen, I., de Kok, R., Birkby, J., et al. 2015, Astronomy & Astrophysics, 576, A59

Snik, F., Rietjens, J. H. H., Apituley, A., et al. 2014, Geophysical Research Letters, 41, 7351, doi: `10.1002/2014GL061462`

Sparks, W. B., & Ford, H. C. 2002, Astrophysical Journal, 578, 543, doi: `10.1086/342401`

Verlaan, A., Klop, W., Visser, H., van Brug, H., & Human, J. 2017, in International Conference on Space Optics—ICSO 2016, Vol. 10562, International Society for Optics and Photonics, 105625Z

Williams, D. J., Feldman, B. L., Williams, T. J., et al. 2005, in Proc. SPIE, Vol. 5655, Multispectral and Hyperspectral Remote Sensing Instruments and Applications II, ed. A. M. Larar, M. Suzuki, & Q. Tong, 134–141

Wu, K., Feng, Y., Yu, G., et al. 2018, Opt. Express, 26, 8239, doi: `10.1364/OE.26.008239`

8 | English Summary

The field of exoplanets has seen rapid development in the past three decades since the discovery of the first few exoplanets. In 1992 the first planet around a star other than our own had been found, and just three years later in 1995 the first exoplanet orbiting a solar-like star was discovered. We now have found several thousands of planets, that are so diverse that it seems like that almost every system is unique. There are strange planets like Kepler 51 b and d that have densities similar to cotton candy or the extremely hot KELT-9b that has gaseous iron and titanium in its atmosphere. Not only is there a large diversity in the planets themselves but there is also a large diversity in the composition of planetary systems. On one side there is Trappist-1 with seven Earth-mass planets with short orbital periods around a red dwarf star, and on the other extreme there is HR8799 with four giant gas planets on very wide orbits. This challenges our theories of planet formation as it should be able to explain the diversity. One of the key questions is how the planet interact with their birth environment, as this plays an important role in their composition and final orbital configuration.

Direct imaging plays an important role here. By spatially resolving the disk and embedded planets we can witness their interaction. Another added benefit is the enhanced intrinsic contrast between the star and planet for young luminous planets. For old systems such as our own solar system the best signal we could use to detect Earth or Jupiter from a distance is through reflected light. The intensity ratio between the Sun and the reflected light of Earth and Jupiter are 10^{-10} and 10^{-9} respectively. This is a huge contrast to overcome. But during the first stages of planet formation the planets are still very hot. This increases the intrinsic contrast in the near-infrared to $10^{-5} - 10^{-6}$ making the detection of such exoplanets orders of magnitude easier.

But direct imaging of exoplanets is still a challenging task even for the hot young gas planets because the contrast needs to be reached at very close angular separations. While current generation telescope like the Very Large Telescope (VLT) of ESO, with an 8.2 meter diameter, would be able to resolve the closest by planets we have not been able to do this. For ground based telescope there are two challenges to overcome. The first being turbulence in the atmosphere and the second is the intrinsic contrast between the planet and its host star. This turbulence will create wavefront aberrations that degrade the resolving power of the telescope. In median weather conditions at good observing sites such as Paranal, La Palmca or Mauna Kea the effective resolution due to the atmosphere is about 1

arcsecond, almost 40 times larger than the diffraction limit! Nowadays all the large telescopes use adaptive optics, where a deformable mirror is controlled at several hundreds of Hz to several kHz to counteract the atmosphere. For direct imaging the AO systems are pushed to their extremes and are therefore called eXtreme AO (xAO) systems.

With the current generation of xAO systems we can reach diffraction-limited performance in the near-infrared. But this is not enough to find faint planets as the planet is still much fainter than the Airy rings of the diffraction pattern. With the high quality correction of xAO systems such as SPHERE and GPI we can use coronagraphs to remove the diffraction effects of the star. A coronagraph is a specialized optical device that is designed as an extreme angular filter; the on-axis starlight needs to be suppressed as much as possible while leaving the off-axis planet light unaltered. But any wavefront error in the system will limit the performance of the coronagraph and will scatter starlight back into the region that we want to make and keep dark. The residual wavefront errors come from two sources, the first being residual wavefront errors from the atmosphere that are not correctable or not completely removed. The second are due to a difference in the optical path between the coronagraphic optics and the wavefront sensor optics. Because these parts of the instrument have different optics they will see a slightly different wavefront error causing differential wavefront errors between the two paths. These wavefront errors are called the Non-Common Path Aberrations (NCPA). Both the NCPAs and the residual turbulence causes speckles that can look like planets. Image processing algorithms are used to further remove these speckles and enhance the contrast.

With medium to high-resolution spectroscopy we can make use of the difference between the planet spectrum and the star spectrum to remove the starlight. Spectral filters tuned to the host star can be used to remove the starlight while leaving the exoplanet's spectrum largely undisturbed. A distinct advantage of this technique is that it is not limited by speckle noise, which hampers other post-processing techniques. High-resolution spectroscopy and medium-resolution integral-field spectroscopy in the near-infrared has been used to characterize several exoplanet atmospheres. None of the current direct imaging instruments have the capability of higher-resolution spectroscopy and adding this would allow us to probe closer to the star and search for lower mass planets. In this thesis we have explored several aspects of high-resolution integral-field spectroscopy for direct imaging.

Chapter 2+3: The Leiden EXoplanet Instrument

We have build several iterations of the Leiden EXoplanet instrument (LEXI), which is visitor instrument for the William Herschel Telescope at La Palma. The purpose of LEXI was to test different ways of coupling an AO-corrected beam to an integral-field spectrograph. To date LEXI has been use on-sky during three different observing campaigns. The first iteration of LEXI consisted of an AO-assisted long-slit spectrograph. The on-sky results showed that AO improves both throughput and spatial resolution of diffraction-limited slit spectrographs. Between the different campaigns LEXI was continuously upgraded to improve its performance. The second observing campaign was focused on improving the imaging performance and the spectrograph bandwidth. The adaptive optics upgrade from a Shack-Hartmann wavefront sensor to the new generalized Optical Differentiation Wavefront sensor together with the strategy to stop down the aperture made it possible to create diffraction-limited images with LEXI and paved the way towards on-sky tests of extreme AO techniques. This resulted in a successful demonstration of non-common path correction with the coronagraphic Modal Wavefront Sensor, that was able to increase the on-sky contrast by a factor of 1.5-2.

Additional due to the high performance of the AO system we were able to couple starlight into a single-mode fiber. A single-mode fiber can be considered as a diffraction-limited fiber. With the single-mode fiber, LEXI feeds a compact cross-dispersed echelle spectrograph designed to have a resolving power close to 100000. From the on-sky observations of Aldebaran we could measure the resolving power of the spectrograph to be 92000, which is very close to the design resolution. This result encouraged us to continue and develop a single-mode fiber-fed integral-field spectrograph, which was used during the third observing campaign.

Chapter 4+5: The Single-mode Complex Amplitude Refiner (SCAR) coronagraph

In these chapters the concept and first lab results of the Single-mode Complex Amplitude Refiner (SCAR) coronagraph are demonstrated. The SCAR coronagraph exploits the design freedom offered by the use of single-mode fibers as a mode filter. The fibers are fed by micro-lenses for increased field coverage making it possible to use single-mode fibers to search for exoplanets. We combined this with a pupil-plane phase plate, yielding the SCAR coronagraph that has several advantages including low inner-working angle and high throughput over a sizeable bandwidth. Our lab results confirm the working principle and demonstrated a coronagraph that reaches a

contrast 10000 at 1 λ/D.

Chapter 6: A duo of accreting proto-planets around the young star PDS 70

In this chapter I presented the results that were obtained with the adaptive-optics assisted, medium-resolution, integral-field spectrograph MUSE at the Very Large Telescope of ESO. With MUSE we were able to detect two proto-planets, that are still actively accreting, around the young star PDS 70. Our observations show that IFUs are highly efficient instruments to observe accretion emission spectra from planets in formation. We suspect that more accreting planets could be found and characterized in transition disks with this technique. Another exciting opportunity, which is now possible due to the high observing efficiency, is the detailed investigation of accretion on short and long time scales. This will shed light on the variability of planetary accretion and will lead to a better understanding of the formation of planets, allowing us to infer the formation history of the solar system.

Chapter 7: Highly multiplexed Bragg gratings

For a given detector there is a trade off between the spectral range, spectral resolution and field of view of an integral-field spectrograph. In this chapter we propose a novel method based on multiplexed Volume Bragg Gratings (VBGs) to analyse the spectrum optically, that eliminates the need to measure the complete spectral bandwidth. We have shown that such VBGs with many multiplexed gratings can be used for the quantitative detection of gas species with a significantly smaller detector than a comparable hyperspectral imager. This allows for a larger field-of-view given the same amount of detector real estate. We proposed to implement the VBGs with acousto-optical gratings that can be dynamically tuned at high speed and work from the near UV to the infrared. The dynamical aspect of the acousto-optical materials will allow us to use the same optics to detect different species. This simplifies the whole instrument as we can digitally choose what we would like to observe and thereby making the instrument highly flexible.

Outlook

Our observations with MUSE show that higher-resolution spectroscopy is very well suited for direct imaging of exoplanets. In the next few years several xAO systems will be upgraded with high-resolution spectroscopy. SPHERE will be coupled with CRIRES+, the KECK telescope will also get a fiber link between KPIC and NIRSPEC and SCEXAO on the SUBARU telescope will be coupled to RHEA. The techniques that were developed in

this thesis can be used to implement the actual coupling between the xAO systems and their spectrographs.

This work at medium resolution lays down the foundation for visible-light high-resolution integral-field units and high-contrast imaging for the detection of reflected light from cold and old exoplanets, like Earth, and biosignatures such as the O_2 band with the Extremely Large Telescopes (ELT). High-resolution spectroscopy for exoplanets is a photon-starved observing technique. The detection limits are therefore set by the amount of light that we can collect from the star and the planet. Proxima Centauri b could be characterized with the current telescopes but almost a hundred nights spread over three years are necessary to guarantee a detection. The effective observing time can be drastically lowered by using one of the ELTs. ELTs come with two advantages, the first being the larger collecting area, and the second is the increased spatial resolution. With an ELT the detection of Proxima Centauri b can obtained in a single night instead of the hundred nights of VLT time. With the addition of high-resolution integral-field units to extreme adaptive optics systems at ELTs, we will start to study older, potentially habitable planets, and thus address humanity's ultimate question: Are we alone?

9 | Nederlandse samenvatting

Het veld van exoplaneten is in de afgelopen dertig jaar in een stroom versnelling beland na de ontdekking van de eerste paar exoplaneten. In 1992 was de eerst planeet rondom een andere ster dan de zon gevonden, en nog geen drie jaar later in 1995 werd de eerste exoplaneet rondom een zonachtige ster gevonden. Ondertussen zijn er duizenden planeten meer ontdekt, die zo divers zijn dat het erop lijkt dat elk systeem uniek is. Er zijn vreemde planeten zoals Kepler 51 b en d die een vergelijkbare dichtheid hebben als een suikerspin of de extreem hete planeet KELT-9b waar er ijzer en titanium in gas vorm in de atmosfeer aanwezig is. Naast de diversiteit in de planeten zelf is er ook een grote diversiteit in de planeetstelsels. Aan de ene kant is er Trappist-1 met 7 aardachtige planeten rondom een rode dwerg, en aan de andere kant hebben we HR8799 met vier gas reuzen die zich bevinden op een gigantische afstand van hun ster. Deze verscheidenheid in planeten en planeetstelsel stelt onze theorie over het onstaan van planeten op de proef, aangezien we alles zouden moeten kunnen verklaren. Een van de hoofd vragen op dit moment is hoe planeten reageren op hun geboorte omgeving, doordat dit een erg belangrijke rol speelt in hun opbouw en uiteindelijke positie.

Het direct waarnemen van exoplaneten heeft een sleutelrol in het beantwoorden van deze vraag. Door de planeet te onderscheiden van de stofschijf waarin hij zich bevind kunnen we de interactie tussen de twee waarnemen. Naast dat deze fase belangrijke vragen beantwoord over het onstaan van planeten, is deze fase ook makkelijker waar te nemen doordat de planeten in deze fase nog heet en helder zijn. In oude systemen zoals ons zonnestelsel zijn de meeste planeten afgekoeld en zenden daardoor veel minder licht uit, het beste zouden we ons zonnestelsel nog kunnen zien door te kijken naar gereflecteerd zonlicht. De ratio tussen het uitgezonden licht van de zon en het gereflecteerde licht van de Aarde of Jupiter ligt rond de 10^{-10} en 10^{-9}. In vergelijking ligt dit intrinsieke contrast in de begin fase rond de 10^{-5} to 10^{-6}, wat veel makkelijker waar te nemen is.

Helaas is het direct waarnemen van planeten nog steeds een heel uitdagende taak, zelfs voor de hete gas reuzen doordat het constrast heel docht bij de ster bereikt moeten worden. Alhoewel de huidige generatie telscopen zoals de Very Large Telescope (VLT) van ESO, met een 8.2m diameter, de planeten zouden moeten kunnen onderscheiden van de ster spelen er twee problemen die ons daarin beperken. De eerste is de turbulentie van de atmosfeer en de tweede is het intrinsieke contrast tussen de planeet en ster. Door de turbulentie wordt het pad van het licht verstoord waardoor de resolutie van de telescope wordt verminderd. Op goede sterrewachten

in de wereld wordt een resolutie van 1 arsecond gehaald in gemiddelde omstandigheden, bijna 40 keer groter dan het diffractie limiet! Tegenwoordig gebruiken bijna alle grote telescopen adaptieve optiek om de effecten van de atmosfeer tegen te gaan. Hierin wordt een vervormbare spiegel bestuurd om enkele honderden Hz to enkele duizenden Hz. Voor instrumenten gespecialiseerd voor de zoektocht naar exoplaneten worden zulke systemen tot het uiterste gedreven en worden daarom soms ook extreem adaptieve optiek (xAO) systemen genoemd.

Met de huidige generatie xAO systemen kunnen we het diffractie limiet van de telescope halen in het nabij infrarood. Maar dit is niet genoeg om de licht zwakke planeten te vinden doordat zij nog steeds veel zwakker zijn dan het diffractie patroon van de ster. Een coronagraaf is een gespecialiseerd stukje optiek dat ontworpen is als een extreem hoek gevoelig filter; het diffractie patroon van de ster wordt zoveel mogelijk onderdrukt terwijl er wordt geprobeerd zoveel mogelijk licht door te laten van de planeten. Helaas zijn coronagraven gevoelig voor elke golffrontfout die zich nog in het systeem bevind, waardoor er toch nog ster licht wordt door gelaten. De golffrontfouten bestaan uit twee componenten. De eerste komt door atmosferische turbulentie die niet volledig gecorigeerd is ofwel doordat het systeem niet perfect werkt danwel doordat het systeem specifieke fouten niet kan corrigeren. De tweede worden door het instrument zelf gemaakt. Er zijn namelijk verschillen tussen de optische elementen van het adaptieve optieke systeem waar de fouten worden gemeten en de uiteindelijke camera. Door dit verschil in optika zullen er kleine verschillen in de golfrontfouten zijn. Deze worden niet gemeenschappelijke pad fouten genoemd. Zowel de overgebleven turbulentie als de niet gemeenschappelijk pad fouten zorgen ervoor dat het sterlicht niet volledig weg gefilterd is. Daarom gebruiken we geadvanceerde beeld verwerking technieken om de laatste beetjes sterlicht weg te halen.

Door middel van spectroscopie kunnen we de verschillen zien tussen het planeet licht en het ster licht. Door dit verschil tussen de ster en planeet kunnen we met speciaal afgestemde spectraal filters het ster licht weg halen terwijl we het planeet signaal zoveel mogelijk ongemoeid laten. Een van de voordelen van deze techniek is dat het niet wordt gelimiteerd door de aanwezigheid van golffront fouten, wat wel een limiteerende factor is voor andere beelverwerkings technieken. Verschillende keren is dit nu toegepast om exoplaneten te karateriseren. Helaas hebben geen van de huidige xAO instrumenten voor exoplaneten de benodigde spectrale resolutie om deze techniek toe te passen. Als er hogere resolutie spectroscopie

beschikbaar is zou er dichter bij de ster gezocht kunnen worden; precies waar we verwachten dat de planeten zich bevinden! In deze thesis kijken we naar verschillende aspecten van hogere resolutie spectroscopie voor het direct waarnemen van exoplaneten.

Hoofdstuk 2+3: The Leiden EXoplanet Instrument

Door de jaren heen zijn er verschillende versies van het Leiden EXoplanet Instrument (LEXI) gebouwd. LEXI is een instrument dat elk jaar tijdelijk naar de William Herschel Telescope op La Palma wordt gebracht om daar te observeren. Het doel van LEXI was om verschillende manieren te testen hoe we instrumenten die adaptieve optiek bezitten het beste kunnen combineren met ruimtelijk opgeloste spectroscopie. Onze eerste versie van LEXI was een adaptief optiek systeem waarbij het veld van de spectrograaf werd gekozen doormiddel van een lange spleet. De resultaten die genomen zijn tijdens de eerste observatie ronde laten zien dat AO zowel de efficienctie als de ruimtelijke resolutie verbeterd van dit type spectrograven. Na de bemoedigende resultaten is LEXI verbeterd. De tweede observatie ronde had het doel om de beeld kwaliteit te verbeteren en het spectraal bereik uit te breiden. De beeld kwaliteit hebben we verbeterd door de golffront sensor te vervangen van een Shack-Hartmann sensor naar de generalized Optical Differentiation Wavefront Sensor en door de apertuur van de telescoop te verkleinen. Door de verbeteringen konden we nieuwe xAO technieken testen die niet gemeenschappelijke fouten proberen te meten en corrigeren. Tijdens onze tweede keer op de telescoop hebben we succsvol de coronagraphic Modal Wavefront Sensor kunnen testen waarmee we bijna een factor 2 wonnen in contrast.

Daarnaast hebben we ook dankzij de goede kwaliteit van het AO systeem licht kunnen koppelen in een single-mode fibre. Een single-mode fibre kan worden gezien als een diffractie gelimiteerde fibre. LEXI gebruikt de single-mode fibre om het licht te transporteren naar een compacte cross-dispersed echelle spectrograaf die een design resolutie heeft van rond de $\lambda/\Delta\lambda \approx 100000$. De resultaten die we hebben behaald met observaties van de ster Aldebaran laten zien dat onze uiteindelijk resolutie boven de 92000 ligt. Onze volgende stap was het ontwikkellen van een bundle van single-mode fibres die door de spectrograaf werd geanalyseerd waarmeer we ruimtelijk opgeloste spectra konden nemen. Uiteindelijk was deze nieuwe versie getest tijdens de derde observatie ronde van LEXI.

Chapter 4+5: De Single-mode Complex Amplitude Refiner (SCAR) coronagraaf

In deze twee hoofdstukken wordt het concept van de Single-mode Complex

Amplitude Refiner coronagraaf en de eerste lab experimenten gedemonstreerd. De SCAR coronagraaf maakt gebruik van de extra vrijheids graad die single-mode fibers bieden dankzij hun vermogen om elektrische velden te filteren. De fibers worden door micro-lenses belicht om het beeldveld te vegroten zodat het mogelijk wordt om ook met een single-mode fiber bundel naar exoplaneten te zoeken. We combineren dit met een stuk optiek in de apertuur van het systeem dat de fase van het inkomende licht aanpast, hierdoor kunnen wij het sterlicht in gekozen fibers weg filteren. De coronagraaf heeft een aantal nuttige voordelen zoals de kleine mimimale hoek separatie waar planeten gezocht kunnen worden en de relatief hoge throughput. Onze lab resultaten bevestigen het principe achter de coronagraaf en demonstreren ook dat we minimaal een contrast van 10000 op 1 λ/D kunnen halen.

Chapter 6: A duo of accreting proto-planets around the young star PDS 70

In dit hoofdstuk heb ik de resultaten gepresenteerd van observaties die waren genomen met MUSE op de Very Large Telescope. MUSE is AO gecorrigeerde spectrograaf met een ruimtelijke resolutie van 50 milliarcseconden. Met MUSE is het gelukt om rondom de jonge ster PDS 70 twee proto planeten te detecteren die nog actief aan het accreteren zijn. De planeten zijn gas reuzen met een massa van een paar keer die van Jupiter. Waarschijnlijk zijn de twee ook aan het einde van hun groei fase gezien de accretie snelheid van $\approx 10^{-8} M_{\mathrm{J}}/\mathrm{yr}$. Volgens onze observaties bevinden deze planeten zich ook dichtbij een 2:1 baan resonantie, wat door veel modellen werd voorspeld als waarschijnlijk configuratie voor systeem met meerdere planeten. De vondst van dit systeem is erg belangrijk aangezien dit tot nu toch toe het enige systeem is met meerdere planeten die zich nog in de stofschijf van de ster bevinden. Hierdoor kunnen veel planeet schijf interactie theorieen getoetst worden, waardoor we weer meer te weten komen over het onstaan van planeten.

Chapter 7: Highly multiplexed Bragg gratings

Voor een spectrograaf met een groot beeldveld is er een afweging tussen het spectraal bereik, spectrale resolutie en beeldveld voor gegeven detector. In dit hoofdstuk presenteren we een nieuwe methode die gebaseerd is op gemultiplexde Volume Bragg Gratings (VBGs) die het spectrum optisch analyseren, waardoor de noodzaak verdwijnt om heel het spectrum waar te nemen. We hebben laten zien dat zulke VBGs met veel gemultiplexde lijnen gebruikt kunnen worden voor quantitatieve detectie van gas soorten met een significant kleinere detector. Daardoor is het mogelijk om voor

een gegeven detector een groter beeldveld te hebben dan voor een conve-
tionele spectrograaf. We stellen voor om de VBGs te implementeren met
akoesto-optische tralies die dynamisch ingesteld kunnen worden op hoge
snelheid en werken over heel het spectraal bereik van het nabij UV to in
het infrarood. Doordat de grating dynamisch ingesteld kan worden kan
er ook makkelijk gezocht worden naar verschillende gas soorten wat het
instrument erg flexibel maakt.

Een blik op de toekomst

Onze observaties met MUSE laten zien dat hogere resolutie spectroscopy
erg geschikt is voor het direct waarnemen van planeten. Er zijn plannen
om in de komende jaren meerdere xAO instrumenten een upgrade te geven
zodat ze toegang hebben tot spectroscopy. SPHERE wordt gekoppeld aan
de spectrograaf CRIRES+, de KECK telescoop krijgt een ook een glasvezel
verbinding van de xAO imager naar NIRSPEC en SCEXAO op de SUBARU
telescoop wordt gekoppeld aan RHEA. De technieken die ontwikkeld zijn
in deze thesis om xAO systemen te koppelen met spectrograven zijn daar
in het bijzonder geschikt voor.

Dit werk legt de fundering om in de toekomst met de Extremely Large
Telescope hoge resolutie spectroscopy te gebruiken voor de detectie van
gereflecteerd licht van oude en koude exoplaneten zoals de Aarde. Daar-
naast zou deze techniek ook gebruikt kunnen worden om biosignaturen te
detecteren zoals de zuurstof band. Hoge resolutie spectroscopy is een tech-
niek die gelimiteerd is door photonen ruis. Daarom wordt het detectie limiet
bepaald door de hoeveelheid licht die we kunnen ontvangen van de ster en
planeet. Het is mogelijk om met de huidige telescopen Proxima Centauri b
te karakteriseren, alleen zijn er bijna honderd nachten aan observatie tijd
voor nodig om een detectie te garanderen. Met een ELT zouden we de
tijd die nodig is drastisch kunnen verlagen. ELTs komen met twee voorde-
len, de eerste is dat de telescope een groter oppervlak heeft en meer licht
verzamelt, en de tweede is de hogere ruimtelijke resolutie. Met een ELT
zouden we Proxima Centauri b kunnen detecteren in een enkele nacht in
tegenstelling tot de honderd nachten met de Very Large Telescope. Door
hoge resolutie spectroscopy met extreme adaptieve optica toe te voegen aan
ELTs kunnen we beginnen met het bestuderen van oudere en mogelijk ook
bewoonbare planeten en daarmee kunnen we een van de oudste vragen van
de mensheid beantwoorden; Zijn wij alleen?

Curriculum Vitae

I was born on the 3rd of May 1992 in Zoetermeer, The Netherlands, where I grew up. Growing up with access to the internet from an early age allowed me to read many webpages about astronomy, which triggered my fascination with the universe and its scale. And as a teenager I decided very early on that I would study astronomy. It helped that my high school, the Oranje Nassau College Parkdreef in Zoetermeer, was a specialised school for natural sciences.

Because I was also very interested in physics I started a double bachelor in Physics and Astronomy at Leiden University in 2010. During my first year at university I always claimed that I would never want to work with optics. This was quickly remedied when I started my bachelor's thesis project on the optimization of the real time control software of the adaptive optics system for ExPo under supervision of Christoph Keller. This project showed me the interesting and difficult technical challenges of direct imaging of exoplanets. Therefore I decided to continue my masters at Leiden University in 2013 with a research specialisation in Astronomical Instrumentation. This was the perfect mixture of experimental physics and astronomy for me.

For my first masters research project I worked under supervision of Nathan de Vries and Simon Portegies-Zwart on dynamical capture of stars by intermediate-mass black holes using 3D hydrodynamical simulations. During my second research project I developed a new wavefront sensor under supervision of Christoph Keller. I finished my masters cum laude and was awarded the "De Zeeuw-Van Dishoeck Afstudeerprijs" for my thesis.

I started my PhD at Leiden Observatory on the 1st of September 2015, under supervision of Christoph Keller and Ignas Snellen. I worked on several projects that were related to integral-field spectroscopy of exoplanets and build the Leiden EXoplanet Instrument. During my years at Leiden Observatory I had the opportunity to spend a considerable amount of time at the observatory on La Palma, where I observed with LEXI.

As of the 1st of November 2019, I will be a Sagan fellow in the Extreme Wavefront Control Lab at the University of Arizona in the Unites States of America.

Acknowledgments

I have spent a considerable amount of time at Leiden Observatory all the way from my bachelors up to my PhD. During this time I met a lot of people that I would like to thank. But first of all, I would like to especially thank Christoph Keller and Ignas Snellen for hiring me as a PhD candidate. You gave me the freedom to explore everything I found interesting. This freedom was sometimes difficult but thanks to the helpful discussions and guidance I was able to find my own way.

Many thanks to my fellow members of the instrumentation group, David, Steven, Maaike, Mike, Emiel, Patrick, Rob, Olivier, Jos, Christian, Schuyler, Alex and Kelsey. You guys were the best support during the somewhat brutal LEXI runs at the WHT. I always like to travel with you to conferences we went to as a group, we had a lot of fun during those days that sometimes for me felt like school trips. And of course I can not ignore the endless discussion that we often have, which really helped me to understand crucial details of the problems we face in direct imaging.

As I was part of two research groups during my PhD I also want to thank the past and present members of the exoplanet group, Jens, Geert-Jan, Emanuelle, Henriette, Andrew, Dilovan, Javi, Vincent, Alex, Paul and Paul. Because of my focus on instrumentation I had quite some gaps in my knowledge of exoplanet physics, the many journal clubs and exoplanet meetings helped me tremendously to fill in those gaps.

Of course I would also like to thank the breaks and lunch group, Kirsty, Stijn, Leon and Leindert. You guys tried to keep us away from instrumentation for a moment, giving us a normal break instead of another meeting.

I would also like to thank the many students that I supervised over the past few years, Irene and Vivienne, Joost, Martijn, Steven, Louis, Pieter and Okke, Rico, Thijs, Fedde, Chen and Jeroen. I have learned a tremendous amount from supervising you. And as a teaching assistant I helped with the second year astronomy lab for 5 years together with Henk Hoekstra and Jarle Brinchmann and of course Christos and the many other TAs. The observing runs at the INT on La Palma were always one of the highlights of the year and I would like to thank everyone, including all the students, for making them very enjoyable.

As I spent a lot of time at both INT and the WHT on La Palma I would also like to thank the amazing support team that works at the Observatorium Roque de los Muchachos.

Ik zou ook mijn ouders willen bedanken, zij hebben mij alle steun en mogelijkheden gegeven om uit te vinden wat ik leuk vond. Daarnaast hebben zij mij ook geleerd om door te zetten en altijd jezelf te verbeteren. Dit zijn

eigenschappen waar ik tijdens mijn studie jaren en PhD enorm veel aan heb gehad.

En het meeste gaat mijn dank uit aan Shirley, mijn vrouw. In de afgelopen jaren ben jij mijn grootste steun geweest. Je staat altijd voor mij klaar en hebt zelfs ervoor gekozen om samen met mij naar Arizona te gaan aan de andere kant van de oceaan. Ik ga graag samen ons nieuwe avontuur tegemoet.